Universidad del País Vasco,
Centro de Física de Materiales

Master thesis :

First-principles calculation of plasmonic resonances and electric field enhancement in metal-cluster dimers

---

Marc Barbry [1]

Under the supervision of Daniel Sánchez-Portal and Peter Koval

Donostia San-Sebastian, Spain

2013-2014

[1] marc.barbry@mailoo.org

Preface

This Thesis is submitted in partial fulfillment of the requirements for the degree of Master in Nanoscience at the university of the Basque country, within the field of Physics and Nanoscience. The work was carried out from September 2013 to June 2014 at the Centro de Fisica de Materiales (CFM) under the supervision of Daniel Sánchez-Portal and Peter Koval. Financial support was provided by the Donostia Internationnal Physics Center (DIPC), Euskampus and the Centre National de la Recherche Scientifique (CNRS) de Bordeaux.

I would like to thank the institution and the individuals that helped me to realize this work. Most of my gratitude goes to Peter Koval who gave me full support during this thesis and who guided me at each step of the work both for the code and the theory. My thanks go of course to Daniel Sánchez-Portal who gave me the opportunity to work in his group and for the time that he spent explaining me the project and the theory. I would like to thank Federico Marchesin for our nice talks and the explanation that he provided to me.
However, my special thanks go to Professor Dietrich Foerster who is giving me full support since my bachelor at Bordeaux, thanks to him I learned a lot about computational physics, and without him I would have never been able to get where I am today.

Donostia San-Sebastian, June 2014

Marc Barbry

Abstract

In this work we investigate the optical properties of small metallic clusters. We present an ab-initio study of the polarizability and electrical field enhancement in the vicinity of metallic clusters and metallic cluster dimers. The ab-initio approach is based on time dependent density functional theory (TDDFT). It allows to confirm basic features of absorption spectra and to examine the spatial- and frequency-dependence of the field enhancement in nanocavities of different sizes and shapes. For the calculations we employ a new implementation of TDDFT in the linear response regime. This implementation is optimized for utilizing locality of operators in order to construct an algorithm of low computation complexity. The TDDFT code is interfaced with SIESTA, an efficient density functional theory implementation. During this thesis the TDDFT code has been extended to compute the spatial distribution of the induced electrical field. Moreover, low complexity algorithms employed in SIESTA and in our TDDFT code made possible to compare electric field enhancement between sodium dimers (compose of clusters of up to 150 atoms).

Contents

Chapter 1

Introduction

Electronic excitations, caused by irradiation with electrons, conventional or modern light sources (synchrotron, ultrafast lasers), are key quantities for the study of materials, ranging from solids to atoms, from surfaces to nanoscale systems. An improved understanding and prediction of the interaction of radiation with matter is instrumental for the development of new technologies, as new functionalities in bulk systems (e.g. optoelectronic) or, in the long term, in biological applications ("bottom up" assembly of molecular machines[1]).

Moreover, recent progress in fabrication of nanodevices has made possible the production of nanoobjects of controlled composition and shape down to atomic precision. For instance, the production of metallic clusters of a given size has been demonstrated [5]. Metallic clusters of Ag, Cu, Au have been used to amplify Raman spectroscopy signal [6]. Recently, the interest of surface-enhanced Raman spectroscopy has exploded for two major reasons. The first is the realization that under favorable circumstances, Raman enhancements as large as 14 order of magnitude can be achieved, i.e., Raman spectra of single molecules can be measured. The second reason is the recent interest in creating of an ultra-sensitive sensing platform based on surface-enhanced Raman spectroscopy with molecular identification capabilities. One of the mechanisms that leads to amplification of Raman signal is so-called electromagnetic field enhancement [6]. The laser field used in the measurement of Raman shifts acts not only on the target molecule but also on the objects which surround the molecule. If a metallic cluster is located in the vicinity of the target molecule, then the electromagnetic field induced in the position of the molecule by the cluster response can be much larger than the exciting of the laser field.

In this thesis we develop and use a suite of tools to compute the electromagnetic field enhancement. We use methods which do not require the knowledge of the many-body wave-function of the system. Namely, time-dependent density functional theory in the linear response regime. Density functional theory (DFT) and time-dependent functional theory (TDDFT) have been extensively used to study optical properties of nanomaterials as graphene nanoflakes [7] and metallic nanocavities [8]. A number of recent publications [9, 10, 11] have treated the electronic response of plasmonic structures using state-of-the-art TDDFT [12, 13]. However, in most of these works the structures were modeled using a simplified description based on the so-called "jellium model". In our work we perform an analysis of the spatial distribution of the density change and of the electric field enhancement which is sometimes neglected because of its computational cost. The induced electrical field is computed from the induced density change according to classical expressions for the Coulomb field.

The thesis consists of two more chapters besides the introduction. In the following, we develop theoretical description of time-dependent phenomena in many-electron systems. To achieve this, we

[1] Scientists have discovered how to use a single plastic molecule to drive a tiny machine. One frequency of light causes the molecule to contract and another causes it to expand, making it move a board down up repeatedly [1]. For details on molecular machines set in action by light, see Refs[2, 3, 4]

develop in chapter 2 the basics theories used during this thesis. We show in section 2.1 how time-dependent perturbation theory leads to a well-know expression for absorption cross section. In section 2.2.1 we describe basics of the density-functional theory that allow to simplify the complexity of the many-electron systems to effective one-particle equations. In section 2.2.2 the time-dependent extension of DFT will be discussed. Time-dependent density-functional theory in linear response regime will be used in section 2.3 in order to derive expressions for the frequency-dependent induced density change and the corresponding electrical field. In section 2.4 we present a small model of two interacting dipoles to compare it with our ab-initio results. In chapter 3 we analyze our calculations of the polarizability and electrical field enhancement for several Na clusters. Our conclusions are summarized in section 4.

Chapter 2

Theory

In the atomic scale the objects show their quantum mechanical nature. As a consequence of this, quantum mechanics is required for a reliable ab-initio description of the studied processes. In this work we focus on phenomena which are determined by the so-called valence shell electrons. The description of these electrons can be non-relativistic in many cases because relevant energy changes (a few eV's) are small comparing to the rest mass energy of the electron (0.511 MeV). Therefore, the wave-function of valence shell electrons can be found as a solution of the well known Schrödinger equation (SE). The solution of SE for a many electron system is a highly non-trivial problem. However, as shown by Kohn [14], many phenomena are amenable for a description within the ab-initio framework of density-functional theory (DFT). The modern formulation of DFT is based on the so-called Kohn-Sham (KS) scheme that reduces to the one-particle SE for an effective electric potential. In our study we will rely on the KS formulation of DFT. DFT allows to determine (in principle exactly) the electronic density of any static quantum system. For instance, DFT is very successful for the determination of molecular geometries, statical dipoles and other properties that are determined by valence-shell electrons.

The valence electrons determine the spectroscopic properties of materials at optical and infra-red wavelengths. The optical absorption and Raman spectroscopy employ lasers to perturb the atoms, molecules, clusters or solids. Typically, laser fields are much smaller than the static fields experienced by valence shell electrons. Therefore, it is usually possible to use perturbation theory to find an approximate solution of time-dependent KS equations. In the following, we outline basics of the time dependent perturbation theory on which a time-dependent perturbation theory in linear response regime is used (section 2.2). In all the thesis, atomic units will be used (excepted when it is indicated).

2.1 The Time Dependent Perturbation Theory

In this section, we derive the photo-absorption cross section for one-electron quantum systems. This will be done in the limit of small perturbation when the potential acting on the electron can be separated into two parts: one large and static, another small and time-dependent. The Hamiltonian of our system can be then written as

$$H = T + V_0(\mathbf{r}) + V_{\text{pert}}(\mathbf{r}, t). \tag{2.1}$$

Here T is the kinetic energy operator, $V_0(\mathbf{r})$ is the static part of the potential and $V_{\text{pert}}(\mathbf{r}, t)$ is the time-dependent part of the electric potential. The full Schrödinger equation reads

$$H\psi(\mathbf{r}, t) = \mathrm{i}\frac{\partial\psi(\mathbf{r}, t)}{\partial t}, \tag{2.2}$$

where $\psi(\mathbf{r},t)$ is the one-particle wave-function. Solving the Schrödinger equation (2.2) for the wave-function $\psi(\mathbf{r},t)$ would give us all information about the evolution of the system.

If the full Hamiltonian H can be separated into a large static part and a small time-dependent part, then SE (2.2) can be approximately solved in terms of the solutions of stationary SE. This is worth to do because the solutions of the equation

$$\{T + V_0(\mathbf{r})\}\,\psi_0(\mathbf{r},t) \quad = \quad \mathrm{i}\frac{\partial\psi_0(\mathbf{r},t)}{\partial t}, \tag{2.3}$$

are usually easier to determine.

In the latter equation (2.3) the operator on the right hand side $\{T + V_0(\mathbf{r})\}$ is time-independent and solutions $\psi_0(\mathbf{r},t)$ are amenable to a separation of variables. As there are many solutions of the equation (2.3), we will provide an additional index n in order to distinguish them.

$$\psi_n^0(\mathbf{r},t) \quad = \quad \phi_n(\mathbf{r})\mathrm{e}^{-\mathrm{i}E_n t}, \tag{2.4}$$

where E_n are the so-called eigen-energies. Moreover, time-independent parts of wave-functions $\phi_E(\mathbf{r})$ satisfy the *time independent eigenvalue equation*

$$\{T + V_0(\mathbf{r})\}\,\phi_n(\mathbf{r}) \quad = \quad E_n\phi_n(\mathbf{r}). \tag{2.5}$$

Time dependent perturbation theory (TDPT) is a method to obtain $\psi(\mathbf{r},t)$ in terms of $\psi_n^0(\mathbf{r},t)$ in a general case [15]. In the next subsection we will consider an idealized case of a quantum system with two-levels only. Nonetheless, the two-levels example provides a direct and clear link to the phenomena of spontaneous emission and induced transitions. The absorption cross-section, which is an observable in the absorption spectroscopy will be derived in this minimal example.

2.1.1 Two-level System

For simplicity, the system treated here is composed of only one electron. We assume that there is just two states of the unperturbed Hamiltonian H_0, $\phi_a(\mathbf{r})$ and $\phi_b(\mathbf{r})$

$$H_0\phi_a(\mathbf{r}) = E_a\phi_a(\mathbf{r}), \quad H_0\phi_b(\mathbf{r}) = E_b\phi_b(\mathbf{r}), \quad \langle\phi_a|\,\phi_b\rangle = \delta_{ab}. \tag{2.6}$$

Any state of the system can be expressed as a combination of the eigen states ϕ_a and ϕ_b

$$\psi(\mathbf{r},0) \quad = \quad c_a\phi_a(\mathbf{r}) + c_b\phi_b(\mathbf{r}). \tag{2.7}$$

Without an external perturbation, any solution of the time dependent SE for the two-level system can be expressed as a linear combination

$$\psi(\mathbf{r},t) \quad = \quad c_a\phi_a(\mathbf{r})\mathrm{e}^{-\mathrm{i}E_a t} + c_b\phi_b(\mathbf{r})\mathrm{e}^{-\mathrm{i}E_b t}, \tag{2.8}$$

where $|c_a|^2 + |c_b|^2 = 1$ in order to ensure normalization to one electron. In the presence of a perturbation, the coefficients c_a and c_b become time dependent (in the next equations, we drop spatial dependence)

$$\psi(t) \quad = \quad c_a(t)\phi_a \mathrm{e}^{-\mathrm{i}E_a t} + c_b(t)\phi_b \mathrm{e}^{-\mathrm{i}E_b t}. \tag{2.9}$$

The whole problem is reduced to determine the coefficients $c_a(t)$ and $c_b(t)$. We next insert the ansatz (2.9) into equation (2.2) and choose the time-dependent Hamiltonian H in the form $H = H_0 + H'(t)$, where $H'(t)$ is a time-dependent perturbation.

$$\begin{aligned} c_a H_0 \phi_a \mathrm{e}^{-\mathrm{i}E_a t} + c_b H_0 \phi_b \mathrm{e}^{-\mathrm{i}E_b t} + c_a H' \phi_a \mathrm{e}^{-\mathrm{i}E_a} + c_b H' \phi_b \mathrm{e}^{-\mathrm{i}E_b t} = \\ \mathrm{i}\left(\frac{dc_a}{dt}\phi_a \mathrm{e}^{-\mathrm{i}E_a t} + \frac{dc_b}{dt}\phi_b \mathrm{e}^{-\mathrm{i}E_b t} - \mathrm{i}E_a c_a \phi_a \mathrm{e}^{-\mathrm{i}E_a t} - \mathrm{i}E_b c_b \phi_b \mathrm{e}^{-\mathrm{i}E_b t} \right). \end{aligned} \tag{2.10}$$

The two first terms on the left hand side cancel with the two last terms on the right hand side, because they obey the non perturbed time-dependent SE (2.3). Therefore, equation (2.10) simplifies to

$$c_a H' \phi_a \mathrm{e}^{-\mathrm{i}E_a t} + c_b H' \phi_b \mathrm{e}^{-\mathrm{i}E_b t} \quad = \quad \mathrm{i}\frac{dc_a}{dt}\phi_a \mathrm{e}^{-\mathrm{i}E_a t} + \mathrm{i}\frac{dc_b}{dt}\phi_b \mathrm{e}^{-\mathrm{i}E_b t}. \tag{2.11}$$

After multiplying equation (2.11) by $\langle \phi_a |$ we get

$$c_a \langle \phi_a | H' | \phi_a \rangle \mathrm{e}^{-\mathrm{i}E_a t} + c_b \langle \phi_a | H' | \phi_b \rangle \mathrm{e}^{-\mathrm{i}E_b t} \quad = \quad \mathrm{i}\frac{dc_a}{dt} \langle \phi_a | \phi_a \rangle \mathrm{e}^{-\mathrm{i}E_a t} + \mathrm{i}\frac{dc_b}{dt} \langle \phi_a | \phi_b \rangle \mathrm{e}^{-\mathrm{i}E_b t}. \tag{2.12}$$

Because eigenstates ϕ_a and ϕ_b are orthonormal ($\langle \phi_a | \phi_b \rangle = \delta_{ab}$) one gets

$$c_a \langle \phi_a | H' | \phi_a \rangle \mathrm{e}^{-\mathrm{i}E_a t} + c_b \langle \phi_a | H' | \phi_b \rangle \mathrm{e}^{-\mathrm{i}E_b t} \quad = \quad \mathrm{i}\frac{dc_a}{dt}\mathrm{e}^{-\mathrm{i}E_a t}. \tag{2.13}$$

One introduces the matrix elements of the perturbation $H'_{ab} = \langle \phi_a | H'(t) | \phi_b \rangle$, and reorder exponential factors

$$\frac{dc_a}{dt} = -\mathrm{i}\left(c_a H'_{aa} + c_b H'_{ab} \mathrm{e}^{-\mathrm{i}(E_b - E_a)t} \right). \tag{2.14}$$

By multiplying equation (2.11) by $\langle \phi_b |$ and using the same method, one obtains

$$\frac{dc_b}{dt} = -\mathrm{i}\left(c_b H'_{bb} + c_a H'_{ba} \mathrm{e}^{-\mathrm{i}(E_a - E_b)t} \right) \tag{2.15}$$

Equations (2.14) and (2.15) can be written in a matrix form

$$-\mathrm{i}\begin{pmatrix} H'_{aa} & H'_{ab}\mathrm{e}^{-\mathrm{i}(E_b - E_a)t} \\ H'_{ba}\mathrm{e}^{-\mathrm{i}(E_a - E_b)t} & H'_{bb} \end{pmatrix} \begin{pmatrix} c_a \\ c_b \end{pmatrix} \quad = \quad \frac{d}{dt}\begin{pmatrix} c_a \\ c_b \end{pmatrix} \tag{2.16}$$

If H' is small, then the matrix equation (2.16) can be solved by a process of successive approximation. In case of optical excitations the diagonal matrix elements $H'_{aa}(t)$ and $H'_{bb}(t)$ vanish because of the spatial dependence of the perturbation operator $H'(\mathbf{r}, t)$. Therefore equation (2.16) reduces to

$$\begin{cases} \dfrac{dc_a}{dt} = & -\mathrm{i}H'_{ab}\mathrm{e}^{-\mathrm{i}\omega_0 t}c_b, \\ \dfrac{dc_b}{dt} = & -\mathrm{i}H'_{ba}\mathrm{e}^{\mathrm{i}\omega_0 t}c_a, \end{cases} \tag{2.17}$$

where $\omega_0 = E_b - E_a$. Let's further assume that our two-level system was in the *ground state* at time $t = 0$, and that our energy levels E_a and E_b are not equal (to mimic the situation in optical spectroscopy). For instance if $E_a < E_b$, then we have to set

$$c_a(0) = 1, \quad c_b(0) = 0. \tag{2.18}$$

In the zeroth approximation $c_a(t)$ and $c_b(t)$

$$c_a^{(0)}(t) = 1, \quad c_b^{(0)}(t) = 0. \tag{2.19}$$

Let's put the zeroth approximation for $c_a(t)$ and $c_b(t)$ into equations (2.17)

$$\frac{dc_a^{(1)}}{dt} = 0, \Longrightarrow c_a^{(1)}(t) = 1, \tag{2.20}$$

$$\frac{dc_b^{(1)}}{dt} = -\mathrm{i}H'_{ba}\mathrm{e}^{\mathrm{i}\omega_0 t}c_a^{(0)}, \Longrightarrow c_b^1(t) = -\mathrm{i}\int_0^t dt' H'_{ba}(t')\mathrm{e}^{\mathrm{i}\omega_0 t'}. \tag{2.21}$$

The last equation shows that the occupation of level b is determined by the strength of coupling matrix element $H'_{ba}(t)$.

2.1.2 Transition Probability

Let's now consider an atom exposed to a monochromatic, spatially homogeneous electric field

$$\mathbf{E} = \mathbf{E}_0 \cos(\omega t). \tag{2.22}$$

If the light polarization is chosen along the $z-$axis, then the perturbing part of the Hamiltonian reads

$$H'(t) = -qE_0 z \cos(\omega t), \tag{2.23}$$

where q is the charge of the electron. The matrix element $H'_{ba}(t)$ will read

$$H'_{ba}(t) = -d_{ba}E_0 \cos(\omega t), \quad \text{where} \quad d_{ba} = q \langle \phi_b | z | \phi_a \rangle . \tag{2.24}$$

If an atom starts out in the lower state ϕ_a, and a polarized monochromatic beam is shinning on it, then occupation of the upper state ϕ_b is given by a transition probability

$$P_{a\to b}(t) = |c_b(t)|^2 \sim |V_{ab}|^2 \frac{\sin^2((\omega_0 - \omega)\frac{t}{2})}{(\omega_0 - \omega)^2}. \tag{2.25}$$

In order to derive the transition probability (2.25) we take the perturbation Hamiltonian (2.23) and use TDDPT to find the coefficient $c_b(t)$ in the first order (equation 2.21), inserting equation (2.24) in (2.21), one finds

$$c_b^{(1)}(t) = -\mathrm{i}V_{ba}\int_0^t \cos(\omega t')\mathrm{e}^{\mathrm{i}\omega_0 t'}\, dt', \tag{2.26}$$

$$\Longrightarrow c_b^{(1)}(t) = -\frac{\mathrm{i}V_{ba}}{2}\left(\frac{\mathrm{e}^{\mathrm{i}(\omega_0+\omega)t} - 1}{\omega_0 + \omega} + \frac{\mathrm{e}^{\mathrm{i}(\omega_0-\omega)t} - 1}{\omega_0 - \omega}\right). \tag{2.27}$$

If one assumes $\omega_0 + \omega \gg |\omega_0 - \omega|$, then occupation $c_b(t)$ is given by

$$c_b(t) \approx V_{ba} \frac{e^{i(\omega_0-\omega)\frac{t}{2}}}{\omega_0 - \omega} \sin((\omega_0 - \omega)\frac{t}{2}). \tag{2.28}$$

Therefore, the transition probability $P_{a\to b} = |c_b|^2$ reads

$$P_{a\to b} = |\mathbf{d}|^2 E_0^2 \frac{\sin^2((\omega_0-\omega)\frac{t}{2})}{(\omega_0-\omega)^2} \quad \text{where} \quad \mathbf{d} = q \langle \psi_b | \mathbf{r} | \psi_a \rangle . \tag{2.29}$$

This result should be interpreted as a probability of absorption of a photon of energy $E_a - E_b = \omega_0$.

2.1.3 Incoherent Perturbation

The transition probability found in the previous section assumes a monochromatic light. For polychromatic incoherent light, the net transition probability expressed in terms of the spatial distribution of the light $\rho(\omega)$ takes the form

$$P_{a\to b}(t) = 2|\mathbf{d}|^2 \int_0^\infty \rho(\omega) \frac{\sin^2((\omega_0-\omega)\frac{t}{2})}{(\omega_0-\omega)^2} d\omega \tag{2.30}$$

The function $\frac{\sin^2((\omega_0-\omega)\frac{t}{2})}{(\omega_0-\omega)^2}$ is sharply peaked about ω_0 whereas $\rho(\omega)$ is ordinarily quite broad $\Longrightarrow \rho(\omega) \sim \rho(\omega_0)$. Therefore equation (2.30) in the case of a system dominated by a single transition ω_0 can be simplified to

$$P_{a\to b}(t) = 2|\mathbf{d}|^2 \rho(\omega_0) \int_0^\infty \frac{\sin^2((\omega_0-\omega)\frac{t}{2})}{(\omega_0-\omega)^2} d\omega, \tag{2.31}$$

$$P_{a\to b}(t) = \pi |\mathbf{d}|^2 \rho(\omega_0) t. \tag{2.32}$$

The transition rate is then given by

$$R_{a\to b} = \frac{dP_{a\to b}}{dt} = \pi |\mathbf{d}|^2 \rho(\omega_0). \tag{2.33}$$

If we consider the general case of an incident non-polarized light coming from all directions, then we have to consider an averaged transition rate

$$R_{a\to b} = \frac{\pi |\mathbf{d}|^2}{3} \rho(\omega_0). \tag{2.34}$$

2.1.4 Einstein's Coefficients A and B

Consider a container of atoms N_a in the lower state $|\psi_a\rangle$, and N_b in the upper state $|\psi_b\rangle$. The Einstein's coefficients are the spontaneous emission rate A, the stimulated emission rate B_{ba} and the absorption rate B_{ab}. On the basis of the definitions of Einstein's coefficients, one can write the equation for occupations change of state b

$$\frac{dN_b}{dt} = -N_b A - N_b B_{ba} \rho(\omega_0) + N_a B_{ab} \rho(\omega_0), \tag{2.35}$$

In the thermal equilibrium $\frac{dN_b}{dt} = 0$ and equation (2.35) provides the values of the spectral density $\rho(\omega)$ at the transition energy ω_0

$$\Longrightarrow \rho(\omega_0) = \frac{A}{\frac{N_a}{N_b}B_{ab} - B_{ba}}. \tag{2.36}$$

From Boltzman statistics, one can write[16]

$$\frac{N_a}{N_b} = \frac{\mathrm{e}^{-\frac{E_a}{k_B T}}}{\mathrm{e}^{-\frac{E_b}{k_B T}}} = \mathrm{e}^{\frac{\omega_0}{k_B T}}, \Longrightarrow \rho(\omega_0) = \frac{A}{\mathrm{e}^{\frac{\omega_0}{k_B T}}B_{ab} - B_{ba}} \tag{2.37}$$

Moreover, Planck's black body radiation reads

$$\rho(\omega) = \frac{1}{\pi^2 c^3}\frac{\omega^3}{\mathrm{e}^{\frac{\omega_0}{k_B T}} - 1}. \tag{2.38}$$

Comparing equations (2.37) and (2.38), one concludes that $B_{ab} = B_{ba}$

$$A = \frac{\omega_0^3}{\pi^2 c^3}B_{ba}, \Longrightarrow A = \frac{\omega_0^3 |\mathbf{d}|^2}{3\pi c^3} \tag{2.39}$$

Moreover, $B_{ba}\rho(\omega_0) = R_{b\to a}$ and stimulated emission rate becomes related to the dipole matrix elements $d_{ba} = \langle\psi_b|\,\mathbf{d}\,|\psi_a\rangle$

$$\Longrightarrow B_{ba} = \frac{\pi}{3}|\mathbf{d}|^2. \tag{2.40}$$

2.1.5 Einstein's Coefficients and Absorption Cross Section

It can be shown that for transition from a state $|\psi_b\rangle$ to a state $|\psi_a\rangle$, the absorption cross section σ can be expressed by [17],

$$\sigma = \frac{1}{4}\lambda_0^2 A, \tag{2.41}$$

where spontaneous emission rate A is given by equation (2.39) and the wavelength of light $\lambda = \frac{2\pi c}{\omega_0}$. Elementary derivation then gives for absorption cross section

$$\sigma = \frac{\pi\omega_0 e^2}{3c}|\,\langle\psi_b|\,\mathbf{r}\,|\psi_a\rangle\,|^2. \tag{2.42}$$

In the case of several transitions, one will find

$$\sigma = \frac{\pi\omega_0}{3\varepsilon_0 c}\sum_i |d_i|^2, \tag{2.43}$$

where i is an index which runs over different transitions.
As we will see below that optical cross section is proportional to the trace of the imaginary part of a polarizability tensor P [18, 19]

$$\sigma(\omega) = -\frac{4\pi\omega}{3c}Im\left[P_{xx}(\omega) + P_{yy}(\omega) + P_{zz}(\omega)\right] \tag{2.44}$$

2.2 Solving the Many-Body Problem

The derivation in the last section is done only for one-particle systems. The many-body problem was not considered so far. The difficulty of this problem is not to find the equation of motion of the electrons, but to solve this equation. It is the famous non-relativistic many-body Hamiltonian

$$H = -\sum_i \frac{\nabla_i^2}{2m_e} - \sum_I \frac{\nabla_I^2}{2M_I} + \frac{1}{2}\sum_{i\neq j} \frac{1}{|\mathbf{r}_i - \mathbf{r}_j|} - \sum_{iI} \frac{Z_I}{|\mathbf{r}_i - \mathbf{R}_I|} + \frac{1}{2}\sum_{I\neq J} \frac{Z_I Z_J}{|\mathbf{R}_I - \mathbf{R}_J|}. \quad (2.45)$$

The small indices i, j run over electrons and the capital indices I, J run over nucleus. The equation (2.45) contains the kinetic energy terms of nucleus and electrons, plus the instantaneous Coulomb interaction between all pairs of bodies. The problem in many-body Quantum mechanics is to solve the corresponding SE equation. The solution would require in principle to diagonalize this equation in order to obtain the eigenvalues (energies) and the eigenfunctions (wave-functions ψ). Unfortunately, the wave-functions are functions of every particle variables $\psi(\mathbf{r}_1, \mathbf{r}_2, ..., \mathbf{R}_1, \mathbf{R}_2...)$. Therefore for a system of N particles, the wave-functions will be functions of $3N$ variables.

The only hope to solve the Schrödinger equation (2.45) is first to simplify its tremendous complexity for a multi dimensional wave-function. For this, a brief description of a Density Functional Theory (DFT) will be presented, then by including a time-dependent perturbation potential, we will touch upon the time-dependent density functional theory (TDDFT).

2.2.1 Density Functional Theory

2.2.1.1 The Thomas-Fermi Model

The idea of the DFT is to avoid the use of the full N-particle wave-function by using the much simpler electron density $n(\mathbf{r})$. The original idea came from the Thomas-Fermi model [20]. Llewellyn Thomas and Enrico Fermi realized that statistical considerations can be used to approximate the distribution of electrons in an atom. The assumptions stated by Thomas are that: "*Electrons are distributed uniformly in the six-dimensional phase space for the motion of an electron at the rate of two for each h^3 of volume*", and that there is an effective potential field that "*is itself determined by the nuclear charge and this distribution of electrons.*" From this assumptions, Thomas and Fermi derived that the ground state electron density must satisfy the variational principle[21],

$$\delta\left\{E_{TF}[n] - \mu_{TF}\left(\int n(\mathbf{r})d\mathbf{r} - N\right)\right\} = 0, \quad (2.46)$$

where $E_{TF}[n]$ is the energy of the atom in terms of electron density, $N = N[n(\mathbf{r})] = \int n(\mathbf{r})d\mathbf{r}$ is the total number of electrons in the atom, and μ_{TF} is defined by the Euler-Lagrange equation

$$\mu_{TF} = \frac{\delta E_{TF}[n]}{\delta n(\mathbf{r})}. \quad (2.47)$$

Unfortunately, the simple approximations $E_{TF}[n]$ for the total-energy density functional fail when it comes to molecules. This plus the fact that the accuracy for atoms is not high compared to other methods, caused the method to become viewed as an oversimplified model of not much real importance for quantitative predictions in atomic, molecular or solid-state physics.

2.2.1.2 The Hohenberg-Kohn Theorems

Hohenberg and Kohn showed that for ground states the Thomas-Fermi model may be regarded as an approximation to an exact theory, the Density Functional Theory [22]. There is an exact energy functional $E[n]$, as well as an exact variational principle of the form of equation (2.46).

The basic lemma of Hohenberg-Kohn (HK) theorem is that the ground state density $n(\mathbf{r})$ of a bound system of interacting electrons in some external potential $V(\mathbf{r})$ determines this potential uniquely. The original proof can be found in [22].

The most important property of an electronic ground state is its energy E. By wave-function methods E could be calculated either by direct approximate solution of the Schrödinger equation $H\psi = E\psi$ or from the Rayleigh-Ritz minimal principle

$$E = min_{\tilde{\psi}} \left\langle \tilde{\psi} \right| H \left| \tilde{\psi} \right\rangle, \tag{2.48}$$

where $\tilde{\psi}$ is a normalized trial function for the given number electrons N, and H is the total Hamiltonian of the system

$$H = T + U + V. \tag{2.49}$$

T is the kinetic energy, U the interaction energy and V is an external potential. The formulation of the minimal principle in terms of trial densities $\tilde{n}(\mathbf{r})$, rather than trial wave-function $\tilde{\psi}$ was first presented in [22]. Here, the derivation due to Levy and Lieb [23], called the constrained search method, will be succinctly presented.

Every trial function $\tilde{\psi}$ corresponds to a trial density $n(\mathbf{r})$ obtained by

$$\tilde{n}(\mathbf{r}) = N \int \tilde{\psi}^*(\mathbf{r}_1, \mathbf{r}_2, ..., \mathbf{r}_n)\tilde{\psi}(\mathbf{r}_1, \mathbf{r}_2, ..., \mathbf{r}_n)d\mathbf{r}_2...d\mathbf{r}_n \tag{2.50}$$

One may carry out the minimization of equation (2.48) in two stages. (i) In the first step, one fixes a trial $\tilde{n}(\mathbf{r})$ and denote by $\tilde{\psi}^{\alpha}_{\tilde{n}}$ the class of trial functions which deliver this $\tilde{n}$. The constrained energy minimum with $\tilde{n}(\mathbf{r})$ fixed is defined as

$$E_V[\tilde{n}(\mathbf{r})] = min_{\alpha} \left\langle \tilde{\psi}^{\alpha}_{\tilde{n}} \right| H \left| \tilde{\psi}^{\alpha}_{\tilde{n}} \right\rangle = \int V(\mathbf{r})\tilde{n}(\mathbf{r})d\mathbf{r} + F[\tilde{n}(\mathbf{r})], \tag{2.51}$$

where,

$$F[\tilde{n}(\mathbf{r})] = \min_{\alpha} \left\langle \tilde{\psi}^{\alpha}_{\tilde{n}} \right| T + U \left| \tilde{\psi}^{\alpha}_{\tilde{n}} \right\rangle. \tag{2.52}$$

The functional $F[\tilde{n}(\mathbf{r})]$ requires no explicit knowledge of external potential $V(\mathbf{r})$. It is an universal functional of the density $\tilde{n}(\mathbf{r})$.

(ii) In the second step, one minimizes the equation (2.51) over all $\tilde{n}$

$$E = \min_{\tilde{n}} E_V[\tilde{n}(\mathbf{r})] \tag{2.53}$$

$$= \min_{\tilde{n}} \left\{ \int V(\mathbf{r})\tilde{n}(\mathbf{r})d\mathbf{r} + F[\tilde{n}(\mathbf{r})] \right\}. \tag{2.54}$$

For a non-degenerate ground-state, the minimum is attained when $\tilde{n}(\mathbf{r})$ is the ground-state density. The HK minimum principle (equation (2.53)) may be considered as the formal justification of the Thomas-Fermi theory (equation (2.46)).

2.2.1.3 Hartree Equations

There are number of approximations in the electronic structure theory which may be considered as precursors of modern KS equations.
Below we recall one of the self consistent schemes- - -Hartree equations. Hartree proposed a set of self-consistent single-particle equations for the approximate description of the electronic structure of atoms. Every electron is regarded as moving in an effective single-particle potential

$$V_{\mathrm{H}}(\mathbf{r}) \;=\; -\frac{Z}{r} + \int \frac{n(\mathbf{r}')}{|\mathbf{r}-\mathbf{r}'|} d\mathbf{r}', \tag{2.55}$$

where the first term represents the potential due to a nuclei of atomic number Z and the second term is the potential due to the average electronic density distribution $n(\mathbf{r})$. Thus, each electron obeys a single-particle Schrödinger equation

$$\left\{ -\frac{1}{2}\nabla^2 + V_{\mathrm{H}}(\mathbf{r}) \right\} \varphi_j(\mathbf{r}) \;=\; \varepsilon_j \varphi_j(\mathbf{r}), \tag{2.56}$$

where j denotes both spatial as well as spin *quantum numbers*. The mean density is given by

$$n(\mathbf{r}) \;=\; 2\sum_{j=1}^{N} |\varphi_j(\mathbf{r})|^2, \tag{2.57}$$

where, in the ground state, the sum runs over the N lowest eigenvalues to respect the Pauli exclusion principle. Equations (2.55)–(2.57) are called the self-consistent Hartree equations. One may start from a first approximation for the density $n(\mathbf{r})$ (e.g. from TF theory), construct $V_H(\mathbf{r})$ according to equation (2.55), solve equation (2.56) for φ_j; and recalculate $n(\mathbf{r})$ from equation (2.57), which should be the same as the initial $n(\mathbf{r})$. If it is not one iterates appropriately until the self-consistency is achieved.

The Hartree differential equation (2.56) had the form of the Schrödinger equation for non-interacting electrons moving in the external potential V_{eff}. For such a system, the HK variational principle takes the form

$$E_{V(\mathbf{r})}[\tilde{n}] \;=\; \int V(\mathbf{r})\tilde{n}(\mathbf{r})d\mathbf{r} + T_S[\tilde{n}(\mathbf{r})] \geq E, \tag{2.58}$$

where $T_S[\tilde{n}(\mathbf{r})]$ is the kinetic energy of the ground state of non-interacting electrons with density distribution $\tilde{n}(r)$. Euler-Lagrange equations, embodying the fact that the expression (2.57) is stationary with respect to variation of $\tilde{n}(\mathbf{r})$ (which leaves the total number of electrons unchanged) read

$$\delta E_V[\tilde{n}(\mathbf{r})] \;=\; \int \delta\tilde{n}(\mathbf{r}) \left(V(\mathbf{r}) + \frac{\delta}{\delta\tilde{n}(\mathbf{r})} T_S[\tilde{n}(\mathbf{r})]|_{\tilde{n}=n} - \varepsilon \right) d\mathbf{r} = 0, \tag{2.59}$$

with $\tilde{n}(\mathbf{r})$ being the exact ground-state density for $V(\mathbf{r})$. Here ε is a Lagrange multiplier to assure particle conservation. Now in this soluble, non-interacting case we know that the ground-state energy and density

can be obtained by calculating the eigenfunction $\varphi_j(\mathbf{r})$ and eigenvalues ε_j of non-interacting, single particle equations

$$\left(-\frac{1}{2}\nabla^2 + V(\mathbf{r}) - \varepsilon_j\right)\varphi_j(\mathbf{r}) \quad = \quad 0, \tag{2.60}$$

yielding

$$E = \sum_{j=1}^{N} \varepsilon_j; \quad n(\mathbf{r}) = \sum_{j=1}^{N} |\varphi_j(\mathbf{r})|^2. \tag{2.61}$$

2.2.1.4 Reasoning Behind the KS Equations

Returning now to the problem of interacting electrons, which had previously been addressed approximately by the single-particle-like Hartree equations, Kohn and Sham wrote the functional $F[\tilde{n}(\mathbf{r})]$ of equation (2.52) in the form

$$F[\tilde{n}(\mathbf{r})] \quad = \quad T_S[\tilde{n}(\mathbf{r})] + \frac{1}{2}\int \frac{\tilde{n}(\mathbf{r})\tilde{n}(\mathbf{r}')}{|\mathbf{r}-\mathbf{r}'|} d\mathbf{r}d\mathbf{r}' + E_{\text{xc}}[\tilde{n}(\mathbf{r})], \tag{2.62}$$

where $T_S[\tilde{n}(\mathbf{r})]$ is the kinetic energy functional for non-interacting electrons. The last term $E_{\text{xc}}[\tilde{n}(\mathbf{r})]$ defines the exchange-correlation energy functional equation (2.62). The HK variational principle for interacting electrons now takes the form

$$E_V[\tilde{n}(\mathbf{r})] \quad = \quad \int V(\mathbf{r})\tilde{n}(\mathbf{r})d\mathbf{r} + T_S[\tilde{n}(\mathbf{r})] + \frac{1}{2}\int \frac{\tilde{n}(\mathbf{r})\tilde{n}(\mathbf{r}')}{|\mathbf{r}-\mathbf{r}'|} d\mathbf{r}d\mathbf{r}' + E_{\text{xc}}[\tilde{n}(\mathbf{r})] \geq E, \tag{2.63}$$

and the corresponding Euler-Lagrange equations, for a given total number of electrons has the form

$$\delta E_V[\tilde{n}(\mathbf{r})] \quad = \quad \int \delta\tilde{n}(\mathbf{r}) \left(V_{\text{eff}}(\mathbf{r}) + \frac{\delta}{\delta\tilde{n}(\mathbf{r})} T_S[\tilde{n}(\mathbf{r})]|_{\tilde{n}(\mathbf{r})=n(\mathbf{r})} - \varepsilon\right) d\mathbf{r} = 0. \tag{2.64}$$

Here

$$V_{\text{eff}}(\mathbf{r}) \quad = \quad V(\mathbf{r}) + \int \frac{n(\mathbf{r}')}{|\mathbf{r}-\mathbf{r}'|} d\mathbf{r}' + V_{\text{xc}}(\mathbf{r}), \tag{2.65}$$

and the local exchange-correlation potential Vxc is formally given by a functional derivative of exchange-correlation energy E_{xc}

$$V_{\text{xc}} \quad = \quad \frac{\delta}{\delta\tilde{n}(\mathbf{r})} E_{\text{xc}}[\tilde{n}(\mathbf{r})]|_{\tilde{n}(\mathbf{r})=n(\mathbf{r})}. \tag{2.66}$$

The form of equation (2.64) is identical to equation (2.59) for non-interacting particles moving in an effective external potential V_{eff} instead of $V(\mathbf{r})$, and so we can conclude that the minimizing density $n(\mathbf{r})$ is given by solving the single particle equation

$$\left(-\frac{1}{2}\nabla^2 + V_{\text{eff}}(\mathbf{r}) - \varepsilon_j\right)\varphi_j(\mathbf{r}) \quad = \quad 0, \tag{2.67}$$

with

$$n(\mathbf{r}) = 2\sum_{j=1}^{N}|\varphi_j(\mathbf{r})|^2, \tag{2.68}$$

$$V_{\text{eff}}(\mathbf{r}) = V(\mathbf{r}) + \int \frac{n(\mathbf{r}')}{|\mathbf{r}-\mathbf{r}'|}d\mathbf{r}' + V_{\text{xc}}(\mathbf{r}). \tag{2.69}$$

The exchange-correlation potential $V_{\text{xc}}(\mathbf{r})$ depends functionally on the entire density distribution $\tilde{n}(\mathbf{r})$. These self-consistent equations are called the Kohn-Sham (KS) equations. The ground-state energy is given by [14]

$$E = \sum_j \varepsilon_j + E_{\text{xc}}[n(\mathbf{r})] - \int V_{\text{xc}}(\mathbf{r})n(\mathbf{r})d\mathbf{r} - \frac{1}{2}\int \frac{n(\mathbf{r})n(\mathbf{r}')}{|\mathbf{r}-\mathbf{r}'|}d\mathbf{r}'. \tag{2.70}$$

If one neglects E_{xc} and V_{xc}, the KS equation (2.67) and (2.70) reduce to the self-consistent Hartree equations.

The KS theory may be regarded as an extension of Hartree theory. With the exact E_{xc} and V_{xc}, all many-body effects are in principle included. Clearly, this directs attention to the functional $E_{\text{xc}}[\tilde{n}(\mathbf{r})]$. The practical usefulness of ground-state DFT depends entirely on whether approximations for the functional $E_{\text{xc}}[\tilde{n}(\mathbf{r})]$ could be found which are at the same time sufficiently simple and sufficiently accurate. There are many approximations for $E_{\text{xc}}[\tilde{n}(\mathbf{r})]$ available in the literature

Local density approximation (LDA) [24],

Generalized gradient approximations [25],

Optimized effective potential [26],

Orbital dependent correlation functional [27].

In this work LDA functional will be used.

2.2.2 Time Dependent Density Functional Theory

One of the principal limitations of DFT is that it gives only access to the ground state as mentioned in the previous section. DFT is a time-independent theory, not generally applicable to problems involving time-dependent fields which we consider in this work.
The generalization of the basic formalism of DFT to the time dependent case has been given by Runge, Gross and Kohn [28].

Suppose having an N-electrons system, described by the Schrödinger equation

$$H(t)\,|\varphi\rangle = \mathrm{i}\frac{\partial}{\partial t}\,|\varphi\rangle\,, \tag{2.71}$$

with $H(t) = T + V_0 + V'(t) = -\frac{1}{2}\sum_i \nabla_i^2 + \sum_{i<j}\frac{1}{|\mathbf{r}_i-\mathbf{r}_j|} + \sum_i V_{\text{ext}}(\mathbf{r}_i, t)$ sum of the kinetic energy, Coulomb potential and external (time-dependent) potential. Runge and Gross showed that the densities $n(\mathbf{r}, t)$ and $n'(\mathbf{r}, t)$ evolving from the common initial state $\varphi(t_0) = \varphi_0$ under the influence of two external potential $V_{\text{ext}}(\mathbf{r}, t)$ and $V'(\mathbf{r}, t)$, both Taylor expandable around t_0, are always different providing that the external potentials differ by more than a purely time-dependent function $c(t)$. This is the time-dependent analogue

of the HK theorem described in section 2.2.1.2. As a consequence, the time-dependent density uniquely determines the external potential (up to a purely time-dependent function $c(t)$). On the other hand, the potential determines the time-dependent wave-function, unique functional of the density up to a purely time-dependent phase

$$\varphi(t) \quad = \quad \mathrm{e}^{-\mathrm{i}\alpha(t)}\varphi[n,\varphi_0](t). \tag{2.72}$$

So for an operator $\hat{O}(t)$, which is a function of time, but not of any derivative or integral operators on t, this phase factor cancels out when taking the expectation value, which is hence a unique functional of the density

$$\left\langle \varphi(t) \right| \hat{O}(t) \left| \varphi(t) \right\rangle \quad = \quad O[n](t). \tag{2.73}$$

The analogue of the second HK theorem, where the Rayleigh-Ritz minimum principle is used for the total energy, is given by the time dependent theory by the stationary principle of the Hamiltonian action integral, as no minimum energy principle is available. In fact, in quantum mechanics the time-dependent Schrödinger equation, with the initial condition $\varphi(t_0) = \varphi_0$ corresponds to a stationary (not necessarily minimum) point of the quantum mechanical action integral

$$E \quad = \quad \int_{t_0}^{t_1} dt \left\langle \varphi(t) \right| \mathrm{i}\frac{\partial}{\partial t} - H(t) \left| \varphi(t) \right\rangle, \tag{2.74}$$

where E is a functional of the density and has a stationary point at the correct time-dependent density. This density can hence be obtained by solving the Euler equation

$$\frac{\delta E}{\delta n(\mathbf{r},t)} \quad = \quad 0. \tag{2.75}$$

with appropriate initial conditions. Now, exactly like for the time-independent case, the functional E reads

$$E[n] \quad = \quad F[n] - \int_{t_0}^{t_1} dt \int d\mathbf{r} n(\mathbf{r},t) V_{\mathrm{ext}}(\mathbf{r},t). \tag{2.76}$$

Here the universal functional $F[n]$ is given by

$$F[n] \quad = \quad \int_{t_0}^{t_1} dt \left\langle \varphi(t) \right| \mathrm{i}\frac{\partial}{\partial t} - T - V_{\mathrm{Hxc}} \left| \varphi(t) \right\rangle. \tag{2.77}$$

As for the time-independent DFT one can define a Kohn-Sham scheme by introducing a non-interacting system with exactly the same density $n(\mathbf{r},t)$. Once the v-representability of the time-dependent density is proven [29], we can apply the stationary condition to equation (2.76) under the condition

$$n(\mathbf{r},t) \quad = \quad 2\sum_i |\varphi_i(\mathbf{r},t)|^2, \tag{2.78}$$

in order to obtain the time-dependent Kohn-Sham equations

$$\left[-\frac{1}{2}\nabla^2 + V_{\text{eff}}(\mathbf{r},t)\right]\varphi_i(\mathbf{r},t) \quad = \quad \mathrm{i}\frac{\partial}{\partial t}\varphi_i(\mathbf{r},t). \tag{2.79}$$

Here effective time-dependent potential

$$V_{\text{eff}}(\mathbf{r},t) \quad = \quad V_{\text{ext}}(\mathbf{r},t) + \int \frac{n(\mathbf{r}',t)}{|\mathbf{r}-\mathbf{r}'|}d\mathbf{r}' + V_{\text{xc}}(\mathbf{r},t) \tag{2.80}$$

is analogous to equation (2.69).

2.3 Electric Field Enhancement in a Cavity

The aim of this work is to study the electric field distribution and enhancement between two metallic clusters. Now, the derivation of this enhancement will be presented from the perspective of linear response TDDFT.

2.3.1 Response Function Formulation

First of all, the density change needs to be derived in order to find the field enhancement. This derivation will be done for one electron, and will be generalized to several electrons.
The time-dependent SE reads

$$\left(\mathrm{i}\frac{\partial}{\partial t} - H_0 - \delta V_{\text{ext}}\right)\psi(\mathbf{r},t) \quad = \quad 0, \tag{2.81}$$

where H_0 is the time-independent Hamiltonian without external perturbation and δV_{ext} is the time-dependent perturbation. Provided $\delta V_{\text{ext}}(\mathbf{r},t)$ is small we adopt perturbation theory ansatz for $\psi(\mathbf{r},t)$

$$\psi(\mathbf{r},t) \quad = \quad \psi_0(\mathbf{r},t) + \delta\psi(\mathbf{r},t), \tag{2.82}$$

where $\psi_0(\mathbf{r},t)$ fulfill the time-independent Schrödinger equation

$$\left(\mathrm{i}\frac{\partial}{\partial t} - H_0\right)\psi_0(\mathbf{r},t) \quad = \quad 0, \tag{2.83}$$

$$\Longrightarrow \left(\mathrm{i}\frac{\partial}{\partial t} - H_0 - \delta V_{\text{ext}}\right)\psi_0(\mathbf{r},t) \quad + \quad \left(\mathrm{i}\frac{\partial}{\partial t} - H_0 - \delta V_{\text{ext}}\right)\delta\psi(\mathbf{r},t) = 0. \tag{2.84}$$

By using (2.83) and by neglecting second order terms, one get

$$-\delta V_{\text{ext}}\psi_0(\mathbf{r},t) + \left(\mathrm{i}\frac{\partial}{\partial t} - H_0\right)\delta\psi(\mathbf{r},t) \quad = \quad 0, \tag{2.85}$$

$$\Longleftrightarrow \left(\mathrm{i}\frac{\partial}{\partial t} - H_0\right)\delta\psi(\mathbf{r},t) \quad = \quad \delta V_{\text{ext}}\psi_0(\mathbf{r},t), \tag{2.86}$$

Green's functions can be used to solve equation (2.86)

$$\left(\mathrm{i}\frac{\partial}{\partial t} - H_0\right) G(\mathbf{r}t, \mathbf{r}'t') = \delta(\mathbf{r}-\mathbf{r}')\delta(t-t'), \tag{2.87}$$

$$\iff \int \left(\mathrm{i}\frac{\partial}{\partial t} - H_0\right) G(\mathbf{r}t, \mathbf{r}'t')\delta V_{\mathrm{ext}}(\mathbf{r}', t')\psi_0(\mathbf{r}', t')d\mathbf{r}'dt' = \int \delta(\mathbf{r}-\mathbf{r}')\delta(t-t')\delta V_{\mathrm{ext}}(\mathbf{r}', t')\psi_0(\mathbf{r}', t')d\mathbf{r}'dt', \tag{2.88}$$

$$\iff \left(\mathrm{i}\frac{\partial}{\partial t} - H_0\right) \int G(\mathbf{r}t, \mathbf{r}'t')\delta V_{\mathrm{ext}}(\mathbf{r}', t')\psi_0(\mathbf{r}', t')d\mathbf{r}'dt' = \delta V_{\mathrm{ext}}(\mathbf{r}, t)\psi_0(\mathbf{r}, t). \tag{2.89}$$

But from (2.86) one gets

$$\iff \left(\mathrm{i}\frac{\partial}{\partial t} - H_0\right) \int G(\mathbf{r}t, \mathbf{r}'t')\delta V_{\mathrm{ext}}(\mathbf{r}', t')\psi_0(\mathbf{r}', t')d\mathbf{r}'dt' = \left(\mathrm{i}\frac{\partial}{\partial t} - H_0\right) \delta\psi(\mathbf{r}, t), \tag{2.90}$$

$$\implies \delta\psi(\mathbf{r}, t) = \int G(\mathbf{r}t, \mathbf{r}'t')\delta V_{\mathrm{ext}}(\mathbf{r}', t')\psi_0(\mathbf{r}', t')d\mathbf{r}'dt'. \tag{2.91}$$

For one electron, the density is

$$n(\mathbf{r}, t) = \psi_0^*(\mathbf{r}, t)\psi_0(\mathbf{r}, t), \tag{2.92}$$

$$\implies n(\mathbf{r}, t) + \delta n(\mathbf{r}, t) = \left(\psi_0^* + \delta\psi^*\right)\left(\psi_0 + \delta\psi\right), \tag{2.93}$$

$$\iff \delta n(\mathbf{r}, t) = \psi_0^*\delta\psi + \delta\psi^*\psi_0, \tag{2.94}$$

$$= 2\mathbb{R}(\psi_0^*\delta\psi), \tag{2.95}$$

$$\iff \delta n(\mathbf{r}, t) = \psi_0^*(\mathbf{r}, t) \int G(\mathbf{r}t, \mathbf{r}'t')\delta V_{\mathrm{ext}}(\mathbf{r}', t')\psi_0(\mathbf{r}', t')d\mathbf{r}'dt' + \mathrm{cc}, \tag{2.96}$$

with cc meaning the complex conjugate. But the linear density change to a perturbation $\delta V_{\mathrm{ext}}(\mathbf{r}', t')$ is given by [30]

$$\delta n(\mathbf{r}, t) = \int \chi(\mathbf{r}t, \mathbf{r}'t')\delta V_{\mathrm{ext}}(\mathbf{r}', t')d\mathbf{r}'dt', \tag{2.97}$$

where $\chi(\mathbf{r}t, \mathbf{r}'t')$ is the so called interacting response function. In frequency space, one gets the following relations

$$\begin{cases} \delta n(\mathbf{r}, \omega) = \int \chi(\mathbf{r}, \mathbf{r}', \omega)\delta V_{\mathrm{ext}}(\mathbf{r}', \omega)d\mathbf{r}', \\ \delta n(\mathbf{r}, \omega) = \int \chi_0(\mathbf{r}, \mathbf{r}', \omega)\delta V_{\mathrm{eff}}(\mathbf{r}', \omega)d\mathbf{r}'. \end{cases} \tag{2.98}$$

Here $\chi_0(\mathbf{r}, \mathbf{r}', \omega)$ is the so called density response function and $\delta V_{\mathrm{eff}} = \delta V_{\mathrm{ext}} + \delta V_{\mathrm{Hxc}}$ with δV_{Hxc} the perturbation of effective interaction potential V_{Hxc}. Comparing ansatz (2.97) with equation (2.96), we can obtain an expression for non-interaction density response

$$\chi_0(\mathbf{r}t, \mathbf{r}'t') = \psi_0^*(\mathbf{r}, t)G(\mathbf{r}t, \mathbf{r}'t')\psi_0(\mathbf{r}', t'). \tag{2.99}$$

Thus, to find χ_0, it is necessary to find G. The Green function obeys equation (2.87), whose the solution is given by [31]

$$G(\mathbf{r}t,\mathbf{r}'t') = -\mathrm{i}\sum_n \phi_n(\mathbf{r})\phi_n^*(\mathbf{r}')\mathrm{e}^{-\mathrm{i}(E_n\pm\mathrm{i}\varepsilon)(t-t')}\theta_\pm(t-t'), \tag{2.100}$$

Where

$$\theta_+(x) = \begin{cases} 0 & \text{if} \quad x>0, \\ -1 & \text{if} \quad x<0, \end{cases} \quad \text{and} \quad \theta_-(x) = \begin{cases} 1 & \text{if} \quad x>0, \\ 0 & \text{if} \quad x<0. \end{cases} \tag{2.101}$$

By doing Fourier transform of (2.99) we get

$$\chi(\mathbf{r},\mathbf{r}',\omega) = \sum_{m>0}\frac{\psi_0^*(\mathbf{r})\psi_m(\mathbf{r})\psi_m^*(\mathbf{r}')\psi_0(\mathbf{r}')}{\omega-(E_0-E_m)+\mathrm{i}\varepsilon} - \frac{\psi_m^*(\mathbf{r})\psi_0(\mathbf{r})\psi_0^*(\mathbf{r}')\psi_m(\mathbf{r}')}{\omega-(E_m-E_0)+\mathrm{i}\varepsilon}. \tag{2.102}$$

For several electrons, one finds

$$\chi(\mathbf{r},\mathbf{r}',\omega) = \sum_{n,m}(f_n-f_m)\frac{\psi_n^*(\mathbf{r})\psi_m(\mathbf{r})\psi_m^*(\mathbf{r}')\psi_n(\mathbf{r}')}{\omega-(E_n-E_m)+\mathrm{i}\varepsilon}, \tag{2.103}$$

with (n,m) indices over the states. f_n and f_m are the occupation terms. If n and m are occupied or unoccupied states, $f_n - f_m = 0$, otherwise $f_n - f_m \neq 0$. Equations (2.98) can be written as variational derivatives of $\delta n(\mathbf{r},\omega)$

$$\begin{cases} \chi_0(\mathbf{r},\mathbf{r}',\omega) = \dfrac{\delta n(\mathbf{r},\omega)}{\delta V_{\mathrm{eff}}(\mathbf{r}',\omega)}, \\ \chi(\mathbf{r},\mathbf{r}',\omega) = \dfrac{\delta n(\mathbf{r},\omega)}{\delta V_{\mathrm{ext}(\mathbf{r}',\omega)}}. \end{cases} \tag{2.104}$$

Thus,

$$\chi_0^{-1}(\mathbf{r},\mathbf{r}',\omega) = \frac{\delta V_{\mathrm{eff}}(\mathbf{r},\omega)}{\delta n(\mathbf{r}',\omega)} \quad \text{and} \quad \chi^{-1}(\mathbf{r},\mathbf{r}',\omega) = \frac{\delta V_{\mathrm{ext}}(\mathbf{r},\omega)}{\delta n(\mathbf{r}',\omega)}, \tag{2.105}$$

rewriting equation (2.80) as $V_{\mathrm{eff}} = V_{\mathrm{ext}} + V_{\mathrm{Hxc}}$ and taking the variational derivative of $\delta n(\mathbf{r},\omega)$

$$\frac{\delta V_{\mathrm{eff}}(\mathbf{r},\omega)}{\delta n(\mathbf{r},\omega)} = \frac{\delta V_{\mathrm{ext}}(\mathbf{r},\omega)}{\delta n(\mathbf{r},\omega)} + \frac{\delta V_{\mathrm{Hxc}}(\mathbf{r},\omega)}{\delta n(\mathbf{r},\omega)}. \tag{2.106}$$

Comparing equation (2.106) with equation (2.105), one gets

$$\chi_0^{-1}(\mathbf{r},\mathbf{r}',\omega) = \frac{\delta V_{\mathrm{Hxc}}(\mathbf{r},\omega)}{\delta n(\mathbf{r},\omega)} + \chi^{-1}(\mathbf{r},\mathbf{r}',\omega), \tag{2.107}$$

$$\chi_0^{-1}(\mathbf{r},\mathbf{r}',\omega) = K(\mathbf{r},\mathbf{r}',\omega) + \chi^{-1}(\mathbf{r},\mathbf{r}',\omega), \tag{2.108}$$

$$\Longrightarrow \chi(\mathbf{r},\mathbf{r}',\omega) = \left[\chi_0^{-1}(\mathbf{r},\mathbf{r}',\omega) - K(\mathbf{r},\mathbf{r}',\omega)\right]^{-1}. \tag{2.109}$$

Here $K = \frac{\delta V_{\mathrm{Hxc}}(\mathbf{r},\omega)}{\delta n(\mathbf{r},\omega)}$ is the TDDFT kernel.

Furthermore,

$$\left(\chi_0^{-1}(\mathbf{r},\mathbf{r}',\omega) - K(\mathbf{r},\mathbf{r}',\omega)\right)^{-1} = \left[\chi_0^{-1}(\mathbf{r},\mathbf{r}',\omega)\left(1-\chi_0(\mathbf{r},\mathbf{r}',\omega)K(\mathbf{r},\mathbf{r}',\omega)\right)\right]^{-1}, \tag{2.110}$$

$$\iff \chi(\mathbf{r},\mathbf{r}',\omega) = \chi_0(\mathbf{r},\mathbf{r}',\omega)\left[1-\chi_0(\mathbf{r},\mathbf{r}',\omega)K(\mathbf{r},\mathbf{r}',\omega)\right]^{-1}. \tag{2.111}$$

Inserting equation (2.109) into equation (2.111)

$$1 = \chi_0^{-1}(\mathbf{r},\mathbf{r}',\omega)\chi(\mathbf{r},\mathbf{r}',\omega) - K(\mathbf{r},\mathbf{r}',\omega)\chi(\mathbf{r},\mathbf{r}',\omega), \tag{2.112}$$

$$\chi_0(\mathbf{r},\mathbf{r}',\omega) = \chi(\mathbf{r},\mathbf{r}',\omega) - \chi_0(\mathbf{r},\mathbf{r}',\omega)K(\mathbf{r},\mathbf{r}',\omega)\chi(\mathbf{r},\mathbf{r}',\omega), \tag{2.113}$$

$$\implies \chi(\mathbf{r},\mathbf{r}',\omega) = \chi_0(\mathbf{r},\mathbf{r}',\omega) + \chi_0(\mathbf{r},\mathbf{r}',\omega)K(\mathbf{r},\mathbf{r}',\omega)\chi(\mathbf{r},\mathbf{r}',\omega). \tag{2.114}$$

2.3.2 Polarizability in Linear Response TDDFT

Using the dipole approximation, the external potential becomes connected to the electric field by $\delta V_{\text{ext}} = \mathbf{r}\mathbf{E}_{\text{ext}}$ and the polarizability tensor emerges

$$P_{ij}(\omega) = \int \mathbf{r}_i \chi(\mathbf{r},\mathbf{r}',\omega)\mathbf{r}_j d\mathbf{r} d\mathbf{r}' \tag{2.115}$$

The trace of the polarizability is proportional to the optical cross section as shown in equation (2.44). Since, we want to look into the spatial characteristics of the optical absorption, we will also analyze the induced density (2.98) due to the external field $\mathbf{E}_{\text{ext}}(\omega)$. The density change depends on the direction of the external electrical field (polarization) and on its frequency

$$\delta n(\mathbf{r},\omega,\mathbf{E}_{\text{ext}}) = -\int \chi(\mathbf{r},\mathbf{r}',\omega)\left(\mathbf{r}'.\mathbf{E}_{\text{ext}}\right) d\mathbf{r}' \tag{2.116}$$

The induced density provides spatial maps that characterize the spatial and frequency dependence of net density change.

Introducing a basis of dominant products into equation (2.114) (see appendix A)

$$\chi_{\mu\nu}(\omega) = \chi^0_{\mu\nu}(\omega) + \sum_{\mu'\nu'} \chi^0_{\mu\mu'}(\omega) K^{\mu'\nu'}_{\text{Hxc}} \chi_{\nu'\nu}(\omega) \tag{2.117}$$

we obtain an equation for expansion coefficients $\chi_{\mu\nu}(\omega)$ of interacting response function, where $K^{\mu\nu}_{\text{Hxc}}$ are the matrix elements of the Hartree-exchange-correlation kernel $K_{\text{Hxc}}(\mathbf{r},\mathbf{r}')$ between dominant products $F^{\mu}(\mathbf{r})$. Solving equation (2.105) against $\chi_{\mu\nu}(\omega)$, one could determine the interacting response function $\chi(\mathbf{r},\mathbf{r}',\omega)$. Setting the external potential to $\delta V_{\text{ext}} = \mathbf{r}\mathbf{E}_{\text{ext}}$, and inserting equation (2.114) into equation (2.98) with the basis of dominant products given in equation (A.6), and by defining the dipole moment as

$$\mathbf{d}^{\mu}(\mathbf{r}) = \int F^{\mu}(\mathbf{r}')\mathbf{r}' d^3\mathbf{r}', \tag{2.118}$$

then equation (2.116) is written as

$$\delta n(\mathbf{r},\omega) = F^{\mu}(\mathbf{r})\left(\delta \mathbf{n}_{\mu}(\mathbf{r},\omega).\mathbf{E}_{\text{ext}}\right) \tag{2.119}$$

where the vector $\delta\mathbf{n}_\mu(\omega) = \left[(1-\chi_0 K)^{-1}\chi_0\right]_{\mu\nu}\mathbf{d}^\mu$. Which can be rewritten in the form of a matrix equation

$$[1-\chi_0(\omega)K(\omega)]\,\delta\mathbf{n}_\mu(\omega) \;=\; \chi_0(\omega)\mathbf{d}^\nu. \tag{2.120}$$

Calculation of both the polarizability tensor (2.115) as well as the density change (2.116) is done at a much lower computational cost using an iterative approach [32]. The calculation is straightforward in this approach, because expansion coefficients of density change are determined in the basis of dominant products $\delta n_\mu(\omega,\mathbf{E})$ during calculation of the polarizability tensor (equation 2.115). The real-space quantity $\delta n(\mathbf{r},\omega,\mathbf{E})$ is then recovered on a 3D grid of points. From this real-space representation of the density change, the electric field distribution is determined as explained in the next section.

2.3.3 Enhancement for a Monochromatic Field

Let's now derive the time average of the power density of induced electrical field

$$P(\omega_0) \;=\; \frac{1}{T}\int_0^T \delta\mathbf{E}_{\text{ind}}(t)\delta\mathbf{E}^*_{\text{ind}}dt, \tag{2.121}$$

where ω_0 is the frequency of the incident monochromatic field, $\delta\mathbf{E}_{\text{ind}}(t)$ is the electrical field generated by the induced density $\delta n(\mathbf{r},t)$.

Lets assume a monochromatic field, homogeneous with a simple cosine dependence on time

$$\mathbf{E}(t) \;=\; \mathbf{E}_0\cos(\omega_0 t) = \frac{\mathbf{E}_0}{2}\left(\mathrm{e}^{\mathrm{i}\omega_0 t}+\mathrm{e}^{-\mathrm{i}\omega_0 t}\right). \tag{2.122}$$

In the frequency domain, the cosine field reads

$$\mathbf{E}(\omega) \;=\; \frac{\mathbf{E}_0}{2}\left(\delta(\omega-\omega_0)+\delta(\omega+\omega_0)\right). \tag{2.123}$$

The scalar potential of the homogeneous field is given by the scalar product $\delta V_{\text{ext}}(\mathbf{r},\omega) = -\mathbf{r}\mathbf{E}_{\text{ext}}(\omega)$. Therefore, from equation (2.97), one can find the form of the induced density for a monochromatic field

$$\delta n(\mathbf{r},t) \;=\; \int d\mathbf{r}'\int_{-\infty}^{+\infty}\chi(\mathbf{r},\mathbf{r}',\omega)\delta V_{\text{ext}}(\mathbf{r}',\omega)\mathrm{e}^{\mathrm{i}\omega t}d\omega, \tag{2.124}$$

$$\Longleftrightarrow \delta n(\mathbf{r},t) \;=\; \int d\mathbf{r}'\int_{-\infty}^{+\infty}\chi(\mathbf{r},\mathbf{r}',\omega)\frac{\mathbf{r}'\mathbf{E}_0}{2}\left(\delta(\omega-\omega_0)+\delta(\omega+\omega_0)\right)\mathrm{e}^{\mathrm{i}\omega t}d\omega, \tag{2.125}$$

$$\Longleftrightarrow \delta n(\mathbf{r},t) \;=\; \int\left(\chi(\mathbf{r},\mathbf{r}',\omega_0)\mathrm{e}^{\mathrm{i}\omega_0 t}+\chi(\mathbf{r},\mathbf{r}',-\omega_0)\mathrm{e}^{-\mathrm{i}\omega_0 t}\right)\frac{\mathbf{r}'\mathbf{E}_0}{2}d\mathbf{r}'. \tag{2.126}$$

For the sake of brevity, lets expel spatial variables from equations below

$$\Longrightarrow \delta n(t) \;=\; \left(\chi(\omega_0)\mathrm{e}^{i\omega_0 t}+\chi(-\omega_0)\mathrm{e}^{-\mathrm{i}\omega_0 t}\right)\frac{E_0}{2}. \tag{2.127}$$

The temporal dependence of the induced electrical field is going to be

$$\delta\mathbf{E}_{\text{ind}}(t) \;=\; \left(\chi(\omega_0)\mathrm{e}^{\mathrm{i}\omega_0 t}+\chi(-\omega_0)\mathrm{e}^{-\mathrm{i}\omega_0 t}\right)\frac{\mathbf{E}_0}{2}. \tag{2.128}$$

Let's separate $\chi(\omega_0)$ in real and imaginary part $\chi(\omega_0) = \chi'(\omega_0) + \mathrm{i}\chi''(\omega_0)$

$$\implies \delta\mathbf{E}_{\mathrm{ind}}(t) = \left[\left(\chi'(\omega_0) + \mathrm{i}\chi''(\omega_0)\right)\mathrm{e}^{\mathrm{i}\omega_0 t} + \left(\chi'(-\omega_0) + \mathrm{i}\chi''(-\omega_0)\right)\mathrm{e}^{-\mathrm{i}\omega_0 t}\right]\frac{\mathbf{E}_0}{2}. \tag{2.129}$$

The real part of the density response is even in frequency, while the imaginary part is odd, thus

$$\implies \delta\mathbf{E}_{\mathrm{ind}}(t) = \left[\left(\chi'(\omega_0) + \mathrm{i}\chi''(\omega_0)\right)\mathrm{e}^{\mathrm{i}\omega_0 t} + \left(\chi'(\omega_0) - \mathrm{i}\chi''(\omega_0)\right)\mathrm{e}^{-\mathrm{i}\omega_0 t}\right]\frac{\mathbf{E}_0}{2}, \tag{2.130}$$

$$\iff \delta\mathbf{E}_{\mathrm{ind}}(t) = \left(\chi'(\omega_0)\cos(\omega_0 t) + \mathrm{i}\chi''(\omega_0)\sin(\omega_0 t)\right)\mathbf{E}_0. \tag{2.131}$$

Now it is easier to compute the average power density given in equation (2.121)

$$\begin{aligned} P(\omega_0) = \frac{1}{T}\int_0^T & \left(\chi'(\omega_0)\cos(\omega_0 t) + i\chi''(\omega_0)\sin(\omega_0 t)\right) \\ & \left(\chi'(\omega_0)\cos(\omega_0 t) - i\chi''(\omega_0)\sin(\omega_0 t)\right)\mathbf{E}_0^2 dt, \end{aligned} \tag{2.132}$$

$$\iff P(\omega_0) = \frac{1}{T}\int_0^T \left(\chi'^2(\omega_0)\cos^2(\omega_0 t) + \chi''^2(\omega_0)\sin^2(\omega_0 t)\right)\mathbf{E}_0^2 dt, \tag{2.133}$$

$$\iff P(\omega_0) = \left(\chi'^2(\omega_0) + \chi''^2(\omega_0)\right)\frac{\mathbf{E}_0^2}{2}. \tag{2.134}$$

The enhancement is given by a ratio R of intensities of the induced and external field, i.e.

$$R(\omega_0) = \chi'^2(\omega_0) + \chi''^2(\omega_0). \tag{2.135}$$

The ratio $R(\omega)$ is the quantity that we characterize in this work.

2.3.4 Spatial Distribution of the Induced Electric Field

The spatial distribution of the induced electric field in response to a monochromatic external field is given by

$$\mathbf{E}_{\mathrm{ind}}(\mathbf{r}) = -\int \frac{(\mathbf{r} - \mathbf{r}')}{|\mathbf{r} - \mathbf{r}'|^3}\delta n(\mathbf{r}')d^3\mathbf{r}', \tag{2.136}$$

where $\delta n(\mathbf{r})$ is the induced density change at a given frequency. For plotting purposes we will compute $\mathbf{E}_{\mathrm{ind}}(\mathbf{r})$ on a 3D equidistant grid. Direct evaluation of the integral (2.136) takes $N_E.N_n$ operations where N_E is number of points at which we evaluate electric field and N_n is the number of points used to represent the density change with a sufficient accuracy. Because the number of points N_E and N_n can be rather large, the direct evaluation of Coulomb field is impractical. Instead, we will apply the convolution theorem to the Coulomb field (2.136) and use *Fast Fourier Transform* (FFT) to compute involved Fourier transform (FT) provide by the FFTW libraries. As it can be easily seen, the Coulomb field (2.136) is a convolution of the two functions

$$\mathbf{E}_{\mathrm{ind}}(\mathbf{r}) = -\frac{\mathbf{r}}{|\mathbf{r}|^3} \bigotimes \delta n(\mathbf{r}). \tag{2.137}$$

The convolution theorem reads

$$\mathrm{FT}\left[\mathbf{E}_{\mathrm{ind}}(\mathbf{r})\right] \quad = \quad -\mathrm{FT}\left[\frac{\mathbf{r}}{|\mathbf{r}|^3}\right].\mathrm{FT}\left[\delta n(\mathbf{r})\right]. \tag{2.138}$$

i.e. FT of a convolution is given by the product of FTs of the function. The last equation can be rewritten by using the inverse Fourier Transform FT^{-1}

$$\mathbf{E}_{\mathrm{ind}}(\mathbf{r}) \quad = \quad -\mathrm{FT}^{-1}\left(\mathrm{FT}\left[\frac{\mathbf{r}}{|\mathbf{r}|^3}\right].\mathrm{FT}\left[\delta n(\mathbf{r})\right]\right). \tag{2.139}$$

Evaluation of FT with FFT methods takes only N operations where N is the number of points at which one has input function.

In order to avoid Coulomb singularity, we evaluate electric field at the points which are shifted relative to the points on which density change is given. In order to get a balanced contribution of density at the nearest neighbor points, we shift the grids by half of the grid space in each direction. The sketch of such setting of grids in the 2D case is shown in the figure 2.3.1

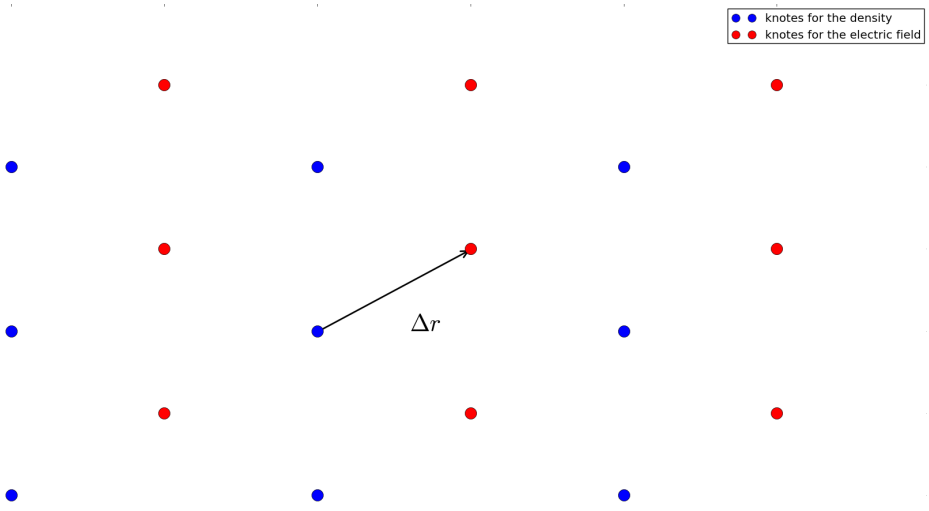

Figure 2.3.1: 2D representation of the spatial grid of the density(blue dots) and the electric field(red dots). The red dots are shifted of $\Delta\mathbf{r}$ compared to the blue dots in order to eliminate the singularity present in $\frac{|\mathbf{r}-\mathbf{r}'|}{|\mathbf{r}-\mathbf{r}'|^3}$ in equation 2.136 and get a balanced contribution from the neighboring points.

2.4 Simple Dipole Model

To get a good understanding of the calculations presented in the next chapter, we study in this section a simple model composed of 2 molecules that can be seen as two interacting dipoles separated by a distance d in a homogeneous, isotropic and linear media. For one dipole, the polarization $\boldsymbol{\mu}$ is written

$$\boldsymbol{\mu} \quad = \quad P\mathbf{E}_{\mathrm{tot}}, \tag{2.140}$$

where $\mathbf{E}_{\mathrm{tot}} = \mathbf{E}_{\mathrm{ext}} + \mathbf{E}_{\mathrm{ind}}$ is the total electric field, $\mathbf{E}_{\mathrm{ind}}$ is the induced electric field and $\mathbf{E}_{\mathrm{ext}}$ is the external perturbation. And P is the polarizability tensor

$$P = \begin{pmatrix} P_{xx} & P_{xy} & P_{xz} \\ P_{yx} & P_{yy} & P_{yz} \\ P_{zx} & P_{zy} & P_{zz} \end{pmatrix}. \tag{2.141}$$

In an homogeneous, isotropic and linear media the Drude-Lorentz model give [16]

$$P_{ij} = \begin{cases} \dfrac{P_0}{\omega^2 - \omega_0^2 + \mathrm{i}\gamma} & \text{if} \quad i = j, \\ 0 & \text{otherwise,} \end{cases} \tag{2.142}$$

where ω_0 is the resonance frequency and γ is the damping. In our small model $\omega_0 = 2.0\,\mathrm{eV}$ and $\gamma = 0.1\,\mathrm{eV}$. In the case of two dipoles, the polarization of the first dipole is

$$\boldsymbol{\mu}_1 = P\left(\mathbf{E}_{\text{ext}} + A\boldsymbol{\mu}_2\right). \tag{2.143}$$

Here A is the dipole interaction matrix

$$A_{ij} = \frac{3R_iR_j}{R^5} - \frac{\delta_{ij}}{R^3}, \tag{2.144}$$

with $\mathbf{R}$ the vector between the two dipoles. But similar to equation (2.143)

$$\boldsymbol{\mu}_2 = P\left(\mathbf{E}_{\text{ext}} + A\boldsymbol{\mu}_1\right). \tag{2.145}$$

Inserting equation (2.145) into equation (2.143)

$$\begin{aligned} \boldsymbol{\mu}_1 &= P\left(\mathbf{E}_{\text{ext}} + A.P\left(\mathbf{E}_{\text{ext}} + A.P\boldsymbol{\mu}_1\right)\right) && (2.146) \\ \Longleftrightarrow \left(I - PAPA\right)\boldsymbol{\mu}_1 &= \left(P + PAP\right)\mathbf{E}_{\text{ext}} && (2.147) \\ \Longleftrightarrow \boldsymbol{\mu}_1 &= \left(I - PAPA\right)^{-1}\left(P + PAP\right)\mathbf{E}_{\text{ext}} && (2.148) \end{aligned}$$

where I is the identity matrix. The total polarizability of the system is therefore

$$P_{\text{tot}} = \left(I - PAPA\right)^{-1}\left(P + PAP\right) \tag{2.149}$$

Then for this basic model, the electric field enhancement in the center of the system is given by

$$\mathbf{E}_{\text{ind}} = 8.\left(A\boldsymbol{\mu}_1 + A\boldsymbol{\mu}_2\right) \tag{2.150}$$

where $\boldsymbol{\mu}_1$ and $\boldsymbol{\mu}_2$ are respectively given by equation (2.148) and (2.145).
The polarizability and electric field enhancement provided by this simple model are shown in figure 2.4.1 with an external field along the $y-$axis and the two objects separated by a distance d along the $y - axis$. One can notice that two modes are present, one mode is shifting to higher energies when the distance decrease. This mode is therefore a non-stable solution caused by the P_{xx} and P_{zz} matrix elements (figure 2.4.1b and 2.4.1d). The second mode is caused by the P_{yy} matrix element as shown in figure 2.4.1c. This mode is going to lower energies when the distance decrease and correspond to a stable solution.

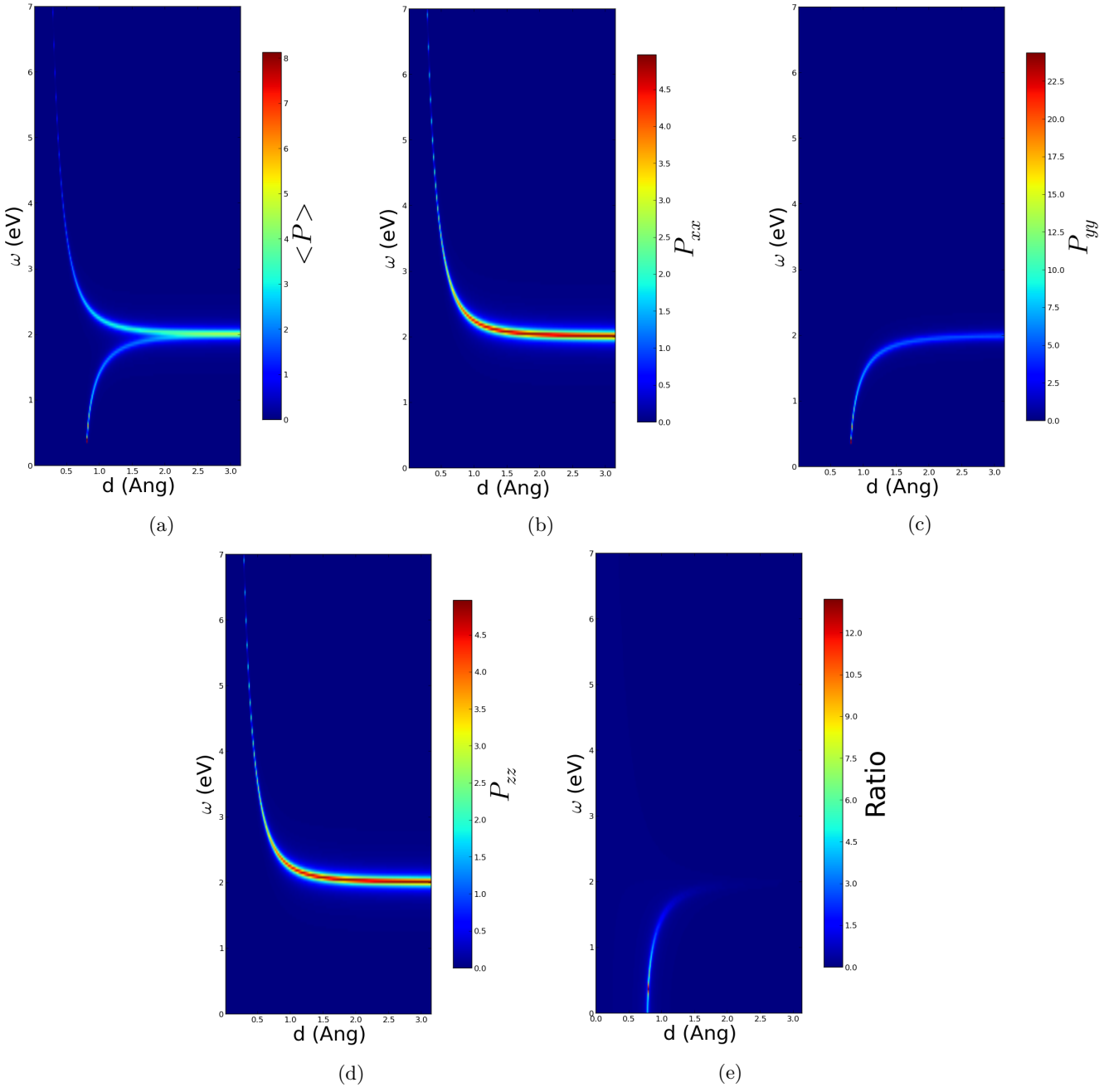

(a) (b) (c) (d) (e)

Figure 2.4.1: (a) average, (b) matrix element xx, (c) matrix element yy, (d) matrix element zz of the imaginary part of the polarizability and (d) electric field enhancement in the center of the dipoles, for two interacting dipoles and an external field oriented in the z direction, when the distance between the dipole increase.

Chapter 3

Results: Na cluster dimers

In this section, we analyze the optical response of four sodium cluster dimers (Na_2, Na_8, Na_{20} and Na_{150}). The calculations are done using a new implementation of TDDFT in linear regime developed in the framework of the Orgavolt project [33]. During this master thesis, an extension of this code was developed in order to calculate the spatial distribution of the induced electric field. This code is interfaced with SIESTA [34] an efficient density functional theory implementation. In all the calculations, a *double zeta polarized* (DZP) basis set has been used with standard pseudo-potentials of Troullier-Martins type [35]. The used *exchange-correlation* functional is the *local density approximation* (LDA) Ceperley-Alder functional[36]. In the following, the calculations performed with this TDDFT code are presented. The calculations consist on the determination of the polarizability and the field enhancement for cavities formed by two Na clusters of different sizes.

For the four dimers, only the $3s$ conduction electrons are explicitly included in the calculation by using standard pseudo-potentials of Troullier-Martins type described in the Appendix B. While in our calculations the variation of all matrix elements of the polarizability with distance is considered, for the calculation of the induced density and induced field distribution we focus on the case where the external field is directed along the $y-$axis, i.e. the vector that separates the two clusters in the dimer. For the Na_2 dimers, the default broadening constant was chosen ($\varepsilon = 0.0083$eV), while for the three larger dimers the calculations are presented with a broadening constant $\varepsilon = 0.1$ eV. The program calculates the value of the electrical field in each point of the space, and the spatial resolution considered for the following calculation is $dx = dy = dz = 0.3$ Bohr, which is a suitable value as shown in Appendix C.
First of all, calculations for Na_2 dimer with relaxed geometries were performed in order to check the consistency of our calculations with the simple model presented in section 2.4. Then, the optical properties of three sodium dimers of different sizes were analyzed. For the Na_8 and Na_{20} clusters, the polarizability and field enhancement were analyzed with relaxed and non-relaxed geometries, taking the geometries from [37] for the Na_2 and Na_8 dimers and from [38] for the Na_{20} and Na_{150} dimers. Since these calculations provide similar results for both geometries (Figure 3.2.4), only the results for the non-relaxed molecules are presented in section 3.2 and 3.3. For the Na_{150} analyzed in section 3.4, the position of the atoms were relaxed for the one cluster case, then the relaxed geometry was used to build the cavity.

3.1 Na_2 Cluster

In order to check the consistency of our program with the simple model presented in section 2.4, we analyze the optical properties of a Na_2 dimer that can be assimilate to two interacting dipoles as in our simple model. We study three different geometries, in the first one the molecules are aligned along $x-$axis, in the second one along $y-$axis and in the last geometry the molecules are aligned along $z-$axis, as shown in the plane $z = 0$ in Figure 3.1.1.

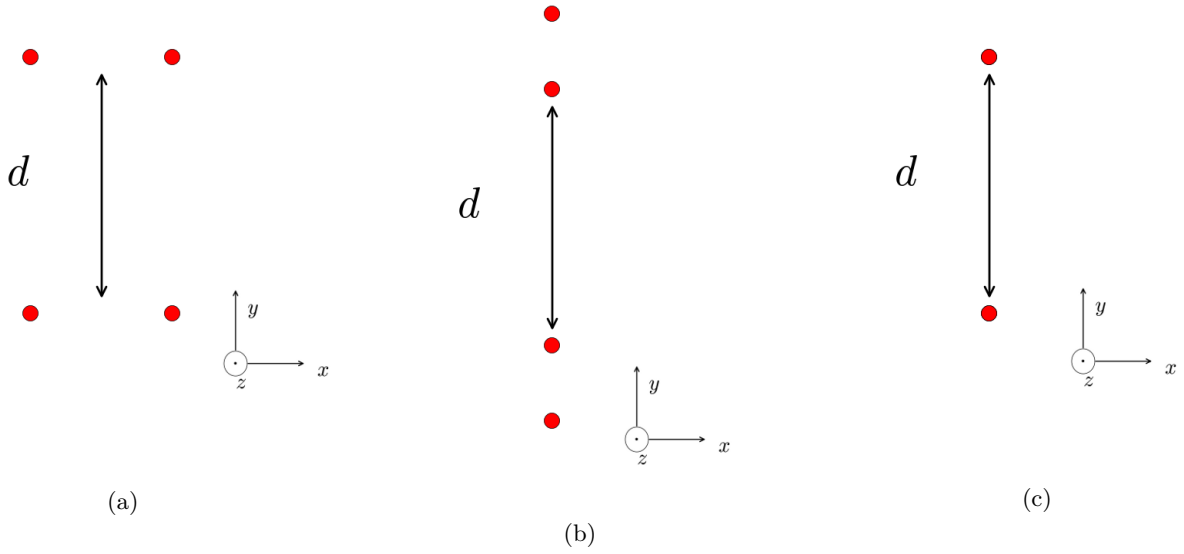

Figure 3.1.1: Geometries of the Na_2 dimers in the plane $z = 0$, when the molecular axis is (a) along the $x-$axis, (b) along the $y-$axis, and (c) along the $z-$axis (for this geometry, the projection of the atoms in the plane $z = 0$ give only two points). The distance d between the molecules is changed from 3 to 12 Å. The distance between the atoms in a molecule is 2.97 Å.

The Na_2 is a good check for our program because of its simple geometry. The density distribution is very similar to that of a dipole (Figure 3.1.2) as in our simple model presented in section 2.4. The broadening constant of the following calculation was set to its default value $\varepsilon = \frac{\Delta\omega}{N_\omega} = 0.0083$ eV where $\Delta\omega = 5.0$ eV is the frequency window, and $N_\omega = 600$ is the number of frequency. The default value was chosen in order to have a better visualization of the frequency shift. Figures 3.1.3, 3.1.4, 3.1.5 and 3.1.6 show the evolution of the polarizability as function of the distance d between the molecules in our frequency window $\Delta\omega$, and should be compared with Figure 2.4.1a, 2.4.1b, 2.4.1c and 2.4.1d; respectively. For large separation between the Na_2 molecules we observed two modes in the average polarizability. The high energy mode corresponds to the polarization of the molecule perpendicular to the molecular axis, whereas the low energy mode corresponds to the polarization along the molecular axis. From a qualitative point of view, the results in Figures 3.1.3, 3.1.4, 3.1.5 and 3.1.6 are similar to those obtained with our simple model. When the external field is perpendicular to the vector joining the molecular centers (along the $y-$axis here as in Figures 3.1.4 and 3.1.6), the excited modes tend to shift to higher frequencies as the distance decreases. When the external field is directed along the $y-$axis (see Figure 3.1.5) we observe a more complex behavior. However, similar to the simple model, the frequencies of the excited modes tend to decrease with the intermolecular distance.

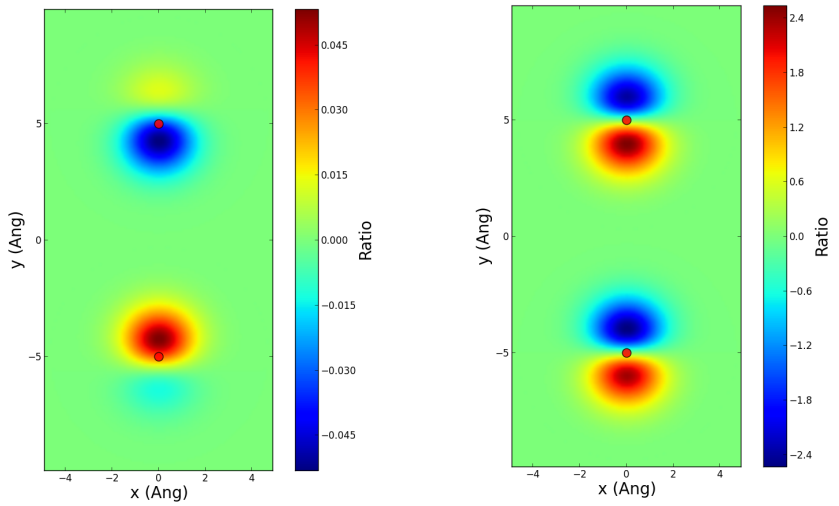

(a) (b)

Figure 3.1.2: Electronic density distribution when the molecules are oriented along the $z-$axis and separated by a distance of 10.0Å at the energy of 3.43 eV, (a) real part, (b) imaginary part,

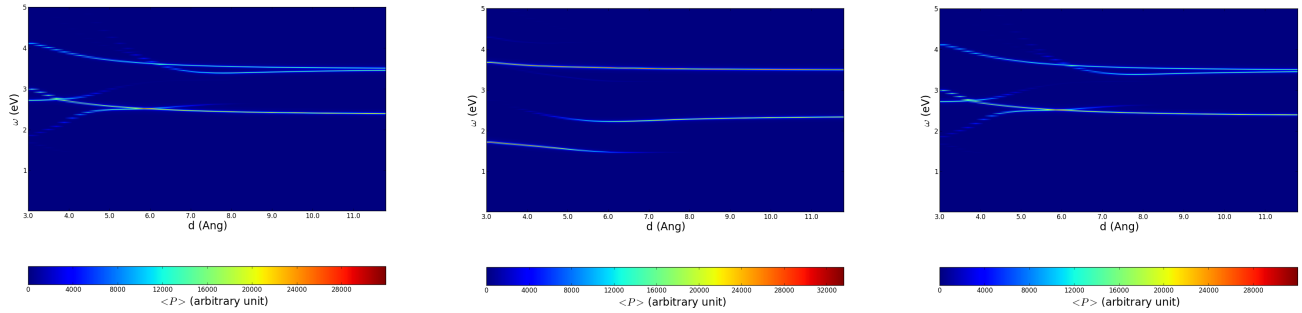

(a) (b) (c)

Figure 3.1.3: Average of the imaginary part of the polarizability, when the axes of the molecules are (a) along the $x-$axis, (b) along the $y-$axis, and (c) along the $z-$axis.

As expected from the symmetry of the system, the average polarizability and the electric field enhancement are exactly the same when the molecules are oriented along the $x-$axis and along the $z-$axis, as shown in Figure 3.1.3 and 3.1.7. Figure 3.1.4 and 3.1.6 show that the matrix elements P_{xx} and P_{zz} are inverted as expected.
For the three geometries the P_{xx} and P_{zz} matrix elements are continuous, while the P_{yy} matrix element shows some discontinuities (one discontinuity when the molecules are separated by 5.5 Å for the second geometry (Figure 3.1.5b) and two discontinuities when the molecules are separated by 4.5 Å and by 7.0 Å for the first and third geometries (Figure 3.1.5a and 3.1.5c)).

This small test give us a some confidence in the calculations of our program since the results can be understood with a simple dipole model. The differences can be justified by the limitations of the model, in particular electron tunneling between molecules and pure chemistry (formation of bonds) are not taken into account by the dipole model but are present in the case of the Na_2 molecule.

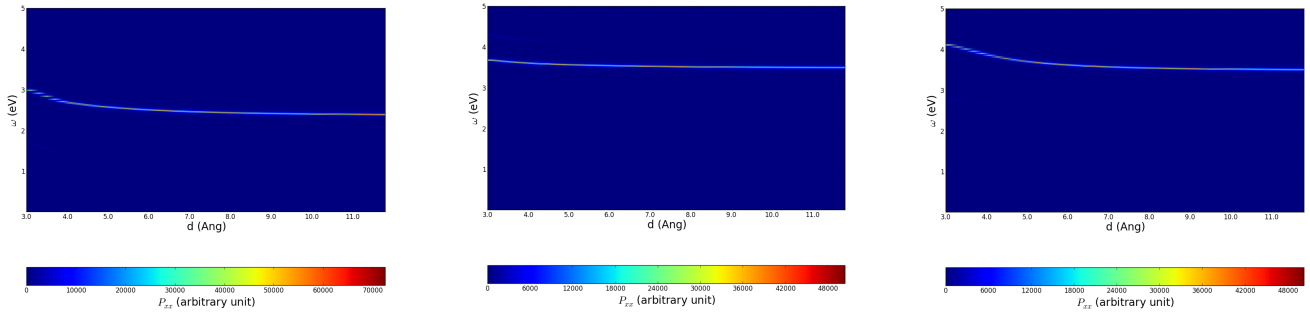

(a) (b) (c)

Figure 3.1.4: Matrix element xx of the imaginary part of the polarizability, when the axes of the molecules are (a) along the $x-$axis, (b) along the $y-$axis, and (c) along the $z-$axis.

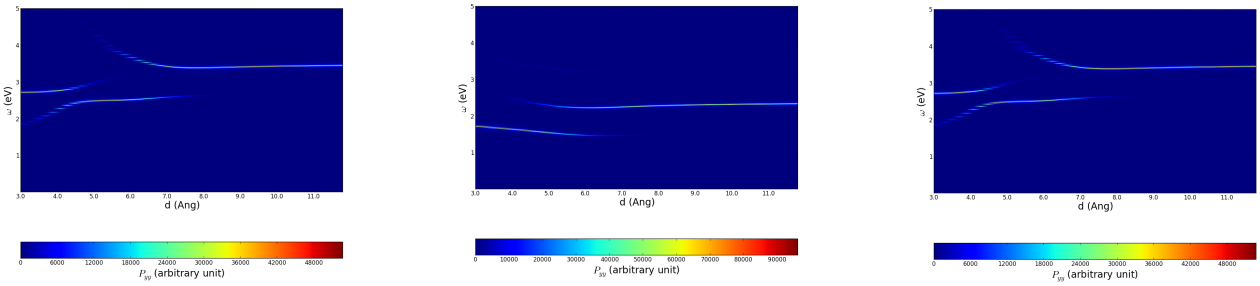

(a) (b) (c)

Figure 3.1.5: Matrix element yy of the imaginary part of the polarizability, when the molecular axes are (a) along the $x-$axis, (b) along the $y-$axis, and (c) along the $z-$axis.

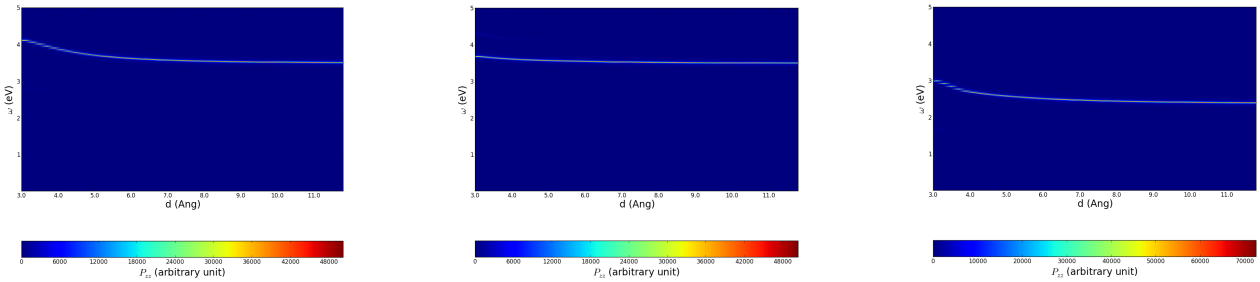

(a) (b) (c)

Figure 3.1.6: Matrix element zz of the imaginary part of the polarizability, when the molecular axes are (a) along the $x-$axis, (b) along the $y-$axis, and (c) along the $z-$axis.

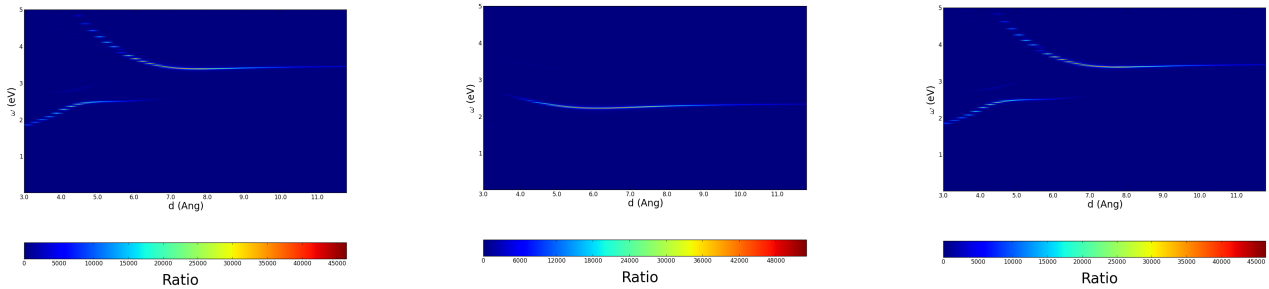

(a) (b) (c)

Figure 3.1.7: Electric field enhancement in the center of the cavity, when the external electric field is oriented in the $y-$direction and the molecular axes are (a) along the $x-$axis, (b) along the $y-$axis, and (c) along the $z-$axis.

3.2 Na_8 Cluster

Then ab-initio calculations for the Na_8 cluster were performed. The geometry of the clusters was taken from Ref.[37] and is depicted in Figure 3.2.1.

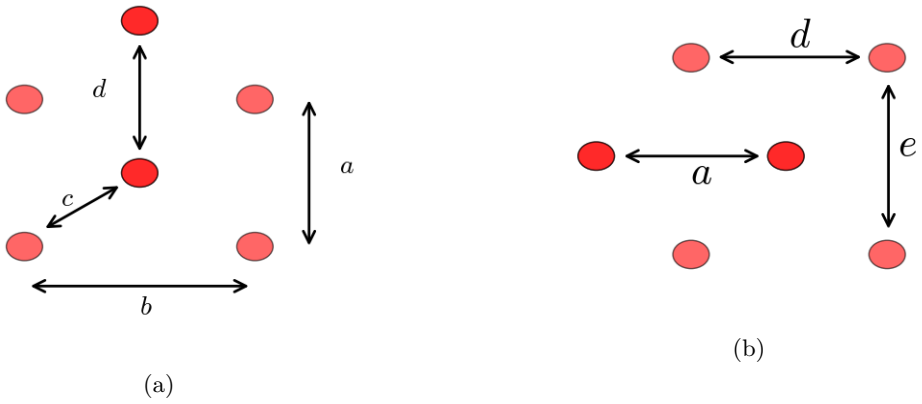

Figure 3.2.1: Geometry of the Na_8 cluster, (a) in the plane $z = 0$, (b) in the plane $x = 0$. The distances between the atoms are $a = 3.122$Å, $b = 3.810$Å, $c = 3.227$Å, $d = 3.228$Å and $e = 4.170$Å.

Then, from the one cluster geometry, the cavity can be built by putting face to face two clusters along the $y-$axis as shown in Figure 3.2.2. The distance d is the distance between the edge atoms of the clusters.

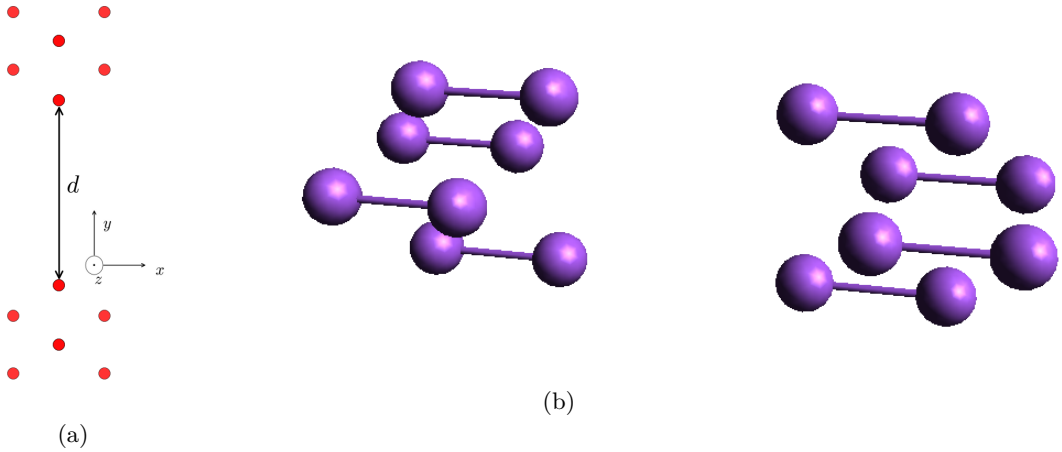

Figure 3.2.2: Geometry of the Na_8 cavity, (a) in the plane $z = 0$, (b) in 3 dimensions. The distance between the 2 clusters is the variable d.

3.2.1 Polarizability

The first interesting quantity in this work is the imaginary part of the polarizability tensor because it is connected to the absorption cross-section given by the equation (2.44) and it is determined by the electron transitions (section 2.1). The one cluster case and the two clusters cases have been studied, with relaxed and non-relaxed geometries. In Figure 3.2.3, the polarizability of the relaxed geometry (red curves) and of the non-relaxed geometry (blue-dotted line) are compared for one cluster. The two polarizabilities have a similar shape, therefore, in the following only the non-relaxed geometry data will be presented. However, calculations were also done with relaxed geometries, and always present similar shapes than the non-relaxed ones. The optical properties of the isolated Na_8 cluster have been studied by *Tsolakidis et al.* [39]. Our results in Figure 3.2.4b are consistent with those of these authors (Figure 3.2.4a).

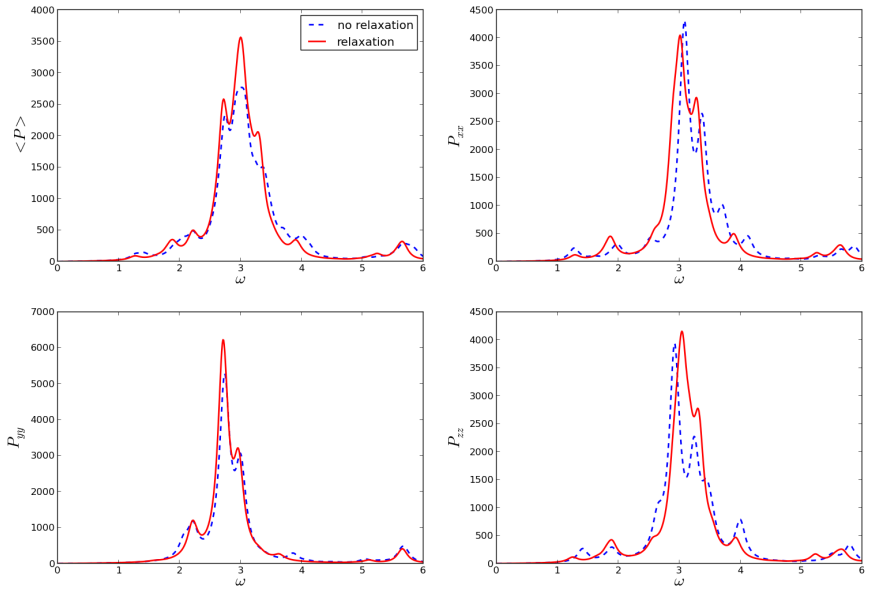

Figure 3.2.3: Imaginary part of the linear polarizability for the Na_8 cluster vs energy. Red curves are the polarizabilities computed when the positions of the atoms are relaxed, while dotted blue curves correspond to the calculation without relaxation. The left top panel is the average polarizability ($< P >= \frac{1}{3}\mathrm{Tr}\{P_{ij}(\omega)\}$), the right top panel is the xx matrix element of the polarizability, the left down panel is the yy matrix element and the right down panel is the zz matrix element.

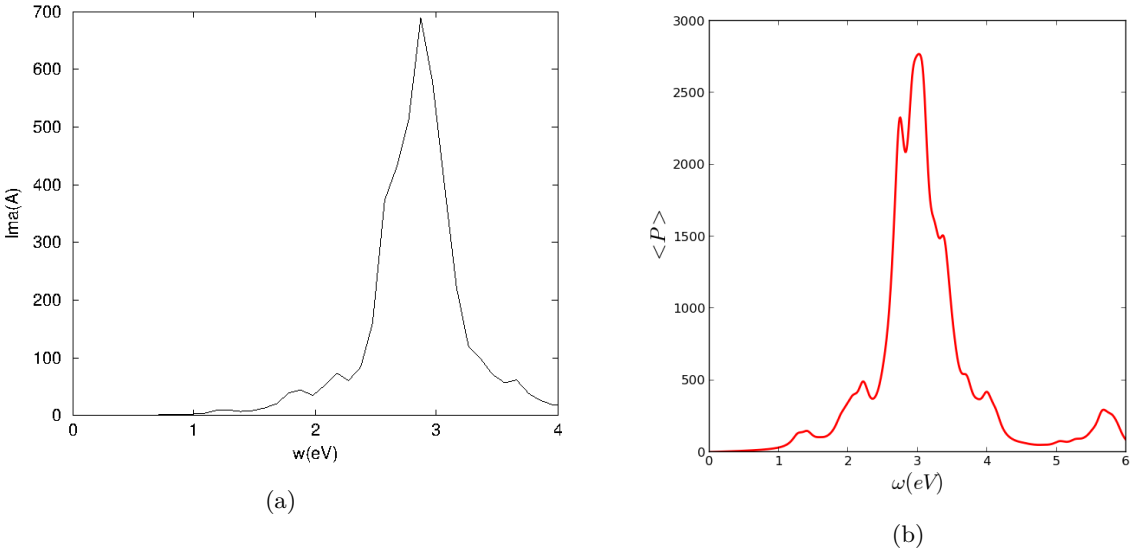

(a) (b)

Figure 3.2.4: Imaginary part of the average linear polarizability of Na_8 vs energy (a) from the literature[39], (b) our calculation.

The plots in Figures 3.2.4a and 3.2.4b have a similar shape with a main peak around 3 eV. The calculations were done with a broadening constant $\varepsilon = 0.1$ eV. The good agreement between our calculations of the polarizability of one Na_8 cluster with previous results give us additional confidence in our new TDDFT implementation.

We will now analyze the polarizability of two Na_8 clusters forming a nanocavity. Figure 3.2.5 and Figure 3.2.6 show the evolution of the imaginary part of the polarizability as a function of the distance for the frequency range $\Delta\omega = [0; 6]$ eV. Figure 3.2.5a is a contour plot of the average polarizability and Figure 3.2.5c is the contour plot of the P_{yy} matrix element. One can observe that at small distances ($1.0 < d < 5$ Å) the average polarizability shows two peaks; one at small frequency (~ 2.1 eV) with a higher intensity and another one at higher frequency (~ 3.8 eV). Around a cavity size of 5 Å, the peak at low frequency goes to zero while a new one appears at a slightly higher frequency (~ 2.74 eV). This shifts are particularly visible in the contour plot 3.2.5c and in Figure 3.2.6c, which shows the details of the P_{yy} matrix element for different cavity sizes. Moreover, one can notice that this polarizability change is correlated with the change in the density distribution shown in Figures 3.2.7 and 3.2.8. The density distributions for small and large cavity sizes are quite different, and this change happens for a cavity size of around 5 Å. This shift was also visible in our small model (Figure 2.4.1) presented in section 2.4 and is therefore characteristic of two interacting dipoles. When the distance between the clusters decreases one can also notice a blue shift of the high energy peak (from 3.0 eV to 3.8 eV) that is caused by the P_{zz} matrix element as shown in Figure 3.2.6d. This blue shift was also present in our small model. As it is well known the polarizability peak corresponds to a dipole *localized surface plasmon* or *Mie resonance* and, under a quantum treatment, its width is due to Landau fragmentation plus non electronic damping processes [40, 41]. It can be noticed that the polarizability along the $y-$axis is stronger compare to the one along the $x-$axis and $z-$axis. This is caused by the geometry of the cluster, shown in Figure 3.2.1, the cluster shows a larger number of Na-Na bonds along the $y-$axis than along the two other axis.

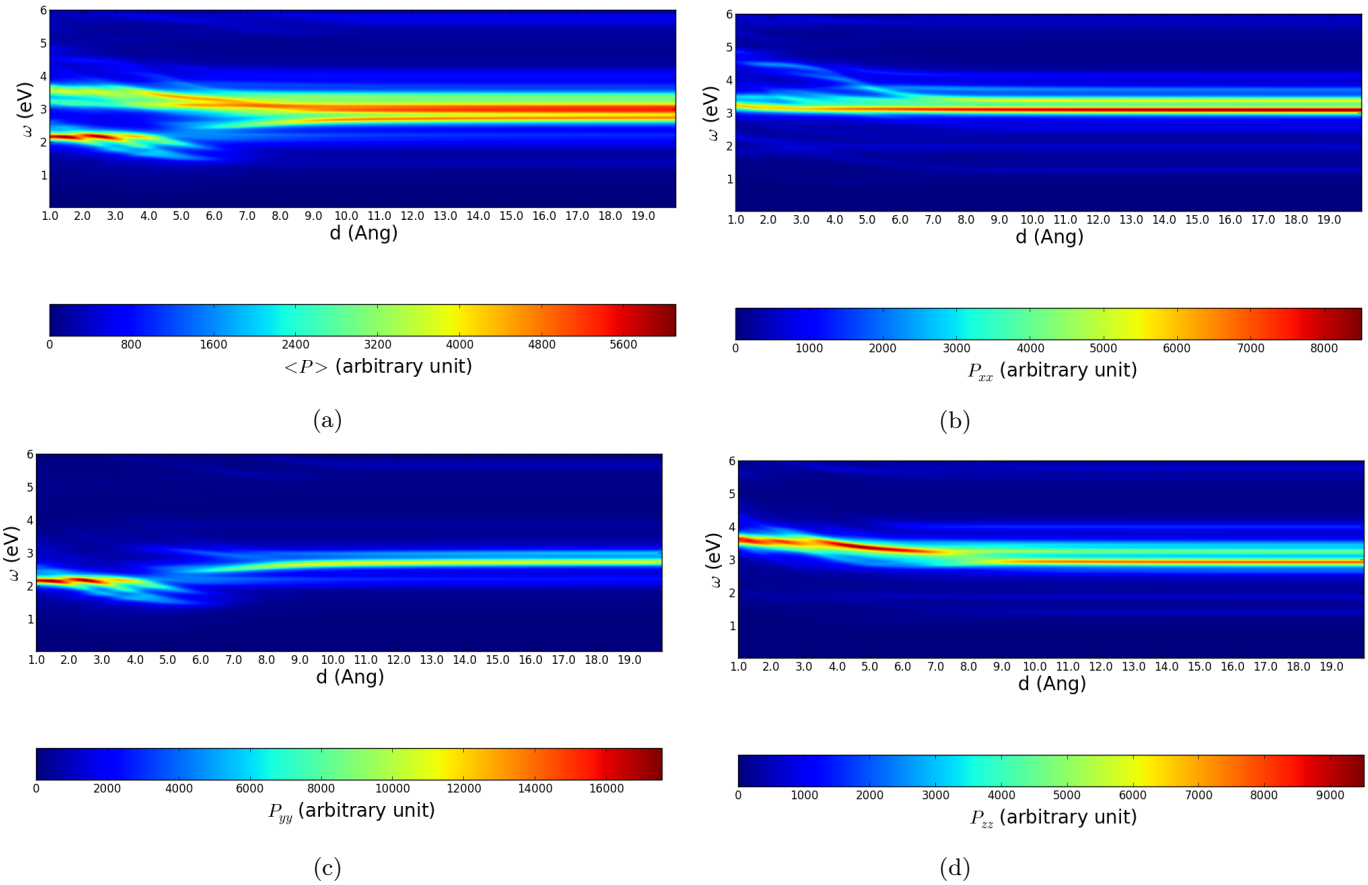

Figure 3.2.5: Contour plots of (a) the average (b) the *xx* matrix element, (c) the *yy* matrix element and, (d) the *zz* matrix element, of the polarizability for the two Na_8 clusters whose the geometry were kept fixed (unrelaxed) vs the distance *d* between the clusters.

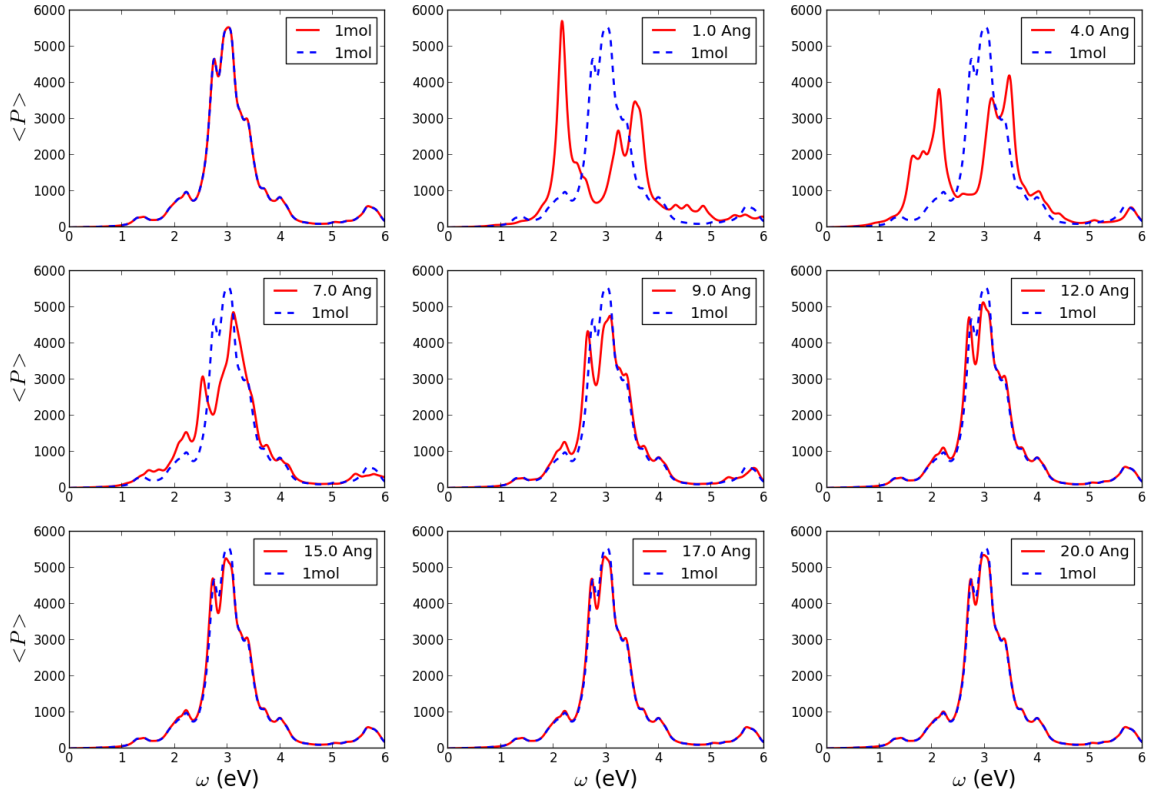

(a)

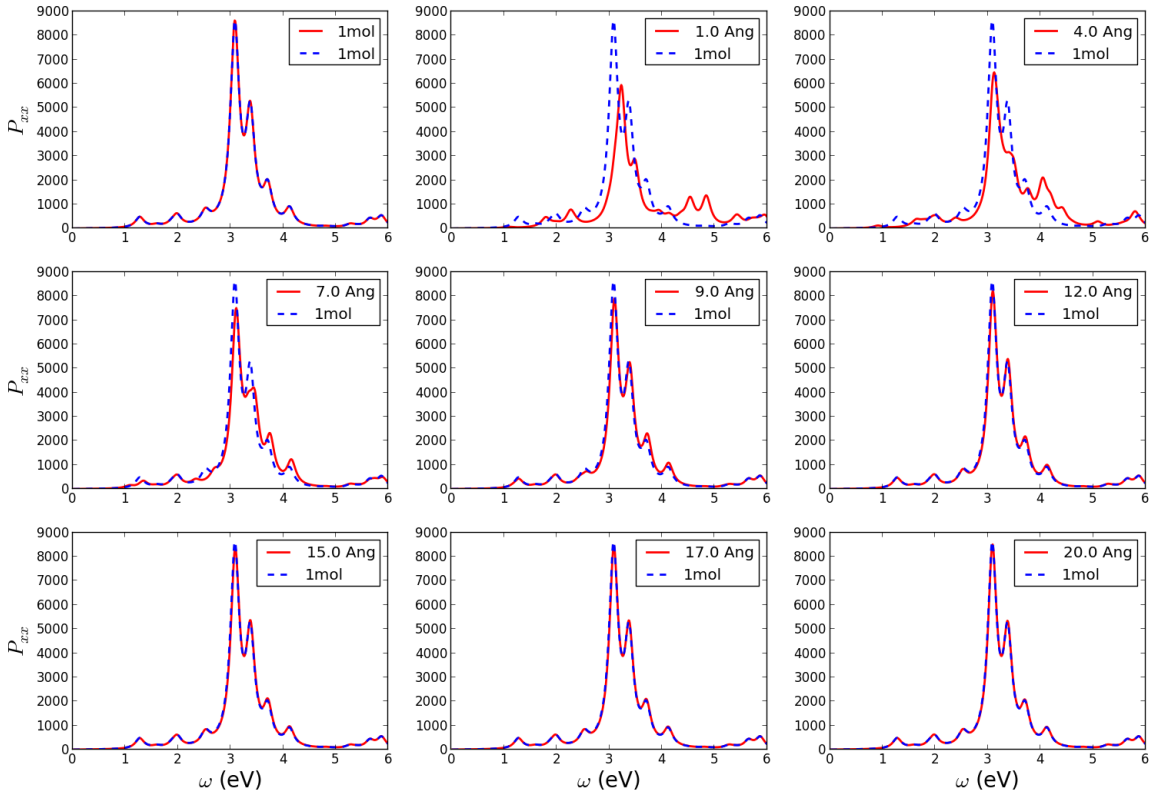

(b)

Figure 3.2.6

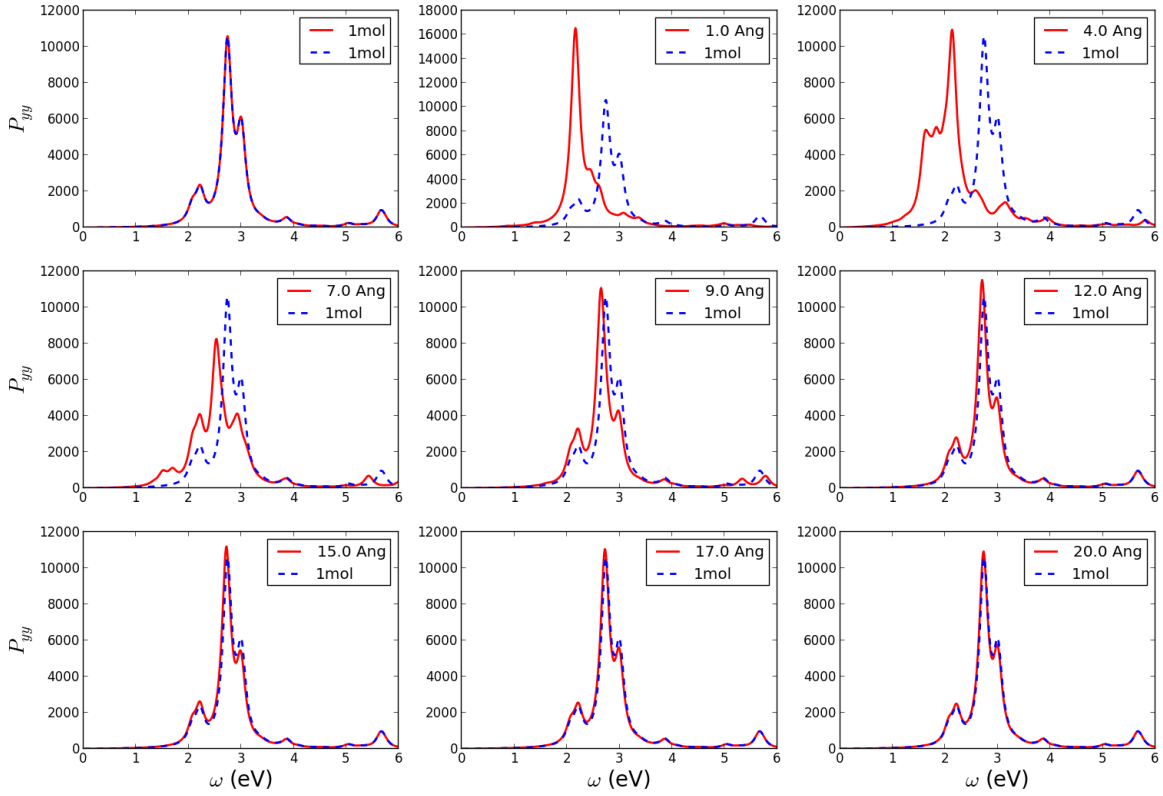

(c)

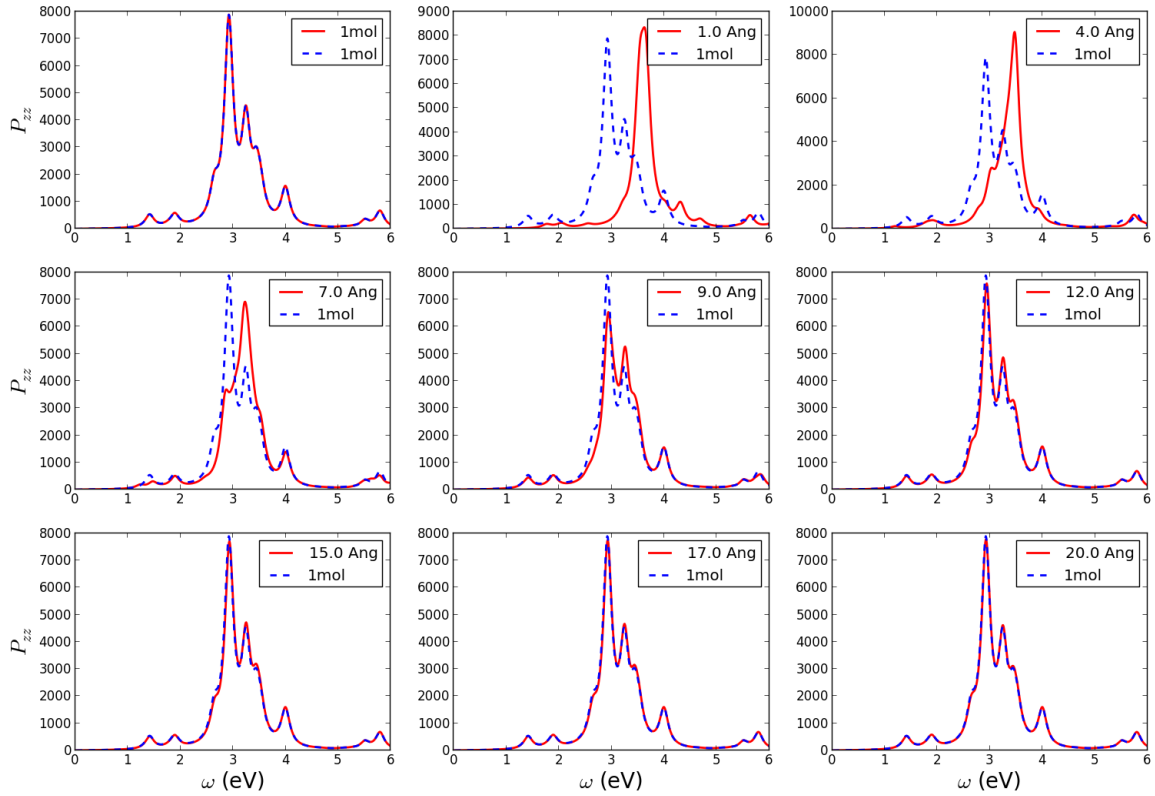

(d)

Figure 3.2.6: Imaginary part of the linear polarizability of two Na_8 clusters vs energy for several distances between the clusters. The blue dotted line represents the polarizability of one cluster multiply by two. (a) Average polarizability, (b) P_{xx} matrix element, (c) P_{yy} matrix element, (d) P_{zz} matrix element.

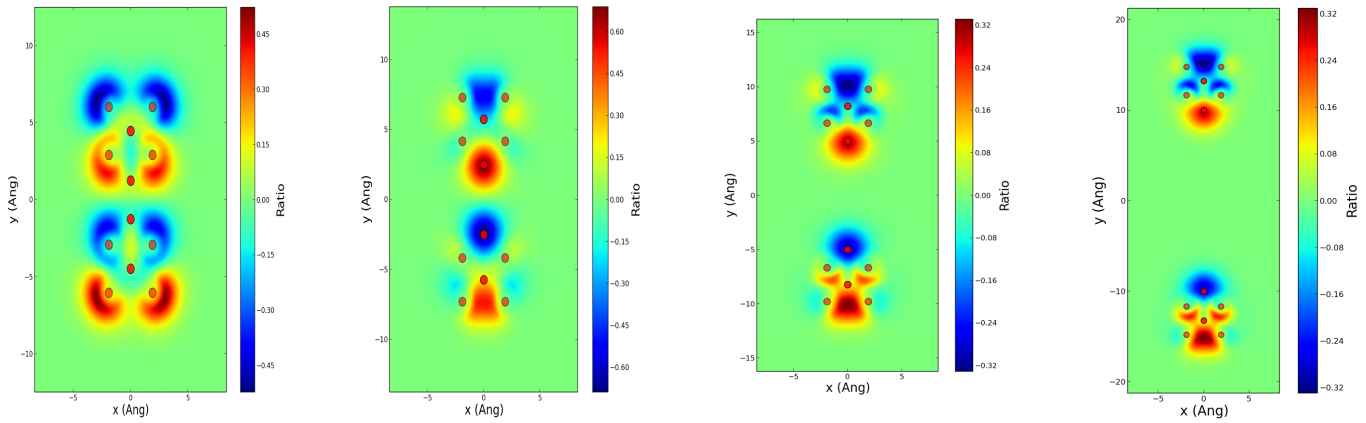

(a) (b) (c) (d)

Figure 3.2.7: Real part of the induced density for different cavity sizes at the energy of the maximum polarizability peak, in the plane $z = 0$ (a) cavity of 2.5Å at 2.13 eV, (b) cavity of 5.0Å at 2.3 eV, (c) cavity of 10.0Å at 2.67 eV and (d) cavity of 20.0Å at 2.72 eV.

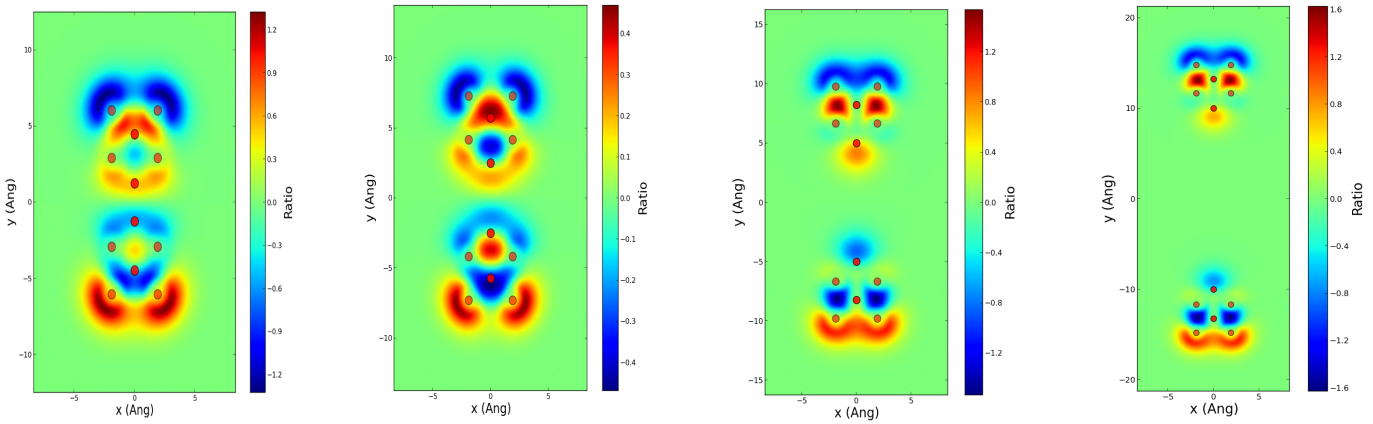

(a) (b) (c) (d)

Figure 3.2.8: Imaginary part of the induced density for different cavity sizes at the energy of the maximum polarizability peak, in the plane $z = 0$ (a) cavity of 2.5Å at 2.13 eV, (b) cavity of 5.0Å at 2.3 eV, (c) cavity of 10.0Å at 2.67 eV and (d) cavity of 20.0Å at 2.72 eV.

For large distances, the induced density of two Na_8 clusters has a similar shape to that of a single cluster. We can compare these two cases by comparing Figures 3.2.7d and 3.2.9a for the real part, and Figures 3.2.8d and 3.2.9b for the imaginary part. Therefore, at large distances two distinguishable dipoles, corresponding to those of the individual clusters, are present. For short distances, the density distribution changes and cannot be assigned anymore to a superposition of those of two individual clusters (Figures 3.2.7a and 3.2.8a).

3.2.2 Electric Field Enhancement

After checking in the literature that our polarizability has a correct shape compared to previous calculations in the literature, and that the evolution of this polarizability in the dimer case is reasonable compared to the one cluster case, we compute the electrical field enhancement distribution as defined in section 2.3.3.

At this point, we are interested in the intensity of the induced electrical field $I_{ind} = |\mathbf{E}_{ind}|^2$. In the next graphics, the ratio between this induced intensity and the intensity of the external electric field

$I_{ext} = |\mathbf{E}_{ext}|^2$ is represented: $Ratio = \frac{I_{ind}}{I_{ext}}$. In these calculations the external electric field is always directed along the $y-$direction.

First of all, we present the electric field distribution for the one cluster case

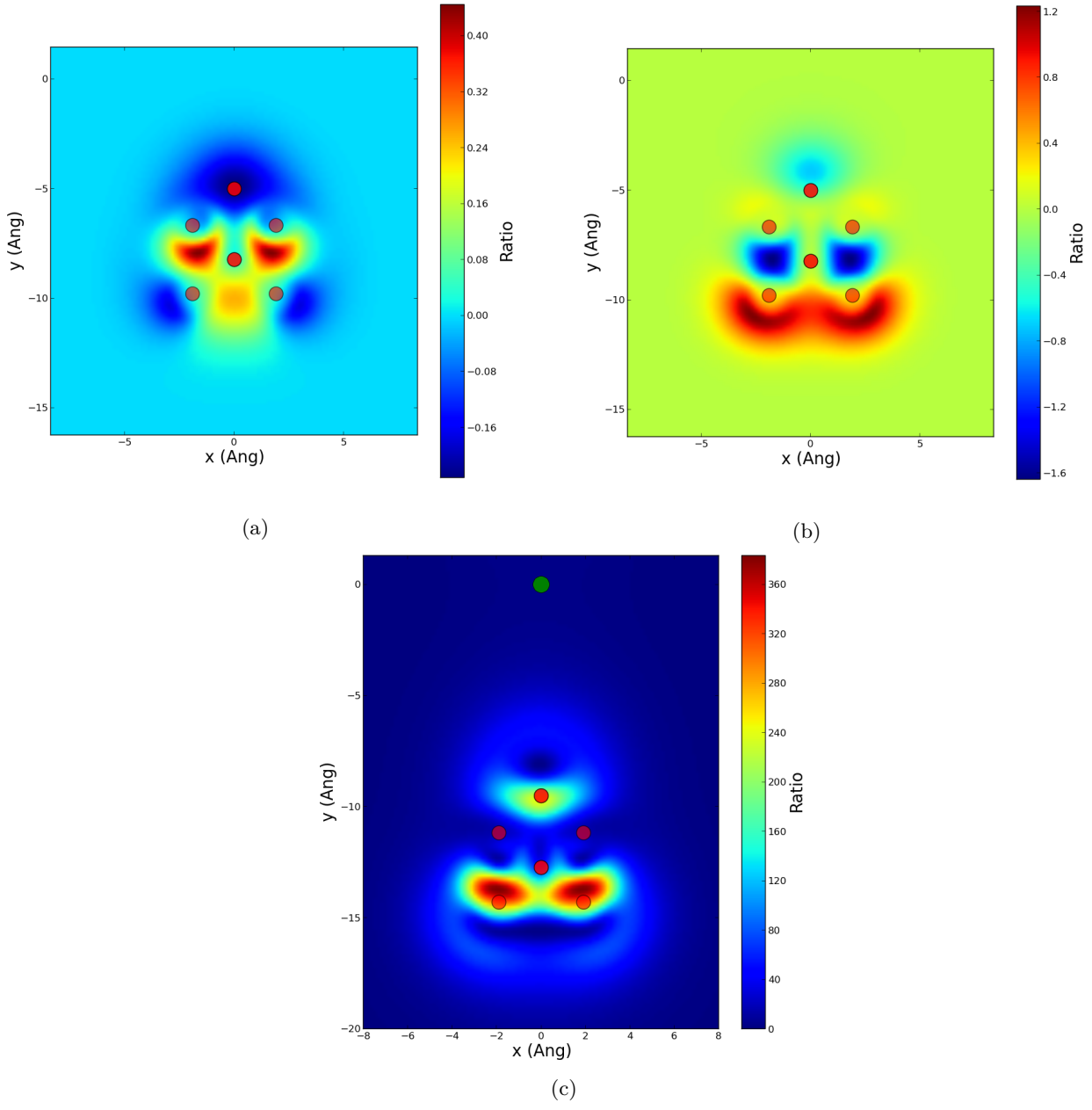

(a) (b)

(c)

Figure 3.2.9: (a) Real part of the induced density distribution, (b) imaginary part of the induced density distribution and (c) electric field enhancement distribution (the green dot represent the point $(0, 0, 0)$), for one Na_8 cluster in the plane $z = 0$, at the energy of 2.74 eV (energy at which P_{yy} and the intensity are maximal as shown in Figure 3.2.3 left down panel and Figure 3.2.4b).

Figure 3.2.9 shows the density and the electric field enhancement distribution for one Na_8 cluster. Figure 3.2.10 shows the electric field enhancement distribution for two Na_8 clusters and the comparison of the field enhancement in Figure 3.2.10d, for one cluster (blue dotted line) and for two clusters (red curve). The field enhancements shown in Figure 3.2.10c were calculated at 9.5 Å from the cluster edges (Green dot plotted in Figures 3.2.9c and 3.2.10c).
The plots shown in Figure 3.2.9 were calculated at the energy of 2.74 eV. As shown in Figure 3.2.10c, this

is the value of the energy at which the field enhancement is maximal for the chosen distance. One can see in Figure 3.2.4b that the polarizability along $-y$ for one cluster is also maximal at this energy. We focus now on the field enhancement distribution as shown in Figure 3.2.10. In particular the study of the evolution of the intensity in the center of the two clusters as function of the cavity size is the objective of the present master thesis work. For a distance of 5 Å, Figure 3.2.10a shows clearly that the intensity peak is at the center of the cavity, but at this distance, the intensity of the electrical field is quite low. When the distance increases, the maximal intensity peak is inside the clusters. Moreover, the intensity in the center is still high (Figure 3.2.10b), even higher than for shorter distances.

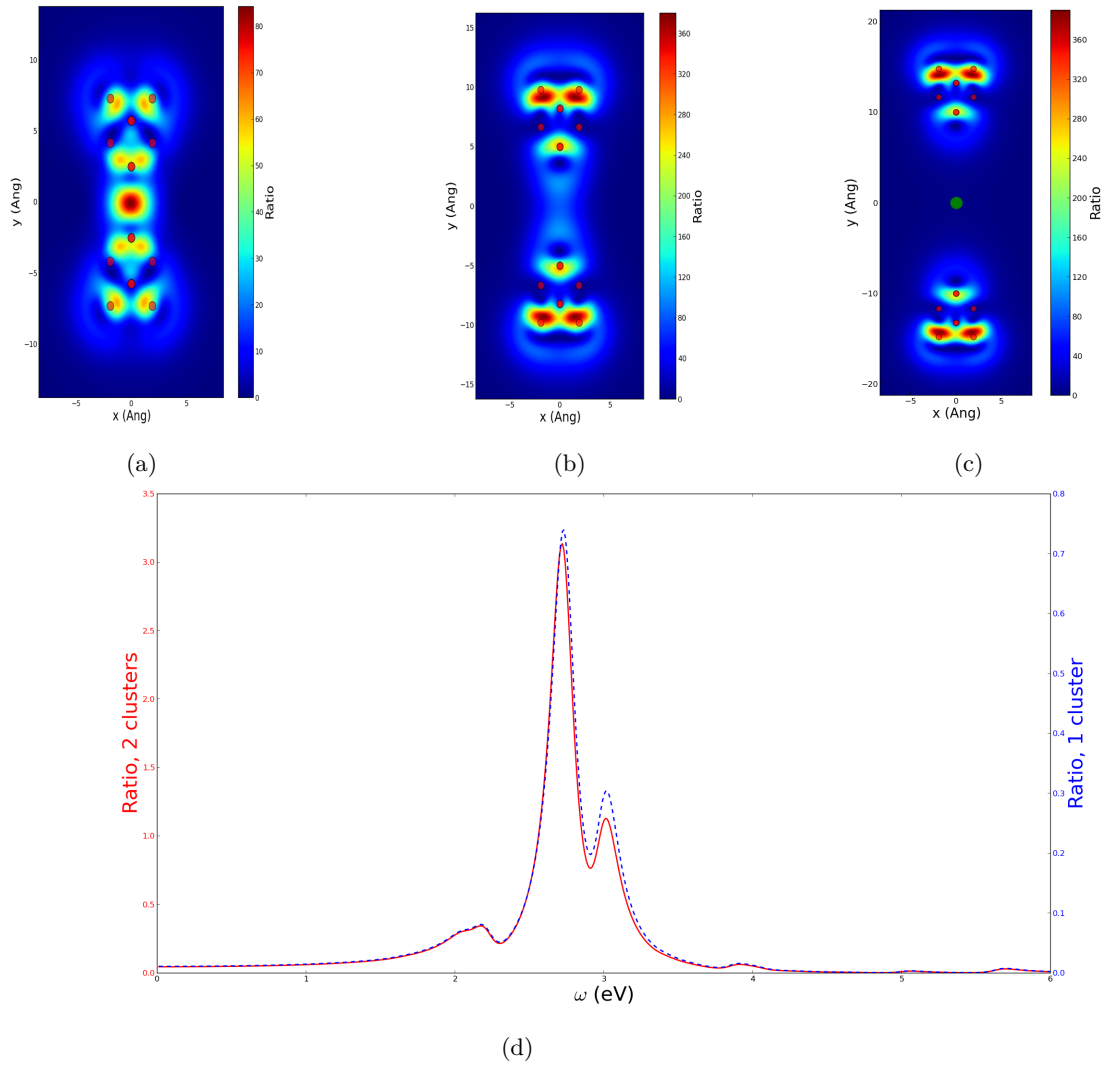

Figure 3.2.10: Intensity of the electric field enhancement for different cavity sizes at the energy of the maximum intensity of the P_{yy} polarizability matrix element, in the plane $z = 0$ (a) cavity of 5.0Å at 2.3 eV, (b) cavity of 10.0Å at 2.67 eV, (c) cavity of 20.0Å at 2.72 eV, the green point is the point where we perform the calculation for the red curve shown in Figure 3.2.10d and (d) comparison of the induced field intensity for one cluster (blue dotted line) and two clusters (red line), the intensity is measured at a distance of 9.5Å from the cluster edges for the frequency window $\Delta\omega = [0; 7]$. The external field is directed along the axis of the dimer, i.e. the $y-$axis.

Figure 3.2.10 shows the intensity distribution for three different cavity sizes (5.0Å, 10.0Å and 20.0Å). Comparing Figures 3.2.10c and 3.2.9c, it is clear that for large distances between the clusters the distribution of the induced field is very similar to that for an isolated cluster. This is shown in Figure 3.2.10d, where the frequency dependence of the field enhancement for two clusters (red curve) and for one cluster (dotted blue line) are compared. The electric field is calculated at a distance of 9.5Å from the edge of the

cluster. The two curves have a similar shape which shows that for large distances, the clusters act like two isolated clusters, only the value of the enhancement ratio is different, for two clusters. Even for so large distances, there is still a small enhancement (almost 4). However, for the one cluster the induced field is smaller than one at such large distances (Figure 3.2.10d blue dotted lines). The average ratio between the induced field for the two clusters and the one cluster is $R = 4.043$. The density distribution of two clusters is also similar to the density distribution of one cluster for large distance as show by comparing of Figure 3.2.7d and Figure 3.2.9a as well as Figure 3.2.8d compared with Figure 3.2.9b

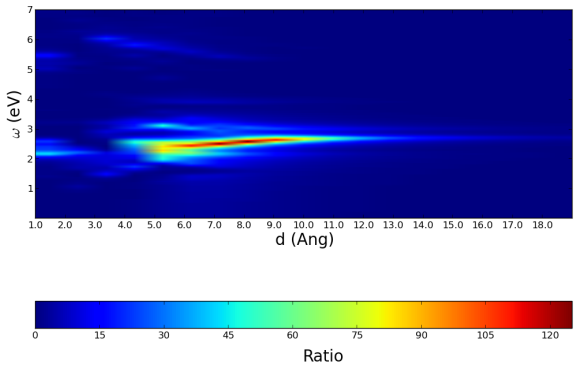

(a)

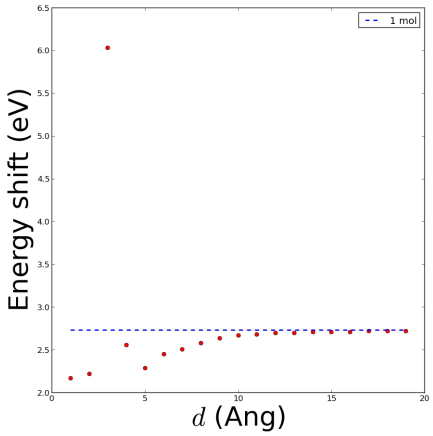

(b)

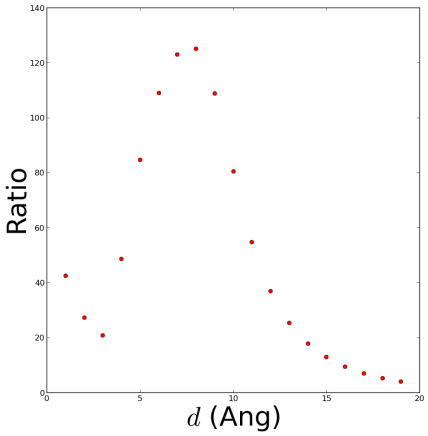

(c)

Figure 3.2.11: (a) Intensity of the induced field as a function of the energy calculated in the center of the cavity for several cavity sizes. (b) Evolution of the energy of the maximal intensity peak (the dotted blue line is the energy of the maximal intensity peak for one cluster), and (c) evolution of the maximal intensity (the energy for a given distance is shown in figure 3.2.11b), when the size of the cavity formed by the two Na_8 clusters increases. The external field goes along the $y-$axis, i.e. the axis of the clusters.

Figure 3.2.11a shows the evolution of the intensity at the center of the cavity as function of the cavity size for a frequency range between 0 and 7 eV. Figure 3.2.11b shows a clear red shift of the intensity peak when the distance between the two cluster decreases. The energy of this peak converges to the value for one cluster (blue dotted line at 2.74 eV) for large cavity sizes. And Figure 3.2.11c shows the value of the induced field at the energy shown in Figure 3.2.11b. At short distances (smaller than 5Å), the energy of the maximum peak is quite irregular with some low value around 2.2 eV and two larger values at $d = 3$Å, $\omega \sim 6.0$ eV and at $d = 4.0$Å, $\omega \sim 2.6$ eV. From $d = 5$ Å, the energy shift has a regular evolution until 12 Å, where the energy reaches the value for one cluster. The irregular shape at short distances can be explained from the fact that for this distance range, the electrons of the two clusters start to overlap. This also explains that the maximum intensity for short distances is quite low as shown in Figure 3.2.11c, then it is increasing until it reaches its maximal value for $d = 9$ Å. For larger distances, the maximal

intensity is decreasing as $\frac{1}{d^3}$ because the electric field of a dipole decay as the inverse of the cube of the distance as it is explained in section 2.3.4.

3.3 Na_{20} Clusters

Similar calculations have been done for the Na_{20} cluster. The geometry of this cluster can be found in Ref.[38] and is given in Figure 3.3.1. For the Na_{20}, two different geometries have been analyzed. The second one corresponds to a rotation of 135° around the $z-$axis compared to the first geometry. In the two cases, the dimer has a mirror plane passing through the center of the gap. Both geometries differ in the side of the cluster in closer proximity to the neighboring cluster.

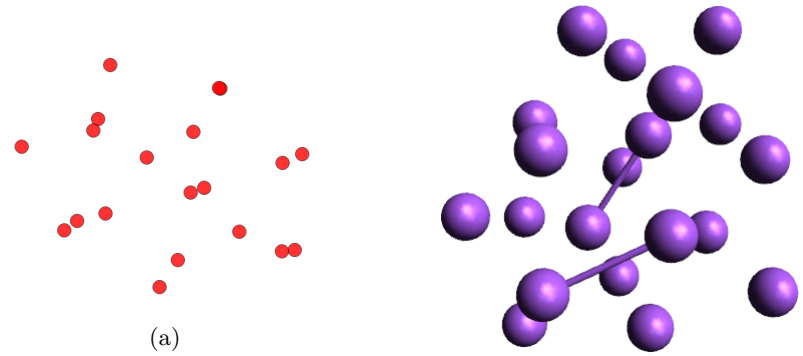

(a) (b)

Figure 3.3.1: Geometry of the Na_{20} cluster (a) in the plane $z = 0$, (b) in 3 dimensions.

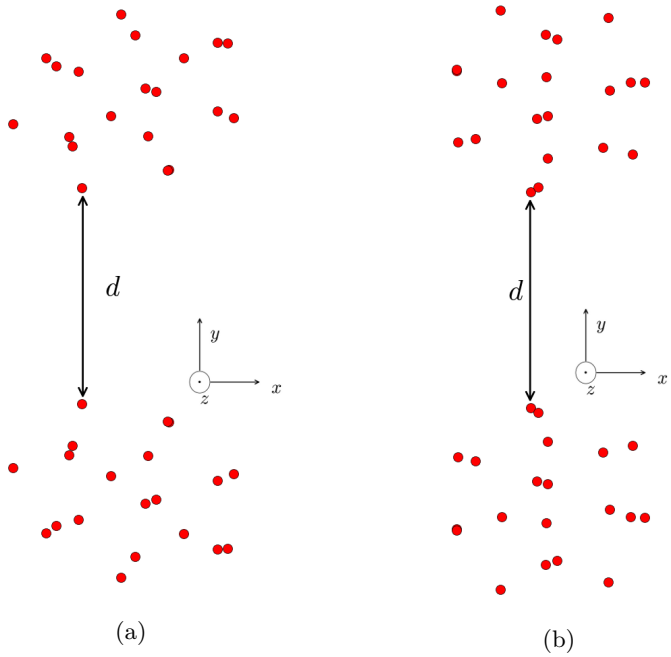

(a) (b)

Figure 3.3.2: Geometry of the Na_{20} cavity in the plane $z = 0$, (a) Without rotation (first geometry) and (b) with a rotation of 135° of each cluster (second geometry). The distance d between the two clusters is taken from the edge atoms.

3.3.1 Polarizability

For Na_{20} the average polarizazbility does not shift significantly in energy when the cavity size changes (Figure 3.3.6a). The main peak is at 2.8 eV, with a second peak at 3.05 eV. For large distances, the two geometries show similar polarizability (see Figure 3.3.6), but for small distances the first geometry (red curves) has one dominant peak with a higher polarizability, while the second geometry (dotted blue line) has two peaks (Figure 3.3.6). The P_{xx} and P_{zz} show a weak dependence on the distance (Figure 3.3.6b). Moreover, the intensity of the polarizability peaks of the first geometry is weaker than that of the one of the second geometry. For distances larger than 5.0 Å, P_{yy} is almost constant for distances larger than 7 Å (Figure 3.3.6c). However, the peak position is different for the first geometry ($\sim$ 3.05 eV) and for the second geometry ($\sim$ 2.8 eV).

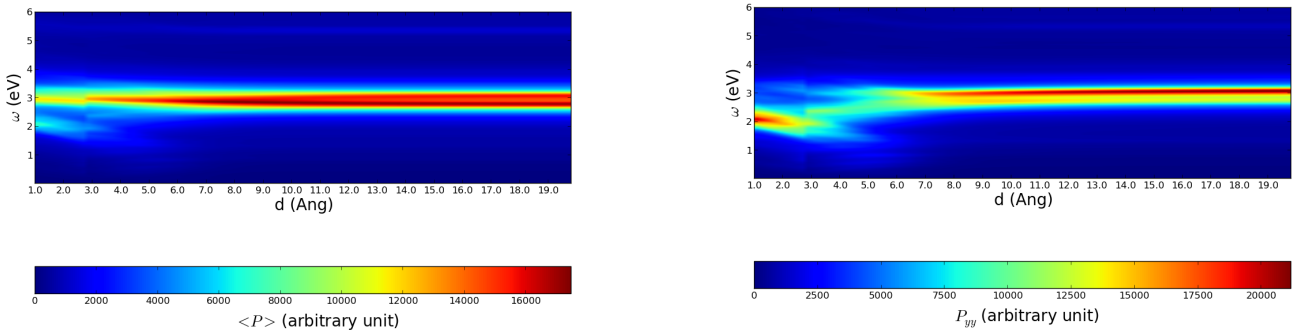

(a) (b)

Figure 3.3.3: Contour plots of the imaginary part of the average polarizability (a) and P_{yy} of the 2 Na_{20} clusters vs the distance d between the Na_{20} clusters for the first geometry.

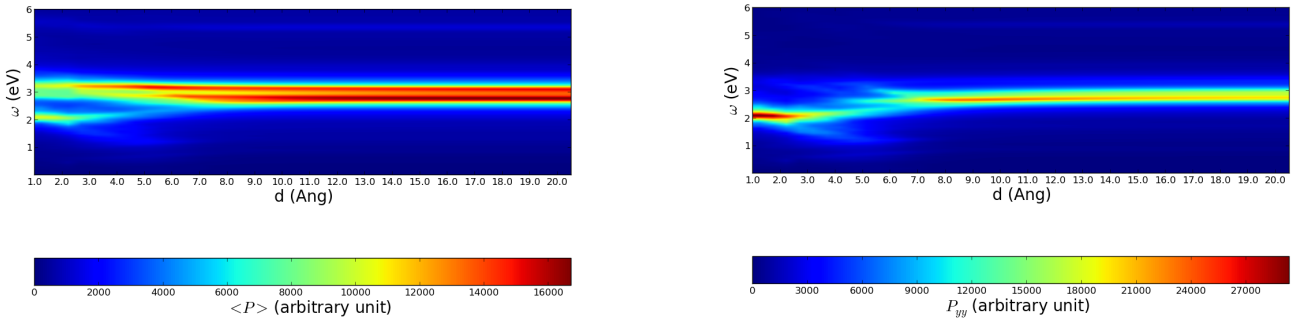

(a) (b)

Figure 3.3.4: Contour plots of the imaginary part of the average polarizability (a) and P_{yy} of the 2 Na_{20} clusters vs the distance d between the Na_{20} clusters for the second geometry.

As for the Na_8 dimer, the polarizability of the cavity converges to twice the one of a single cluster when the size of the cavity increases (Figure 3.3.5 shows this convergence but a small difference between the two polarizabilities is still visible for a cavity size of 20.0 Å). Comparing to the Na_8 polarizability shown in Figure 3.2.5a, the polarizability peaks of the Na_{20} are less shifted. The P_{xx} peak of the rotated geometry moves from 3.05 eV at large distances to 3.20 eV for small cavity sizes (Figure 3.3.6b). For the P_{zz} matrix element, the peaks have an energy of 2.9 eV (Figure 3.3.6d) and are almost no shifted. The P_{yy} matrix element shows a larger shift (Figures 3.3.3b and 3.3.6b). For large cavity sizes, the peaks have an energy of 2.75 eV and shift to 2.10 eV for small distances. During this shift, one can notice a range of distances (from 3.5 to 7.5 Å) where the polarizability is strongly attenuated.

The first geometry presents similar behavior to those of the second geometry. However, the shape of the P_{xx} and P_{zz} matrix elements are reversed (a consequence of the rotation of the clusters). The main peak of the P_{xx} matrix element (Figure 3.3.6b) almost does not shift and has an energy of 3.1 eV. The P_{zz} peak is slightly shifted from 2.80 eV at large distances to 2.95 eV for small cavity sizes (Figure 3.3.6d). As for the rotated geometry, it is the P_{yy} matrix element which induces the larger shift from 3.1 eV at large distances to 2.1 eV at small distances (Figures 3.3.3b and 3.3.6c). This large shifts for both geometries resemble those calculated for the Na_8 and the Na_2 clusters and are caused by the interaction between the dipoles generated in each cluster by the external field. The differences with the theoretical simple model presented in section 2.4 can be caused by the presence of other modes that are not take into account in this model.

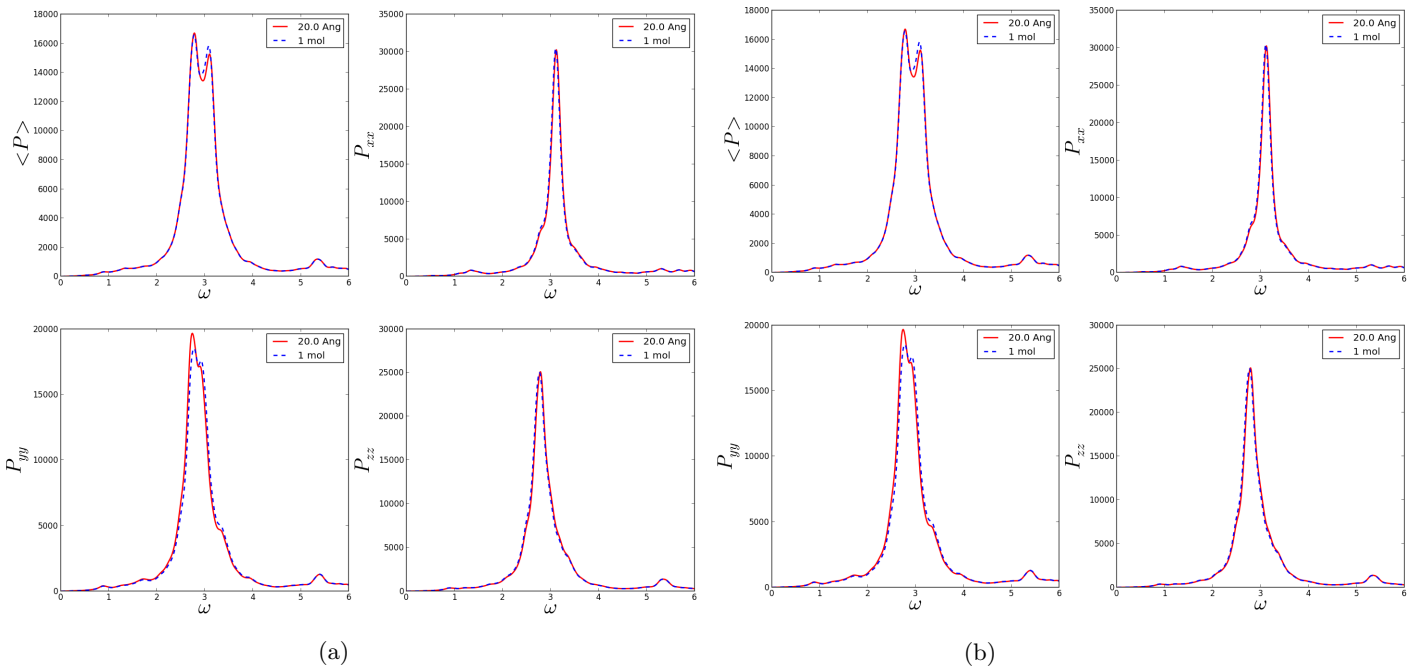

Figure 3.3.5: Comparison of the imaginary part of the polarizability of two clusters separated by a distance of 20.0 Å (red curves) with the polarizability for one molecule (dotted blue line) (a) for the non-rotated geometry and (b) for the rotated geometry.

3.3.2 Electric Field Enhancement

The effect of the rotation of the clusters on the induced electric field can be seen in Figure 3.3.7. The rotated geometry has its maximum intensity peak at 2.65 eV, while the non-rotated geometry has its maximum intensity peak at a higher energy (~ 3.05 eV) as shown in Figure 3.3.7c. The field enhancement is also stronger for the second geometry with a value of 172 while the field enhancement is only 150 for the first geometry. Figures 3.3.8 and 3.3.9 show the electric field enhancement distribution for different cavity sizes (5.0Å, 10.0Å, 15.0Å, 20.0Å,). By comparing the field distribution for the two geometries, the impact of the rotation on the field enhancement is apparent. Therefore, we can conclude that the intensity and distribution of the induced electric field enhancement is quite sensitive to small structural change, at least for these rather small clusters.

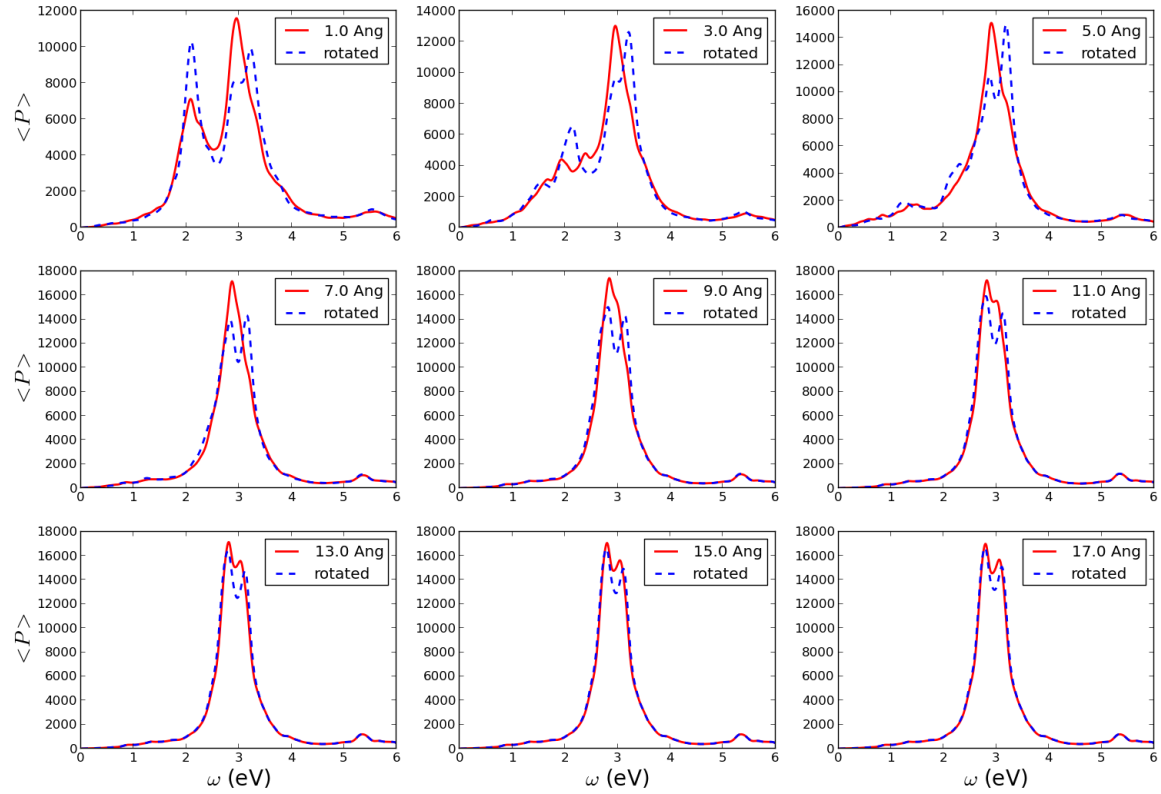

(a)

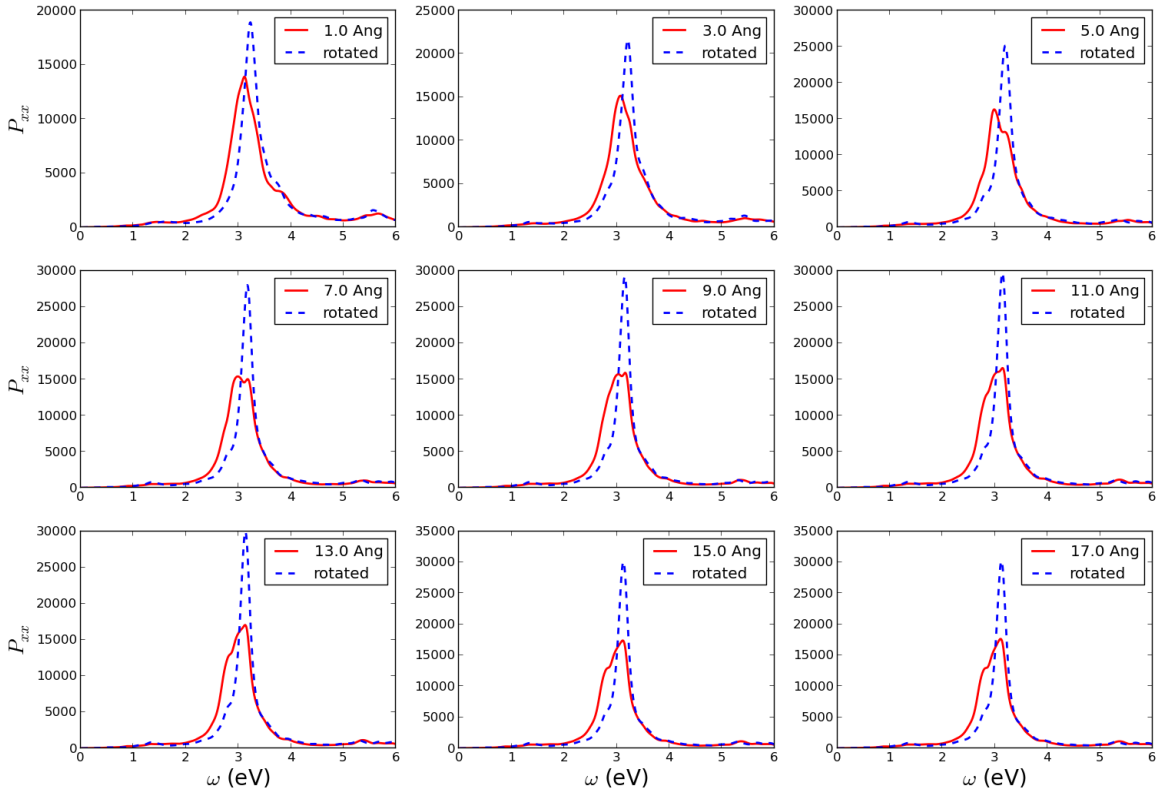

(b)

Figure 3.3.6

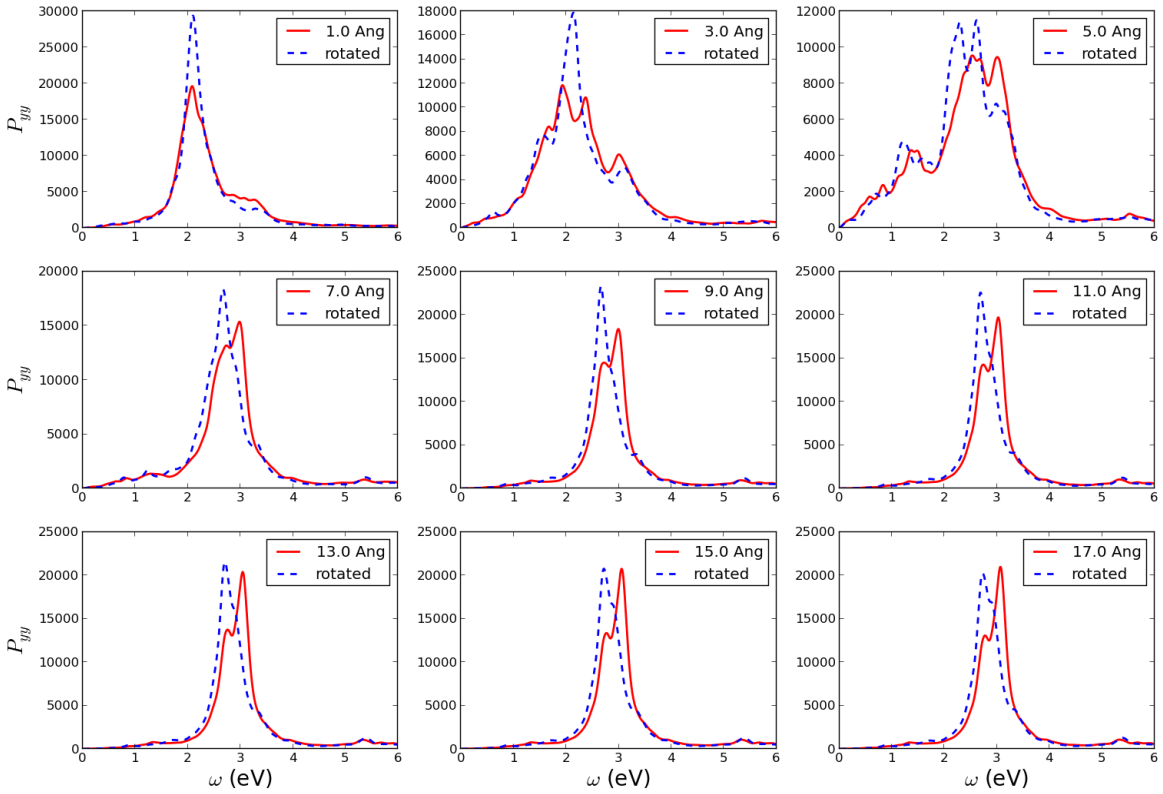

(c)

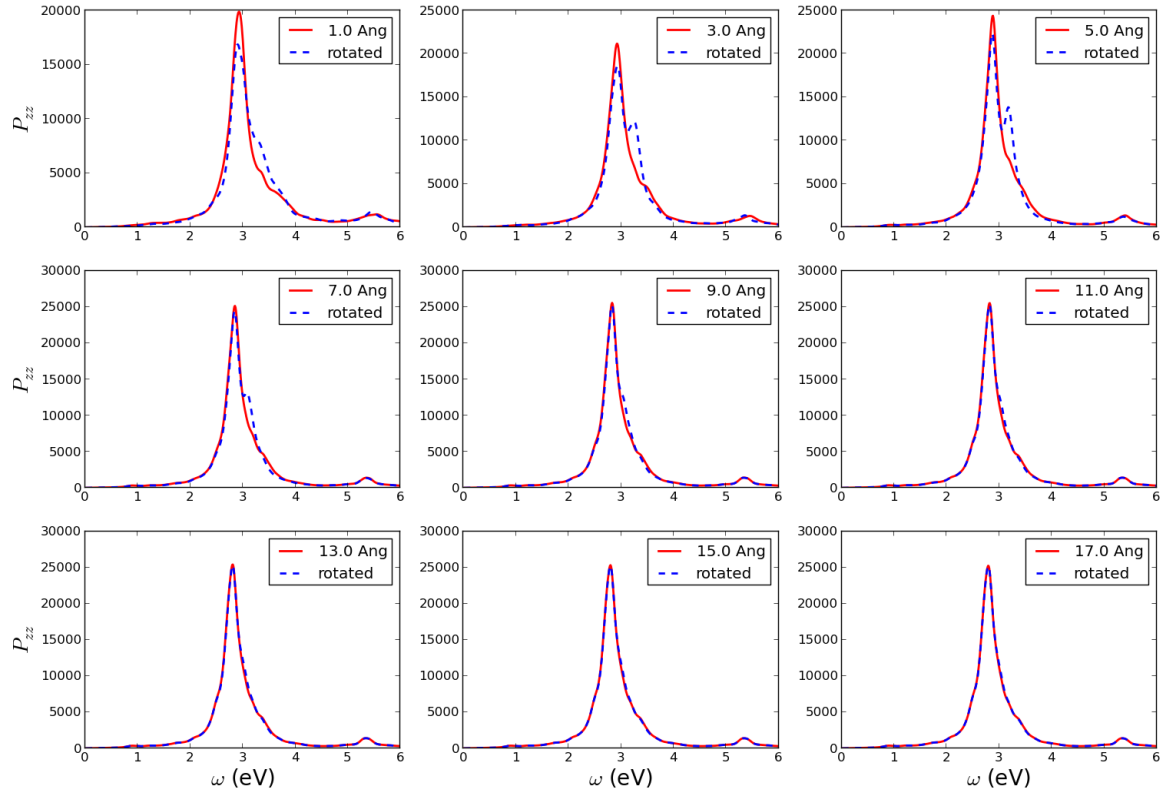

(d)

Figure 3.3.6: Imaginary part of the linear polarizability of two Na_{20} clusters vs energy for several distances between the clusters. The red curves correspond to the first geometry while the blue dotted lines are the polarizability after a rotation of 135° around the $z-$axis for each of the clusters. (a) Average polarizability, (b) P_{xx} matrix element, (c) P_{yy} matrix element, (d) P_{zz} matrix element.

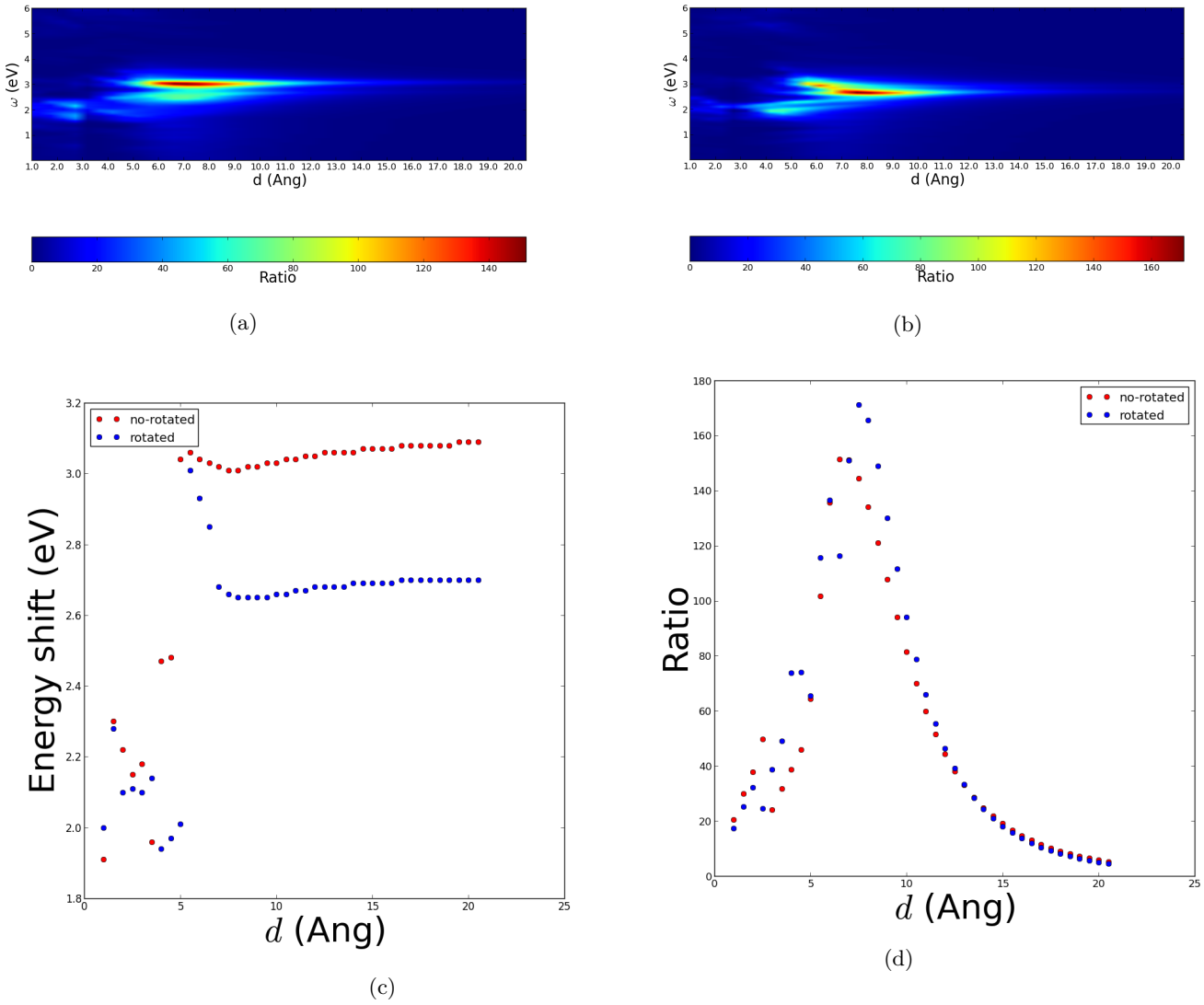

Figure 3.3.7: (a) and (b) contour plots of the electrical field intensity of the two Na_{20} clusters vs the distance *d* between the clusters for the first and second geometry respectively. (c) Evolution of the energy of the maximal intensity peak, and (d) evolution of the maximal intensity (the energy for a given distance is shown in Figure 3.3.7c), when the size of the cavity formed by the two Na_{20} clusters increases. The red dots correspond to the first geometry while the second geometry is represented by the blue dots.

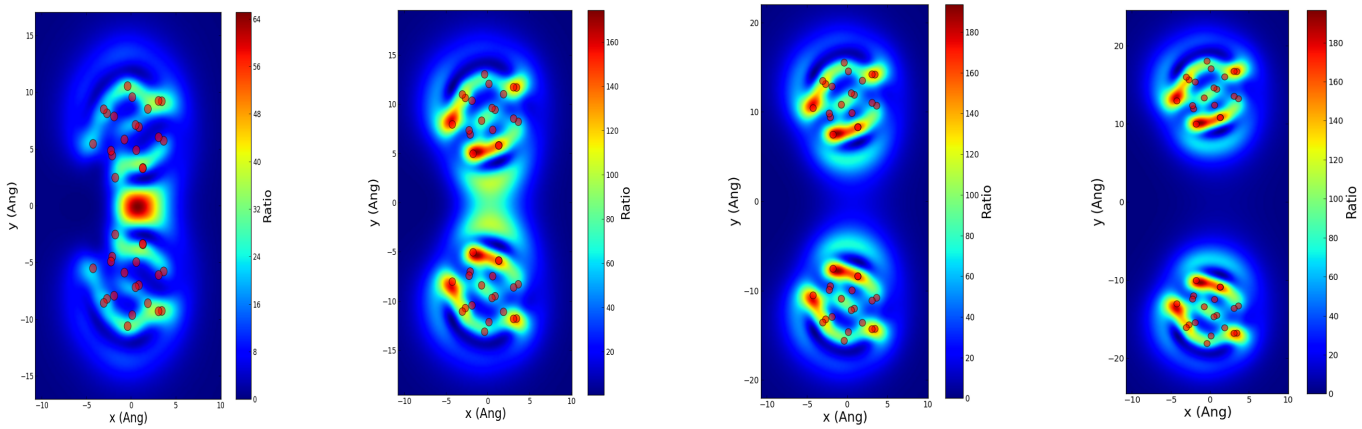

Figure 3.3.8: Intensity of the induced electric field for different cavity sizes of the first geometry at the energy of the maximal intensity peak, (a) cavity of 5.0Å at 3.04 eV, (b) cavity of 10.0Å at 2.66 eV, (c) cavity of 15.0Å at 3.0 eV, and (d) cavity of 20.0Å at 3.1 eV.

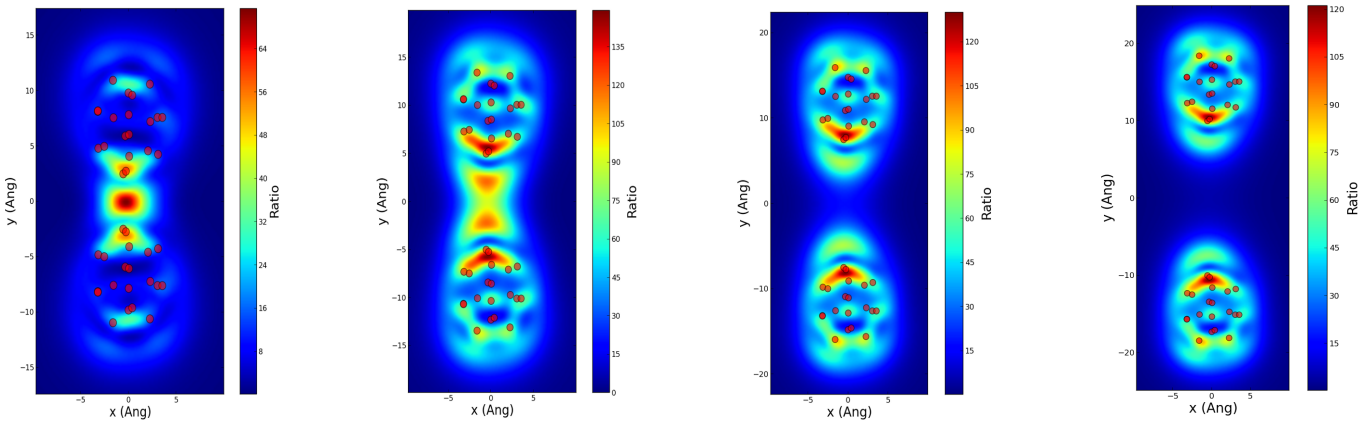

(a) (b) (c) (d)

Figure 3.3.9: Intensity of the induced electric field for different cavity sizes of the second geometry at the energy of the maximal intensity peak, (a) cavity of 5.0Å at 2.28 eV, (b) cavity of 10.0Å at 2.66 eV, (c) cavity of 15.0Å at 2.69 eV, and (d) cavity of 20.0Å at 2.7 eV.

The electric field enhancement for the Na_{20} clusters shows a similar behavior than that of the Na_8 dimer. By comparing Figure 3.3.7d and Figure 3.2.11c, one can notice that the enhancement in the case of Na_{20} is slightly larger ($\sim$ 150 and 172) than that of Na_8 ($\sim$ 122).The energy shift shown in Figure 3.3.7c moves the main peak of the intensity from $\sim$ 2.2 eV for small cavity sizes to $\sim$ 3.2 eV for larger cavity sizes with a big gap (2.3 $\longrightarrow$ 3.15) between 4 and 5 Å. This gap is caused by the presence of a second peak at 4 Å at the energy $\sim$ 3.15 eV. The shift, therefore, is rather abrupt and discontinuous. The intensity of this second peak is increasing until $\sim$ 7.0 Å and shifts slightly to higher energy (Figure 3.3.7a). The first peak, present for small cavity sizes, shifts to higher energy (from 2.2 $\longrightarrow$ 2.8 eV) and its intensity increases until 7 Å. However, it is less much weaker than the second peak.
The maximum intensity for the first geometry is around a cavity size of 7 Å, while for the second geometry, it is for a cavity size around 8 Å as shown in Figure 3.3.7d. For Na_8 clusters the maximum intensity occurs for a distance of 9 Å between the clusters (fig. 3.2.11c). Nevertheless, as in the case of the Na_8 cluster, for distances larger than 9 Å the intensity decays with a $\frac{1}{d^3}$ behavior showing the presence of the dipole-dipole interactions.

3.4 Na_{150} Cluster

Finally we have performed calculations for Na_{150} cluster. The particularity of this cluster is its larger size compared to the previous calculations which makes expect larger field enhancement. The geometry of this cluster was taken from Ref.[38].

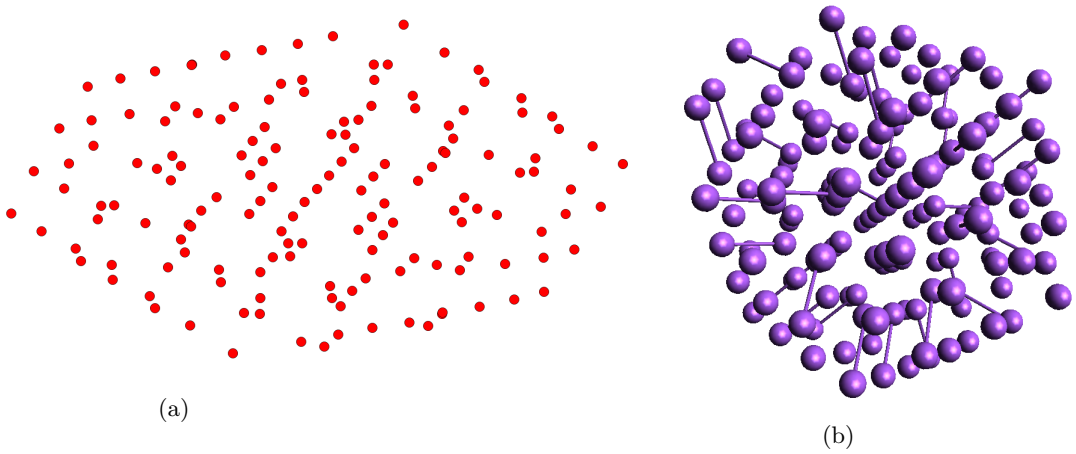

(a) (b)

Figure 3.4.1: Geometry of the Na_{150} cluster (a) in the plane $z = 0$, (b) in 3 dimensions.

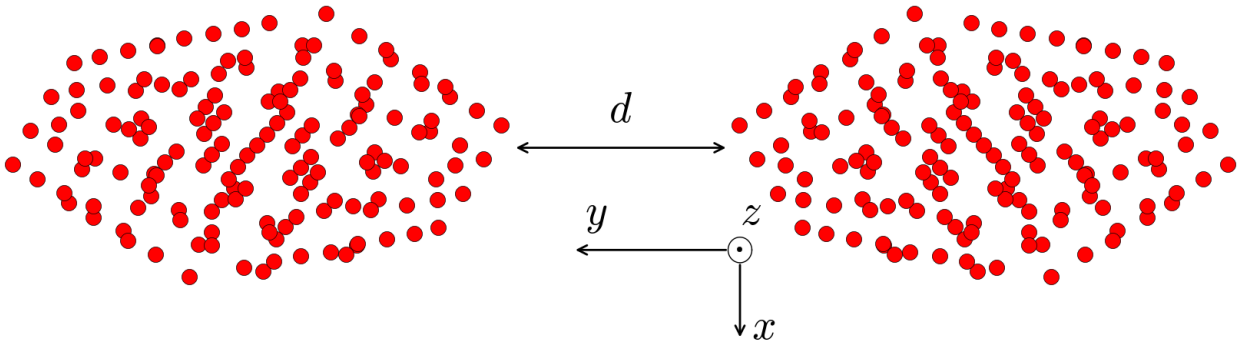

Figure 3.4.2: Geometry of the Na_{150} cavity in the plane $z = 0$, The distance d between the two clusters is taken from the edge atoms.

3.4.1 Polarizability

The analysis of the polarizability of the Na_{150} cavity only shows a small red shift compared to that of the smaller clusters. The average of the imaginary part of the polarizability shown in the contour plot 3.4.3a and Figure 3.4.5a, is characterized by this small energy shift from 3.55 eV for small cavity sizes to 3.3 eV for larger cavity sizes. As for smaller clusters, P_{xx} and P_{zz} matrix elements are almost not shifted, and the resonance occurs at 3.5 eV (Figure 3.4.5b). The P_{yy} matrix element shows a much stronger variation. On the contour plot 3.4.3b and Figure 3.4.5c, one can see that for very small distances between the two clusters, P_{yy} shows two peaks, one at the energy 1.85 eV and the other one at 3.35 eV. The peak at small energy could be caused by the electrostatic interaction between the clusters; but one has to notice the fast extinction of this peak when the distance increases (between 2 Å and 3 Å). Then when the cavity size

is larger than 5 Å, one can observe only one peak that is slightly shifted (from 3.11 eV at 5 Å to 3.3 eV at 15 Å). The shape of the P_{zz} matrix element is almost not changing with the cavity size (Figure 3.4.5d). Nevertheless, a small shift of the peak from 3.6 eV at 1 Å to 3.5 eV at 15 Å can be seen. This shifts has been observed in the small model presented in section 2.4, but for the Na_{150} the shifts amplitude is smaller than for the dipole model and for the Na_8 and Na_{20} clusters. Low amplitude shifts can be explained by the fact that other modes than the dipole-dipole interaction mode are present for large clusters. The fast disappearance of the low energy peak with the cavity size increases also point to the importance of electron tunneling and chemical interactions for those very small distances (notice that typical Na-Na bond distances are of the order of 3 Å).

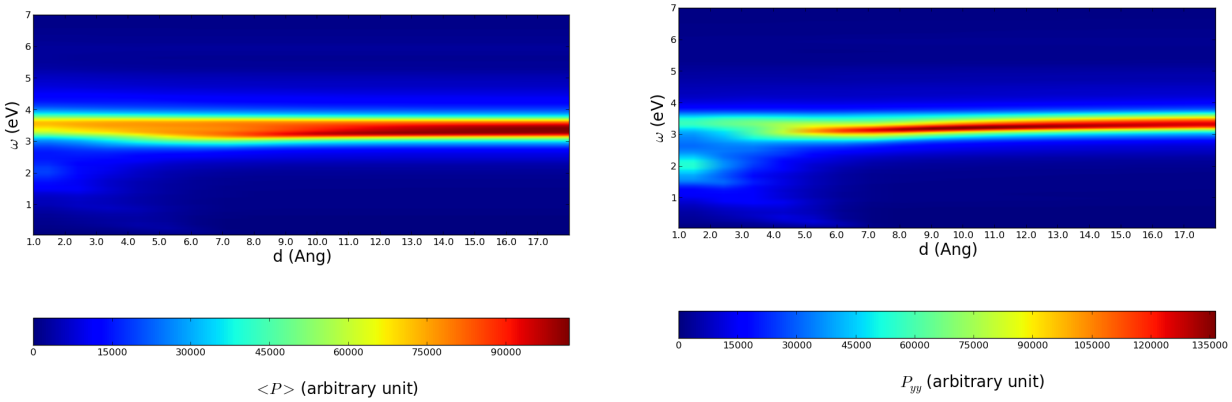

(a) (b)

Figure 3.4.3: Contour plots of the average polarizability (a) and P_{yy} of the two Na_{150} clusters vs the distance d between the clusters.

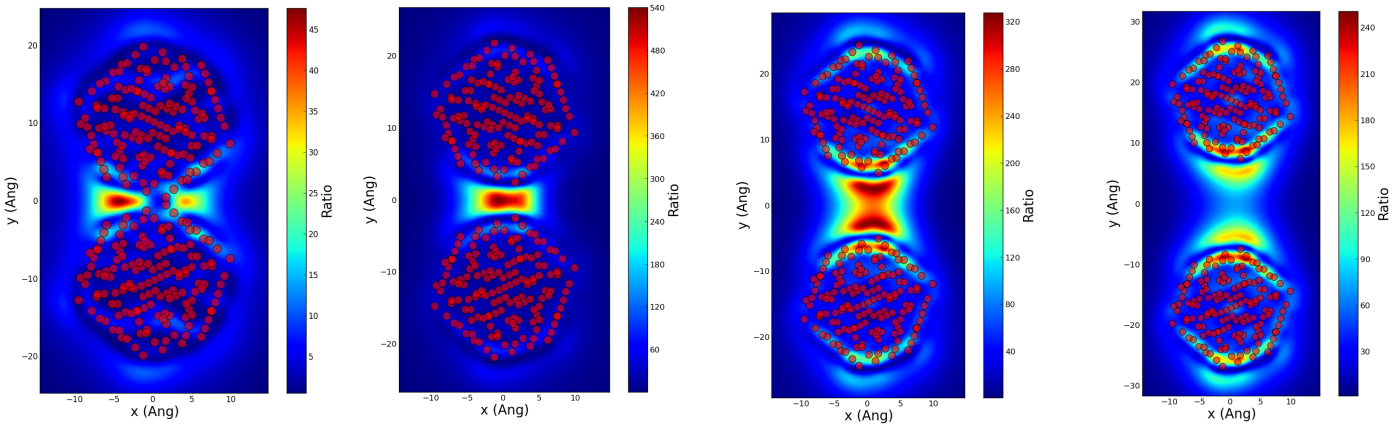

(a) (b) (c) (d)

Figure 3.4.4: Electric field enhancement for different cavity sizes at the energy of the maximum polarizability peak, in the plane $z = 0$ (a) cavity of 1.0Å at 1.85 eV, (b) cavity of 5.0Å at 3.08 eV, (c) cavity of 10.0Å at 3.185 eV and (d) cavity of 15.0Å at 3.22 eV.

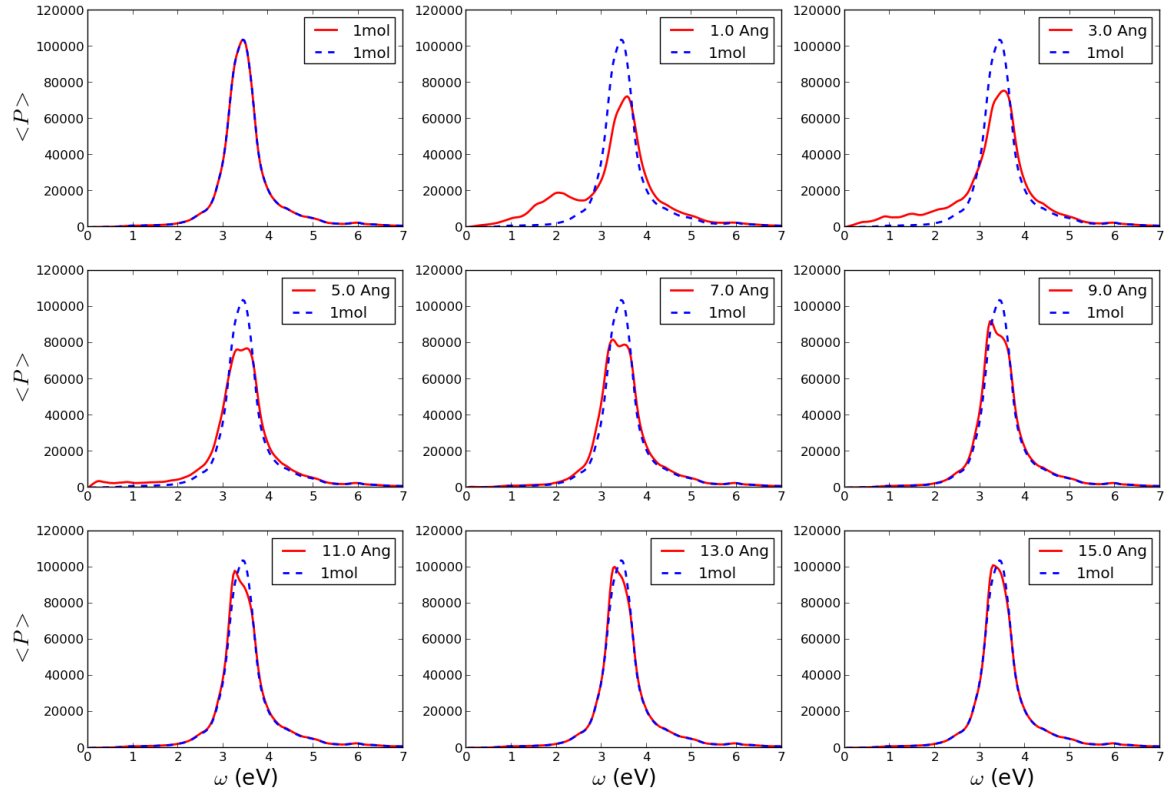

(a)

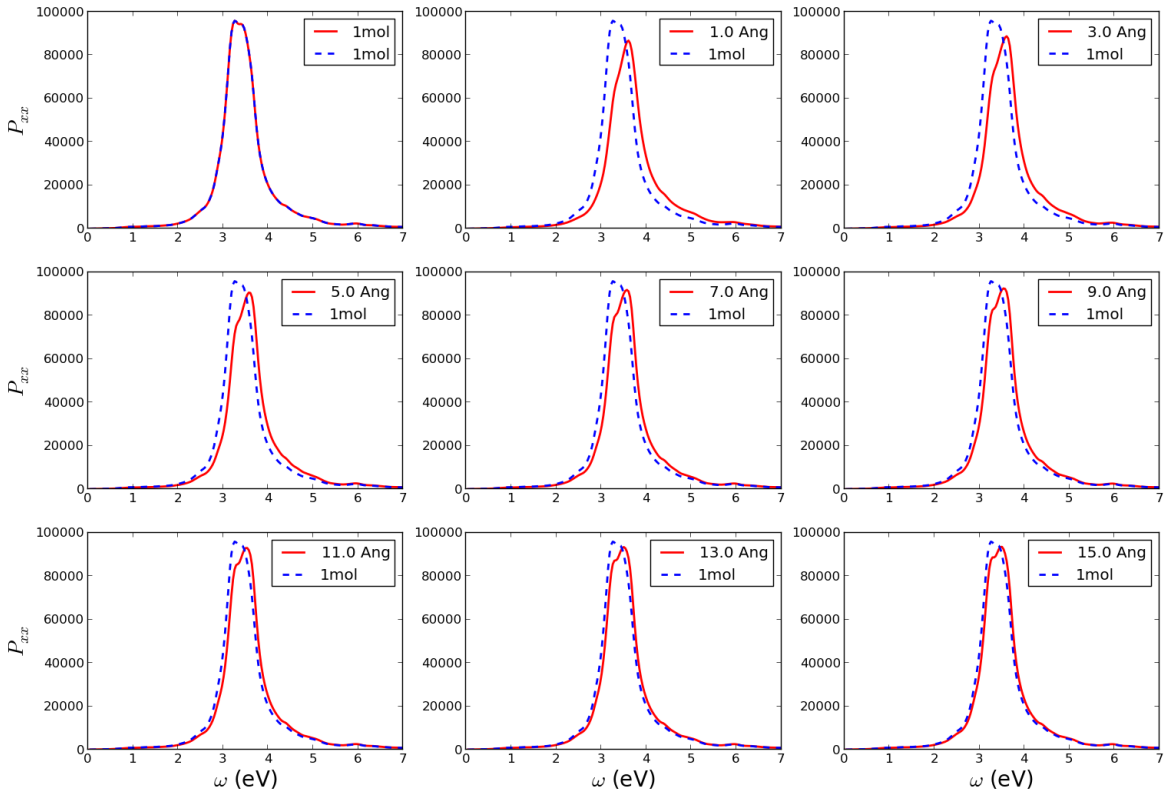

(b)

Figure 3.4.5

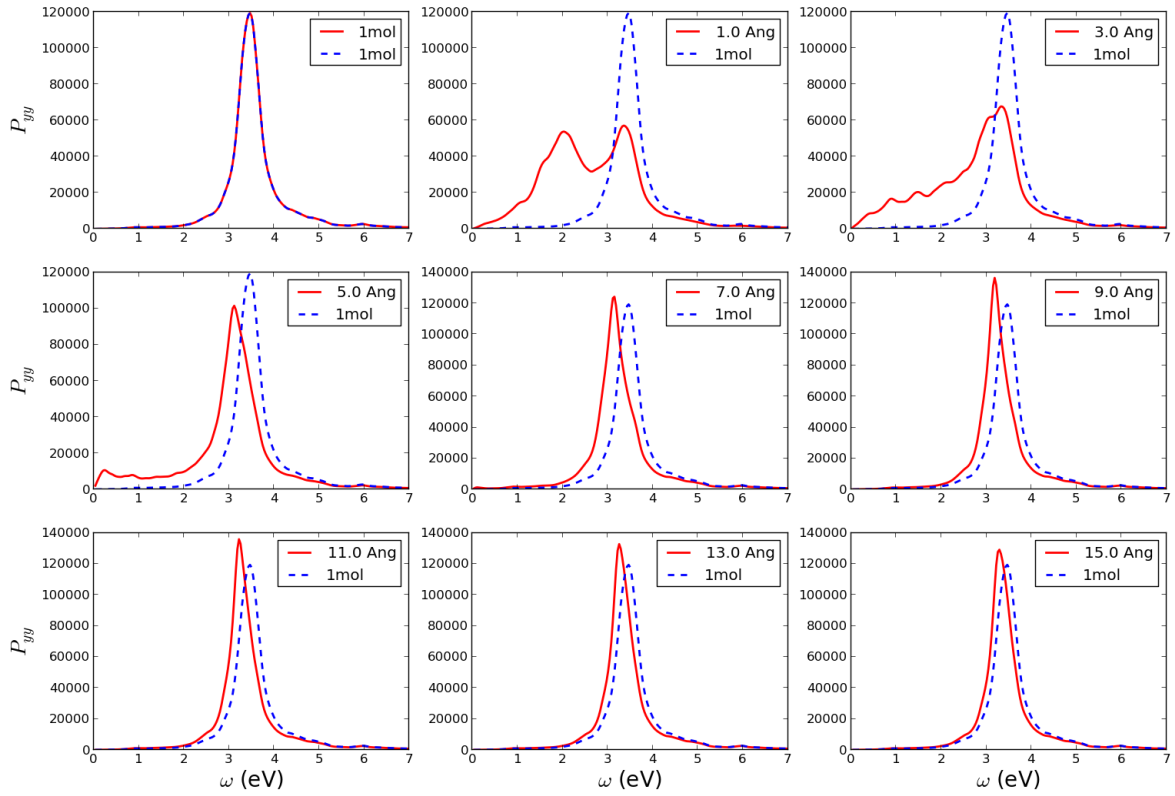

(c)

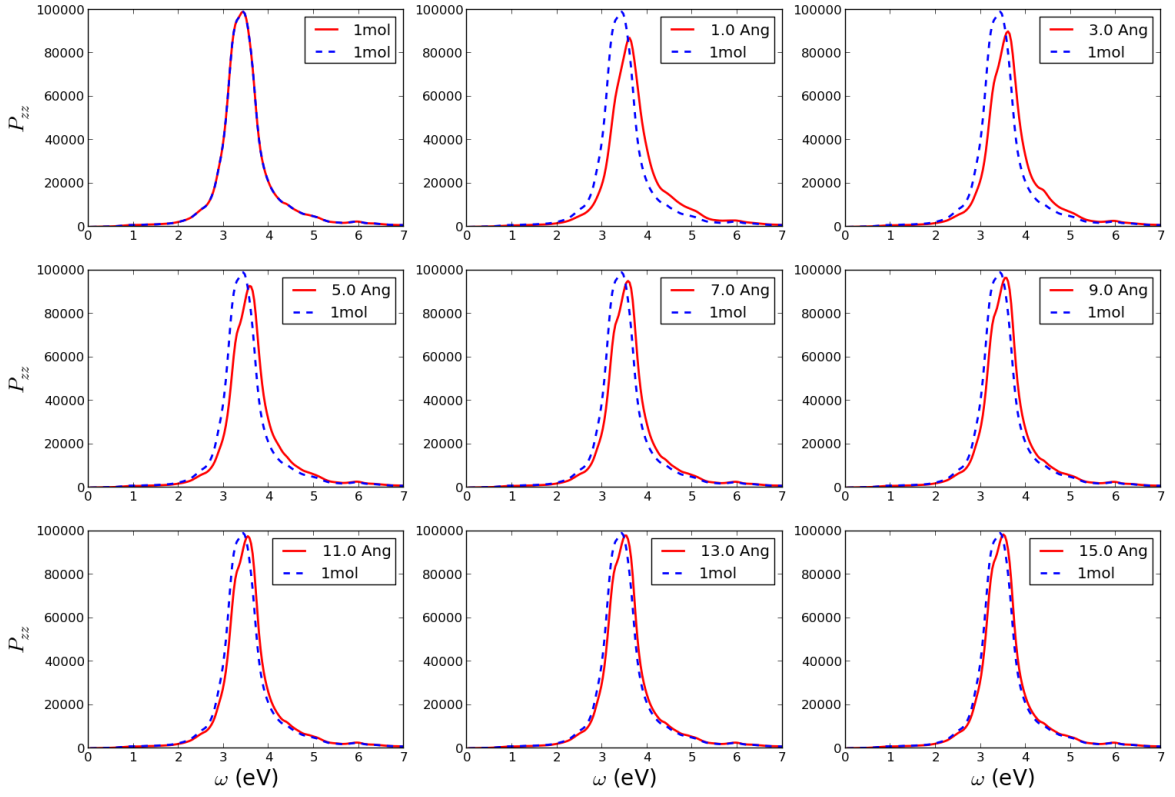

(d)

Figure 3.4.5: Imaginary part of the linear polarizability of two Na_{150} clusters vs energy for several distances between the clusters. The blue dotted lines represents the polarizability of one cluster multiply by two. (a) Average polarizability, (b) P_{xx} matrix element, (c) P_{yy} matrix element, (d) P_{zz} matrix element.

3.4.2 Electric field Enhancement

Compared to smaller clusters, the electric field enhancement of the Na_{150} dimer is quite larger, as shown in Figure 3.4.6c (compare to Figure 3.2.11c for Na_8, and Figure 3.3.7d for Na_{20}). The contour plot 3.4.6a and Figure 3.4.6c show that there is a large field enhancement for a cavity size from 4.0 Å to 9.0 Å with a maximal enhancement of 590 around 6.0 Å. This distance is slightly smaller that for Na_8 (around 8 Å) and for Na_{20} (around 9 Å). Another interesting result is the large energy shift shown in Figure 3.4.6b. For a cavity size of 1 Å the maximal intensity peak appear at an energy of 1.85 eV, while for large cavity size, the peak converge to the one molecule value which is 3.3 eV, therefore, an energy difference of 2.45eV. While for the Na_8 and Na_{20}, the shift are 0.7 eV and 1eV respectively (Figures 3.2.11b and 3.3.7c). This shift follows the same shape than the one of the P_{yy} matrix element. Thus, as for smaller clusters, induced electric field and P_{yy} are strongly connected. Figure 3.4.4 shows the electric field distribution for several cavity sizes at their maximal intensity peak given in Figure 3.4.6b. One can notice that contrary to the smaller clusters, the electric field enhancement is mainly situated in the center of the cavity and not distributed inside the clusters. This is a consequence of the fact that the field enhancement is still strong for large distances (the ratio of induced field intensity and the external field intensity is 38 for a cavity of 18 Å, while for the same cavity, the ratio for Na_8 is 5 and 10 for Na_{20}).

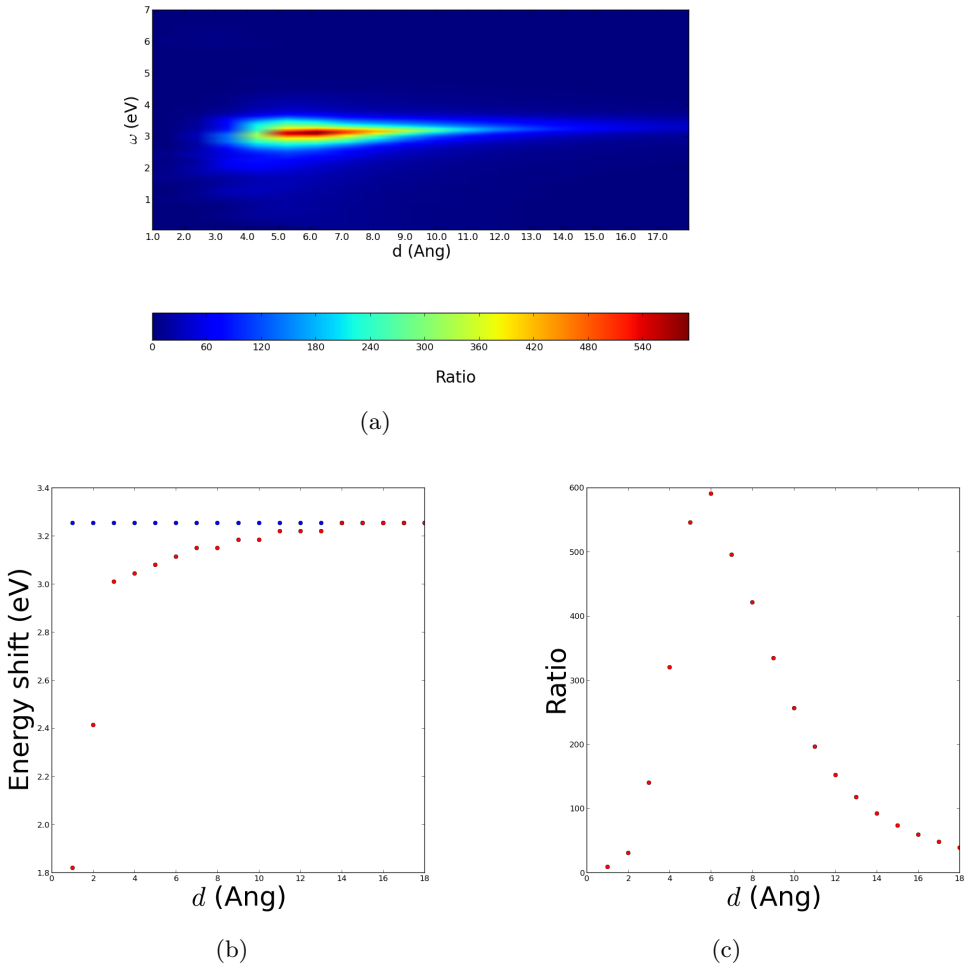

Figure 3.4.6: (a) Contour plot of the electric field enhancement of two Na_{150} clusters vs the cavity size, (b) evolution of the energy of the maximal intensity peak, and (c) evolution of the maximal intensity (the energy for a given distance is given in figure 3.4.6b) when the size of the cavity formed by the two Na_{150} clusters increases. The blue dots are the data for the one cluster calculations, while the red dots are calculations for the two clusters.

Chapter 4

Conclusion

In this thesis the absorption cross-section and the electric field enhancement were analyzed for four Na dimmers (Na_2, Na_8, Na_{20}, and Na_{150}) with a new implementation of TDDFT in the linear response regime. Thanks to the low computational cost of our new TDDFT implementation we were able to perform a detailed analysis of the density change and the induced electric field distribution. In this master thesis a summary of the theory used for the response calculation and the implementation of the electric field enhancement was presented. In this first part, we first explained the principles of the time-dependent perturbation theory that is used to derive an expression for the absorption cross-section. The basics of DFT and TDDFT were also presented and used to derive expressions for the frequency-dependent induced density change and the corresponding induced electric field. Finally, we analyzed a small model of two interacting dipoles in order to compare with our TDDFT results.

After this brief description of the theory, our *ab-initio* calculations obtained with this new implementation of TDDFT were presented. We analyzed the optical response of four sodium dimers. From these calculations we have been able to demonstrate that the atomic structure of the metal clusters plays a key role for determining accurately both the absorption cross-section and electric field enhancement. First, we have shown that the optical properties of the dimer of Na_2 molecules, with a density distribution similar to that of a dipole, are consistent with the results provided by the simple model. Moreover, the polarizability of the Na_8 is in good agreement with previous calculations. This two cross-checks give us confidence in our new TDDFT implementation. Then, the polarizability for the three dimers as function of the distance between the clusters for an energy range between 0 and 7 eV were studied. It was shown that at large distances only one polarizability peak is observable for the three dimers and that the polarizability converges to twice the value of the polarizability of one cluster, which is the expected result. At small distances, however, several peaks have been observed, which shows the presence of dipolar modes as well as other modes. Finally, our calculations of the electric field enhancement for the three dimers follow a similar shape than the polarizability with only one peak at large distance. Moreover, unlike the polarizability, we have seen that the field enhancement decreases rapidely at large distance with a maximum around 8 Å. Furthermore, the electric field enhancement shows a dependence with the orientation of the clusters respect to the external field. The size of the clusters play also an important role on the field enhancement. We showed that Na_{150} clusters exhibit a higher electric field enhancement in the cavity center than Na_8 and Na_{20}.

For a future investigation, it would be very interesting to first analyze the cross-section and electric field enhancement for other species, like large silver clusters, in order to find a system which provides the largest field enhancements. Furthermore, the analysis of the effect of a molecule placed in the center of the nanocavity on the field enhancement distribution can be relevant for the study of Surface Enhanced Raman Scattering. In particular, we will study the effect of an aromatic molecule in a cavity for different orientations of the molecule.

Another interesting idea would be to analyze the conductance and the impact in the optical response, between the two clusters when they are linked by a bridge of atoms. The variation of the conductance as function of the bridge thickness would provide valuable information.

Appendices

Appendix A

Response Function in a Basis of Dominant Products

The expression for the density change (2.98) involves the interacting response function $\chi(\mathbf{r}, \mathbf{r}', \omega)$. In order to find this function, one should solve a similar equation to the Dyson's equation[42] with the *Random phase approximation*

$$\chi(\mathbf{r}, \mathbf{r}', \omega) = \chi_0(\mathbf{r}, \mathbf{r}', \omega) + \int \chi_0(\mathbf{r}, \mathbf{r}', \omega) K_{\mathrm{Hxc}}(\mathbf{r}'', \mathbf{r}''') \chi(\mathbf{r}''', \mathbf{r}', \omega) d\mathbf{r}'' d\mathbf{r}''' \tag{A.1}$$

Where the non-interacting response function $\chi_0(\omega)$ and the interaction kernel K_{Hxc} are present. In our work, the Hartree-exchange-correlation kernel K_{Hxc} is independent on frequency because the simple adiabatic LDA is assumed for the exchange-correlation functional. The non-interacting response function $\chi_0(\mathbf{r}, \mathbf{r}', \omega)$ is expressed in terms of sums over eigen states $\psi_i(\mathbf{r})$ of the Kohn-Sham Hamiltonian[43]

$$\chi_0(\mathbf{r}, \mathbf{r}', \omega) = \sum_{i,j} (n_i - n_j) \frac{\psi_i^*(\mathbf{r}) \psi_j(\mathbf{r}) \psi_j^*(\mathbf{r}) \psi_i(\mathbf{r}')}{\omega - (E_j - E_i) + i\varepsilon} \tag{A.2}$$

Here ε is a broadening constant, i and j enumerate the Kohn-Sham eigen-states. E_i and n_i denote the eigen-energy and the occupation number of the Kohn-Sham eigen-state i. Both interacting and non-interacting response functions have been expanded in terms of a basis of dominant products[33]

$$\chi_0(\mathbf{r}, \mathbf{r}', \omega) = \sum_{\mu\nu} F^\mu(\mathbf{r}) \chi^0_{\mu\nu}(\omega) F^\nu(\mathbf{r}') \tag{A.3}$$

The basis functions $F^\mu(\mathbf{r})$ obey a radial-angular decomposition analogous to usual atom-centered orbitals. Dominant products span the space of products of the localized orbitals[33, 44] and maintain their locality

$$f^a(\mathbf{r}) f^b(\mathbf{r}) = \sum_\mu V_\mu^{ab} F^\mu(\mathbf{r}) \tag{A.4}$$

By inserting the expansion (A.3) into the equation (A.1)

$$\chi_{\mu\nu}(\omega) = \chi^0_{\mu\nu}(\omega) + \sum_{\mu'\nu'} \chi^0_{\mu\mu'}(\omega) K^{\mu'\nu'}_{\mathrm{Hxc}} \chi_{\nu'\nu}(\omega) \tag{A.5}$$

And one gets the following relations

$$\chi_0(\mathbf{r},\mathbf{r}',\omega) = \sum_{\mu\nu}\chi^0_{\mu\nu}(\omega)F^\mu(\mathbf{r})F^\nu(\mathbf{r}'), \tag{A.6}$$

$$\chi(\mathbf{r},\mathbf{r}',\omega) = \sum_{\mu\nu}\chi_{\mu\nu}(\omega)F^\mu(\mathbf{r})F^\nu(\mathbf{r}'), \tag{A.7}$$

$$\delta n(\mathbf{r},\omega) = \delta n_\mu(\omega)F^\mu(\mathbf{r}). \tag{A.8}$$

Appendix B

Pseudo-Potential

The pseudo-potential was calculated using the ATOM program[45], the file head is,

```
1  Na ca nrl nc
2  ATM3  13-MAR-14 Troullier-Martins
3  3s 1.00  r= 2.94/3p 0.00  r= 2.94/3d 0.00  r= 2.94/4f 0.00  r= 2.94/
4  4  0 1054  0.225341106970E-03  0.125000000000E-01   1.00000000000
5  Radial grid follows
```

The first line gives the atomic configuration

- Na is the specie label.
- ca stands for Ceperley-Alder functional[36].
- nrl stand for non-relativistic calculation.
- nc stand for no-core correction.

The shell radii are given in line 3 and resume in table B.1

Table B.1: Shell radii of the Na pseudo-potential

shell	radii (Å)
$3s$	2.94
$3p$	2.94
$3d$	2.94
$4f$	2.94

Appendix C

Convergence of the Electric Field

In this appendix, the convergence of the intensity of the induced electric field as function of the grid fineness is shown. The convergence test was performed with a N_2 dimer, the broadening constant was set to $\varepsilon = 0.033\,\text{eV}$ (default value). The electric field enhancement was calculated in the center of the molecule at the maximum intensity peak ($\omega = 15.87\,\text{eV}$), the distance between the atoms in one molecule is 1.098 Å and the distance between the molecule is 4.0 Å.

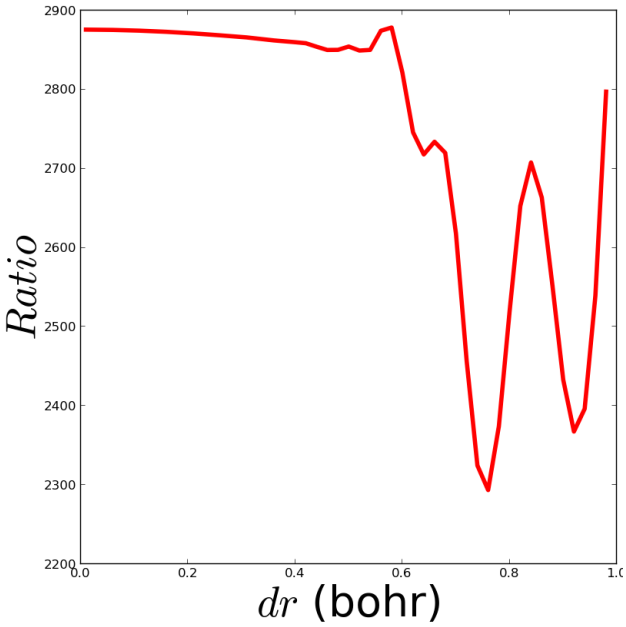

Figure C.0.1: Evolution of the induced electric field as function of the spatial precision dr. The spatial step is changing in the three directions at the same time and $dx = dy = dz = dr$. The test was done with a simple N_2 dimer.

From figure C.0.1, one can conclude that below a precision of 0.4 Bohr, the results are converging.

Bibliography

[1] G. Gugliotta. *The Washington Post*, page A14, May 2002.

[2] M. Gomez-Lopez S. J. Langford and J. F. Stoddart. *Acc. Chem. Res.*, 31(405), 1998.

[3] F. M. Raymo V. Balzani, A. Credi and J. F. Stoddart. *Angew. Chem. Int. Ed.*, 39(3348), 2000.

[4] F. M. Raymo S. J. Langford and J. F. Stoddart. *Molecular Electronics*. Blackwell, London, 1998.

[5] S. Kapoor, S. Adhikari, C. Gopinathan, and J.P. Mittal. Radiolytic production of metallic nanoclusters in a quaternary microemulsion system. *Materials Research Bulletin*, 34(8):1333 – 1343, 1999.

[6] Harald Kneipp Katrin Kneipp, Martin Moskovits. *Surface-Enhanced Raman Scattering*, volume 103. Springer, 2006.

[7] D. Foerster F. Marchesin, P. Koval and D. Sanchez-Portal. Optical properties of carbon nanoflakes Optical properties of carbon nanoflakes. *(submitted)*.

[8] Pu Zhang, Johannes Feist, and Angel Rubio. Ab-initio nanoplasmonics: atoms matter. (arXiv:1403.8016v1), 2014.

[9] Ruben Esteban, Andrei G Borisov, Peter Nordlander, and Javier Aizpurua. Bridging quantum and classical plasmonics with a quantum-corrected model. *Nature communications*, 3(May):825, January 2012.

[10] Jorge Zuloaga, Emil Prodan, and Peter Nordlander. Quantum description of the plasmon resonances of a nanoparticle dimer. *Nano Letters*, 9(2):887–891, 2009.

[11] Tatiana V. Teperik, Peter Nordlander, Javier Aizpurua, and Andrei G. Borisov. Quantum effects and nonlocality in strongly coupled plasmonic nanowire dimers. *Optics Express*, 21(22):27306, November 2013.

[12] Erich Runge and E. K. U. Gross. Density-functional theory for time-dependent systems. *Phys. Rev. Lett.*, 52:997–1000, Mar 1984.

[13] F. M. S. Nogueira M. A. L. Marques, N. T. Maitra. *Fundamental of Time-Dependent Density Functionnal Theory*. Springer, Berlin, 2012.

[14] W. Kohn. Nobel Lecture: Electronic structure of matter-wave functions and density functionals. *Reviews of Modern Physics*, 71(5):1253–1266, October 1999.

[15] David J. Griffiths. *Introduction to Quantum Mechanics*. Prentice Hall, 1994.

[16] Mark Fox. *Optical Properties of Solids*. Oxford University Press, 2010.

[17] Robert C Hilborn. Einstein coefficients, cross sections,. pages 1–12, 2002.

[18] R. M. Martin. *Electronic Structure: Basic Theory and Practical Methods*. Cambridge University Press, Cambridge„ 2004.

[19] G. Malloci, G. Cappellini, G. Mulas, and A. Mattoni. Electronic and optical properties of families of polycyclic aromatic hydrocarbons: A systematic (time-dependent) density functional theory study. *Chemical Physics*, 384(1-3):19–27, 2011.

[20] N.H. March. *Theory of the Inhomogeneous Electron Gas*. Springer US, 1983.

[21] Robert G. Parr and Weitao Yang. *Density-Functionnal Theory of Atoms and Molecules*. Oxford University Press, 1989.

[22] P. Hohenberg and W. Kohn. Inhomogeneous electron gas. *Phys. Rev.*, 136:B864–B871, Nov 1964.

[23] Mel Levy. Electron densities in search of hamiltonians. *Phys. Rev. A*, 26:1200–1208, Sep 1982.

[24] Ulf von Barth. Local-density theory of multiplet structure. *Phys. Rev. A*, 20:1693–1703, Oct 1979.

[25] John P. Perdew, Kieron Burke, and Matthias Ernzerhof. Generalized gradient approximation made simple. *Phys. Rev. Lett.*, 77:3865–3868, Oct 1996.

[26] Stephan Kümmel and John P. Perdew. Optimized effective potential made simple: Orbital functionals, orbital shifts, and the exact kohn-sham exchange potential. *Phys. Rev. B*, 68:035103, Jul 2003.

[27] Ireneusz Grabowski, So Hirata, Stanislav Ivanov, and Rodney J. Bartlett. Ab initio density functional theory: Oep-mbpt(2). a new orbital-dependent correlation functional. *The Journal of Chemical Physics*, 116(11):4415, 2002.

[28] E. Runge and E. K. U. Gross. *Phys. Rev. Lett.*, 52:997, 1984.

[29] R. van Leeuwen. *Phys. Rev. Lett*, 82:3863, 1999.

[30] M Petersilka, Uj Gossmann, and Ek Gross. Excitation energies from time-dependent density-functional theory. *Physical Review Letters*, 76(8):1212–1215, February 1996.

[31] Walter Harrison. *Solid State Theory*. McGraw-Hill, 1972.

[32] Peter Koval, Dietrich Foerster, and Olivier Coulaud. A Parallel Iterative Method for Computing Molecular Absorption Spectra. *Journal of Chemical Theory and Computation*, 6(9):2654–2668, September 2010.

[33] D Foerster, P Koval, and D Sánchez-Portal. An O(N3) implementation of Hedin's GW approximation for molecules. *The Journal of chemical physics*, 135(7):074105, August 2011.

[34] J.M Soler et al. *J. Phys:Condens. matter*, 2745(4), 2002.

[35] N Troullier and J. L. Martins. Efficient pseudopotentials for plane-wave calculations. *Physical Review B*, 43(3), 1993.

[36] D. M. Ceperley and B.J. Alder. *Physical Review Letters*, 566(46), 1980.

[37] Jl Martins, J Buttet, and R Car. *Physical review. B, Condensed matter*, 31(4):1804–1816, February 1985.

[38] D. J. Wales. The cambridge cluster database. http://www-wales.ch.cam.ac.uk/CCD.html.

[39] Argyrios Tsolakidis, Daniel Sánchez-Portal, and Richard Martin. Calculation of the optical response of atomic clusters using time-dependent density functional theory and local orbitals. *Physical Review B*, 66(23):235416, December 2002.

[40] Jian-Hao Li, Michitoshi Hayashi, and Guang-Yu Guo. Plasmonic excitations in quantum-sized sodium nanoparticles studied by time-dependent density functional calculations. *Physical Review B*, 88(15):155437, October 2013.

[41] C. Yannouleas and E. Vigezzi. Evolution of the optical properties of alkali-metal microclusters towards the bulk: The matrix random-phase approximation description. *Physical Review B*, 47(15), 1993.

[42] M. Petersilka, U. J. Gossmann, and E. K. U. Gross. Excitation energies from time-dependent density-functional theory. *Phys. Rev. Lett.*, 76:1212–1215, Feb 1996.

[43] E. K. U. Gross and K. Burke. *Time-Dependent Density Functionnal Theory*. Springer, Berlin, 2008.

[44] D. Foerster. Elimination, in electronic structure calculations, of redundant orbital products. *The Journal of Chemical Physics*, 128(3), 2008.

[45] Sverre Froyen, L Cohen, and S Louie. Nonlinear ionic pseudopotentials in spin-density-functional calculations. *Physical Review B*, 26(4), 1982.